LONDON'S GLOBAL UNIVERSITY

DEVELOPMENTS OF IRON OXIDE NANOPARTICLES FOR MAGNETIC THERMOTHERAPY AND MULTIMODAL IMAGING

GAVIN S. BELL

University College London

Department of Chemistry

A thesis submitted for the partial fulfilment for the degree of Doctor of Philosophy

2018

DECLARATION

I, Gavin Bell, declare that the work presented in this thesis is of my own original work and that all material from other sources has been clearly identified and acknowledged.

Gavin S. Bell

March, 2018

ABSTRACT

Current methods of cancer therapy and detection still warrant high demand and great developments. Utilising the fundamental magnetism of iron oxide nanoparticles, it is possible to harness that magnetic power for the development of new, influential therapeutic and imaging modalities. In this thesis, a detailed look into the use of iron oxide nanoparticles as a material for magnetic thermotherapy and bio-imaging will be undertaken.

Iron oxide nanoparticles are synthesised using a common co-precipitation synthesis. Stabilisation was achieved with citrate molecules followed by advanced functionalisation of the nanomaterial with gold achieved *via* reduction of Au^{3+} ($HAuCl_4$) to Au^0 from the citrate ligands. These materials were shown to exhibit remarkable intrinsic heating power when under the influence of an external alternating current magnetic field.

Following the potential of iron oxide nanoparticles functionalised with gold for magnetic hyperthermia, multimodal imaging and therapeutic probes were studied. Iron oxide gold nano were analysed as possible Raman enhancer substrates.

Finally, iron oxide nanoparticles were synthesised using an organic photoacoustic dye as a stabilising ligand to functionalise the magnetic Fe_3O_4 cores with optical properties. This lead to the novel co-precipitation synthesis of indocyanine green (ICG) and Flamma®774 covalently attached to Fe_3O_4 nanoparticles.

ACKNOWLEDGEMENTS

There are many people I need to thank for their unwavering support, contributions and time over the course of this thesis. Foremost, is that of my supervisors; Professor Ivan P. Parkin, Professor Quentin A. Pankhurst and Professor Malini Olivo, for their comments, suggestions and wholehearted support of my projects and ideas. Without their guidance I would not have achieved this milestone.

I owe a huge thank you to Dr Paul Southern and Dr Lara Bogart for sharing their incredible expertise on iron oxide nanoparticles and assistance on magnetic hyperthermia and Mössbauer spectroscopy. Dr Ghayathri Balasundaram and Dr Amalina Attia deserve thanks for the MSOT analysis and I am always grateful for how patient they were when I needed guidance. I must also thank Michael Ng and Francesca Mandino for aiding in the collection of MRI data.

I must thank all the people I have met, however briefly during this PhD process including the Parkin lab group in UCL and all of SBIC A*STAR in Singapore.

I must thank all my friends and family. My office pals Douglas and Andrew welcomed me wholeheartedly and made my stay in Singapore one of the greatest experiences that I will always look back at with joy.

Lastly, a special thank you to Mum, Dad, and Yuko. You have all always supported me and encouraged me in every step I take and have been by my side to celebrate the wins with me and to hold me steady when times were tough.

Thank you!

CONTENTS

LIST OF FIGURES

LIST OF TABLES

LIST OF EQUATIONS

LIST OF ABBREVIATIONS

AC	Alternating current
ATR	Attenuating total reflectance
C e6	Chlorin e6
CFSE	Crystal field stabilisation energy
cfu	Colony forming unit
CMC	Critical micelle concentration
CV	Crystal violet
DLS	Dynamic light scattering
EDC	1-[3-(dimethylamino)propyl]-3-ethylcarbodiimide hydrochloride
EDX	Energy-dispersive X-ray
eV	Electron volts
fcc	Face centre cubic
FI	Fluorescein isothiocyanate
FOV	Field of view
FTIR	Fourier transform infra-red
FWHM	Full width half maximum
HA	Hyaluronic acid
Hb	Deoxygenated haemoglobin
HbO_2	Oxygenated haemoglobin
IACUC	Institutional animal care and use committee
ICG	Indocyanine green
ILP	Intrinsic loss power
IR	Infra-red
IUPAC	International union of pure and applied chemistry
M.W.	Molecular weight
MACH	Magnetic alternating current hyperthermia
MES	2-(N-morpholino)ethanesulfonic acid
MGITC	Malachite green isothiocyanate

mmPA	Magnetomotive photoacoustic
MR	Magnetic resonance
MRI	Magnetic resonance imaging
MSOT	Multispectral optoacoustic tomography
NIR	Near infrared
NMR	Nuclear magnetic resonance
NP	Nanoparticle
OPO	Optical parametric oscillator
PA	Photoacoustic
PDI	Polydispersity index
PDT	Photo dynamic therapy
PEG	Poly(ethylene) glycol
PEI	Polyethyleneimine
PET	Positron emission tomography
PVP	Polyvinylpyrrolidone
PXRD	Powder X-ray diffraction
RF	Radio frequency
ROI	Region of interest
SAR	Specific absorption rate
SEM	Scanning electron microscopy
SERS	Surface enhanced Raman scattering
SPION	Superparamagnetic iron oxide nanoparticle
SPR	Surface plasmon resonance
SQUID	Superconducting quantum interference device
Sulfo-NHS	N-hydroxysulfosuccinimide sodium salt
TEM	Tunnelling electron microscopy
TMAOH	Tetramethylammonium hydroxide
TNT	Trinitrotoluene
TOAB	Tetraoctylammonium bromide
UV	Ultraviolet
XPS	X-ray photoelectron spectroscopy

1 INTRODUCTION

1.1 OPENING REMARKS

The study of nanoscale materials has undergone a significant boom in recent decades. Thanks to developments in technology, it is now easier than ever to study, measure and analyse the nanoscale range. Within materials chemistry, nanoparticles have rapidly developed in scope and complexity to be potentially considered as the next big breakthrough in science.

With this in mind, this work will be discussing the research involved in the developments of iron oxide nanoparticles for their applications as materials in biomedicine. The thesis will start with a detailed understanding of iron oxide nanoparticles; from the synthetic beginnings to the current downstream technologies. This research here will investigate the synthetic routes of iron oxide formation and enhancement of these nanomaterials for targeted applications through nanoparticle functionalisation.

1.2 NANOSCALE

Nanoparticles; as a relatively new form in materials chemistry, they have seen continuous interest in recent decades. This is due to fascinating and surprising properties accessible through their narrow size range. Nanoparticles are defined by IUPAC (International Union of Pure and Applied Chemistry)[1] as having at least one aerodynamic dimension between 1 – 100 nm resulting in possible structures such as; nanospheres, tubes, stars, rods, and sheets. Their small dimensions result in a larger surface area per unit volume and a higher proportion of surface atoms to bulk. This increases reactivity due to greater numbers of free coordination sites and unsaturated bonds.

The high degree of reactivity means that small changes in the morphology and composition of nanoparticles can result in large variations in physicochemical properties from both related nanoparticle and bulk materials. A common example of this are the optical properties of gold nanoparticles. Nano-sized gold exhibits surface plasmon resonance (SPR) bands in the ultraviolet and visible light wavelengths which vary depending of the size of the nanoparticles.[2]

Due to the high reactivity of nanoparticles, they can be fundamentally unstable. Ligands are therefore utilised to stabilise this surface instability and, complement or modify properties. The effect of these variations is therefore fundamental to the understanding and development of future nano-devices.[3,4] Ligands are typically simply functionalised organic compounds, such as carboxylates, amides and phosphonates. This has fuelled research into diverse applications such as developing novel materials for biomedicine, technology and catalysis.[5–8]

Iron oxide is one material of high interest in the nanoscale range due its intrinsic magnetic properties. The utilisation of this magnetism is currently pushing the research of iron oxide nanoparticles for novel biomedical devices and treatments.

1.3 IRON OXIDE

Iron is a highly abundant first row transition metal element that comes in a wide variety of forms and readily binds to produce oxides, chlorides, and sulphates. Significantly, iron is found within nature as a vital element for life as an electron donor and acceptor in the complex oxygen transporter proteins haemoglobin and myoglobin. As well as being critical in metallurgy for the advancements in early civilisations of the Iron age and in steel alloys today.

As an element, iron has the chemical structure $[Ar]4s^2 3d^6$ and like other transition metals can possess a wide range of oxidation states from -2 to +7, with 0, +2, and +3 being the most stable. This makes iron a very versatile element.

Figure 1.1 shows the crystal field stabilisation energy (CFSE) diagrams for Fe(II) and Fe(III), in high spin configurations. With a d^6 orbital configuration, i.e. 6 electrons in the d-orbitals, Fe(II) will preferentially form octahedral orientations due to the inherently smaller splitting as shown by the equation:

$$\Delta_t = \frac{4}{9}\Delta_o \tag{1.1}$$

The CFSE = -2/5 Δ_o, for octahedral splitting whereas, for the tetrahedral splitting, Δ_t = -3/5 Δ_t, or -6/45 Δ_o.

Fe(III) however can occupy both octahedral and tetrahedral sites. As Fe(III) = d^5 configuration, when in high spin due to the weak field ligands one lone electron occupies each orbital resulting in a net CFSE = 0. Meaning neither octahedral nor tetrahedral sites are energetically preferred.

From the spectrochemical series, weak field ligands – the halides and OH^- – exhibit a low energy splitting to the d-orbitals. This results in high spin configurations being energetically favoured as more energy is required to pair repelling electrons than to put them in high spin orbitals.

Strong field ligands, CN, CO and PPh_3, lead to a greater Δ_o splitting energy making the high energy orbitals increasingly inaccessible and low spin complexes become more energetically favourable (Figure 1.2). Where the energy require to pair the opposite spin electrons is lower than that required to occupy a high spin orbital.

For the iron oxides seen in this thesis, they are coordinated to either Cl^- or OH^-, meaning we will typically be dealing with the high spin states of Fe(II) and Fe(III).

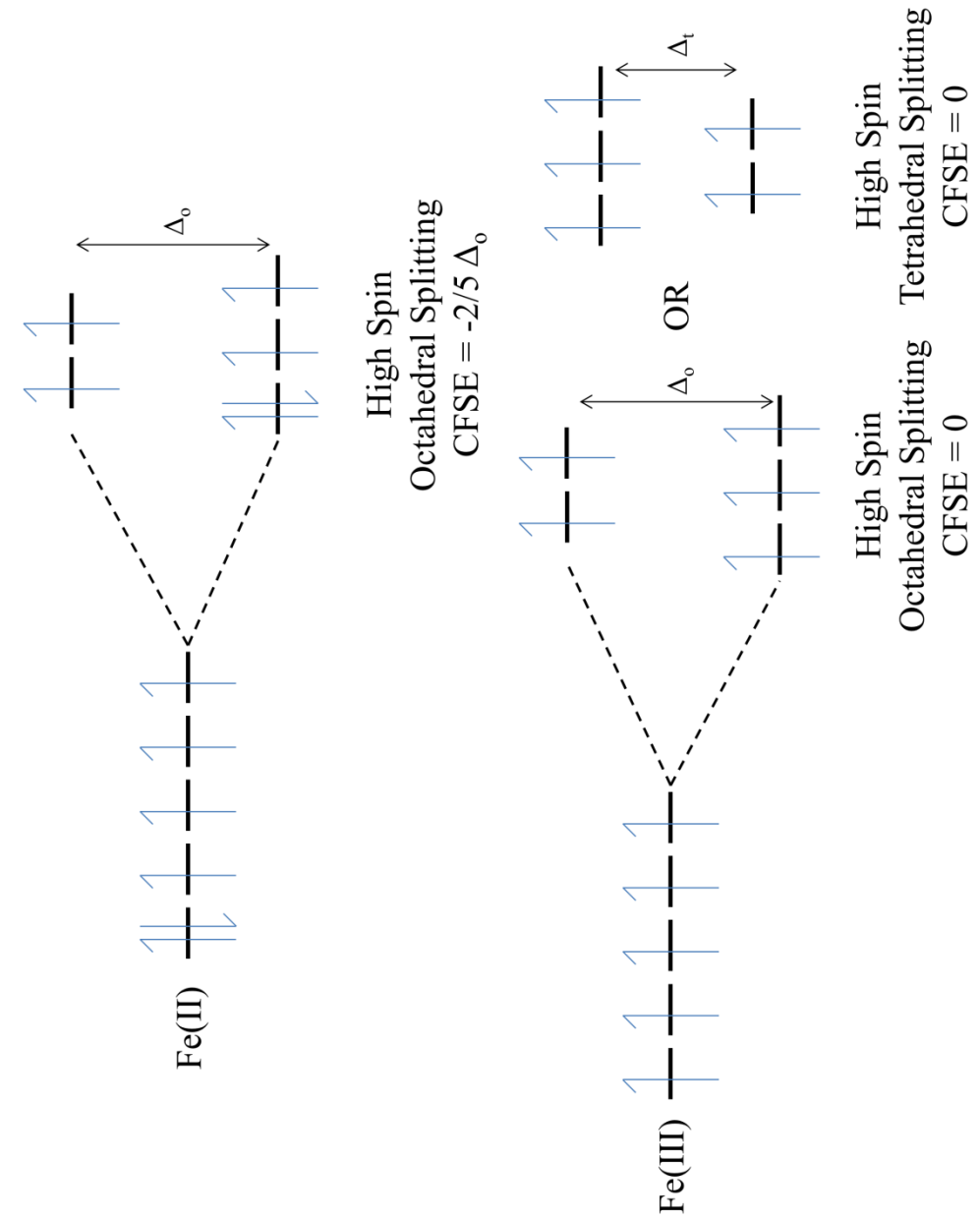

Figure 1.1. Crystal field stabilisation energy (CFSE) of the high spin orbital splitting of Fe^{2+} and Fe^{3+}. Note that Fe(III) can possess both octahedral and tetrahedral sites whereas Fe(II) can only occupy octahedral as it has higher stabilisation energy.

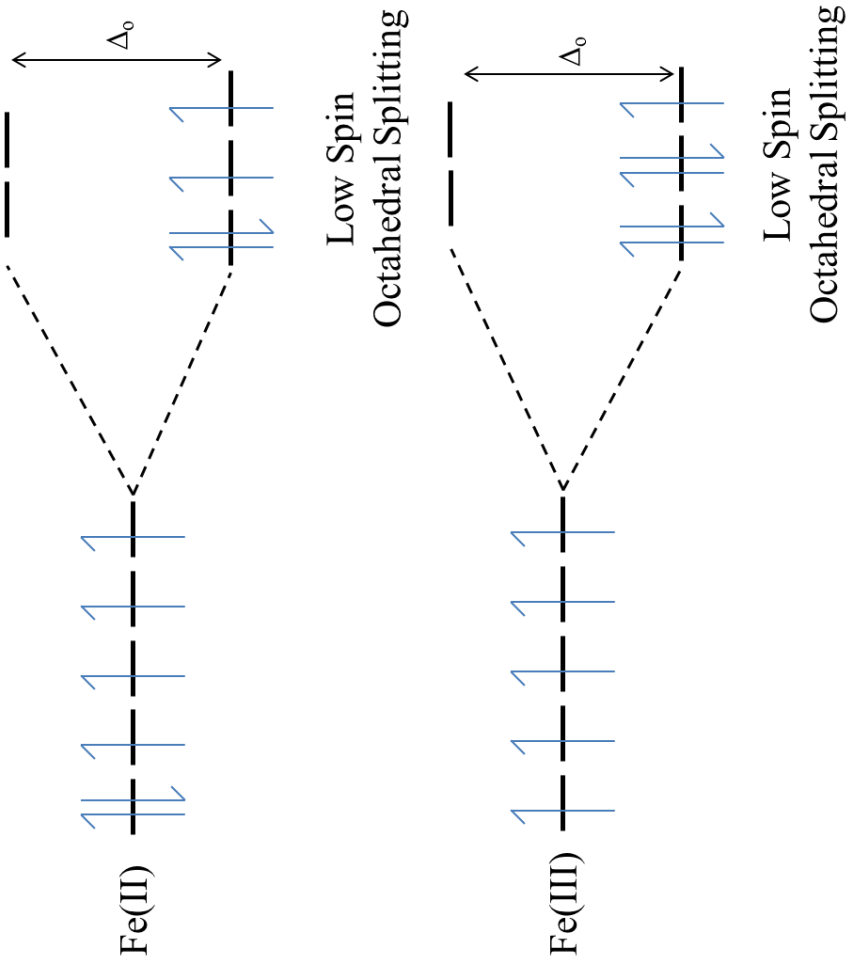

Figure 1.2. Crystal field stabilisation energy (CFSE) of the low spin orbital splitting of octahedral Fe^{2+} and Fe^{3+}. Note that both Fe(II) and Fe(III) only possess electrons in the ground state (t_{2g}) orbitals due to higher Δ_o splitting energy.

In this thesis, iron oxides, specifically Fe_3O_4 and Fe_2O_3 nanoparticles, are the only form of iron considered with iron oxide nanoparticles the major focal point. The nanoparticles will be considered as a basis for developments in biomedicine by manipulating the intrinsic magnetic properties of the iron atoms within the nanostructure. This section will detail the underlying properties of iron oxide and its nanoparticle form.

The high levels of development in recent decades are due to the multitude of beneficial applications within the biomedical sector and in imaging techniques.[5,6,9] These interests arise from the intrinsic magnetic properties that iron possesses, and currently range in the development of superparamagnetic iron oxide nanoparticles (SPIONs) for:

- Drug delivery
- MRI contrast agents
- Magnetic separation
- Magnetic hyperthermia
- Cell separation

To become applicable for such uses, iron oxide needs to be tailored to have high superparamagnetic properties and be suitably stabilised for surface interactions; with chemical solvents, biological media, or towards further functionalisation. Here we will discuss the modifications (see section 1.3.6) which are common to help broaden the scope of these particles through addition of organic or synthetic polymers – i.e. dextran, lauric acid, PEG, PVP[10–12] – or metallic and inorganic colloids – gold, and silica.[13,14] Surface modification also limits the degree of aggregation as without stabilising ligands, iron oxide nanoparticles are hydrophobic. Therefore in an aqueous medium the hydrophobic interaction lead to aggregation and thus increased effective particles sizes and a reduction in paramagnetic properties.[15]

1.3.1 FeO

There are three main compounds of iron oxide that are naturally occurring. Iron(II) oxide, FeO, otherwise known as the mineral wüstite is one of those forms of iron oxide and makes up to approximately 9% of the Earth's mantle. It has a standard cubic lattice structure in which the Fe(II) and O^{2-} atoms occupy octahedral sites. Fe(II) can readily undergo oxidation to Fe(III), making FeO thermodynamically unstable under 850 K and will decay following the equation:

$$4FeO \rightarrow Fe + Fe_3O_4 \tag{1.2}$$

1.3.2 Fe_3O_4

Magnetite, Fe_3O_4, is one of the main oxides of iron found naturally and has received the most interest due its high magnetic potential and its well-known biocompatibility in contrast to other transition metal nanoparticles. This ferromagnetic property arises from the unpaired electrons present in the high spin Fe^{3+} and Fe^{2+} ions which occupy the interstitial tetrahedral and octahedral sites in a face centred cubic (fcc) close packed inverse spinel structure.[16]

This can be shown and written as:

$$[A^{\mathrm{III}}]^{Tet}[B^{\mathrm{II}}A^{\mathrm{III}}]^{Oct}X_4 = [Fe^{3+}][Fe^{2+}Fe^{3+}]O_4 \tag{1.3}$$

Where *A*, represents the Fe^{3+} centres and *B*, the Fe^{2+} centres in Fe_3O_4.

Above a critical temperature, the Curie temperature, T_c, the thermal energy causes the magnetic properties of the material to become disordered (See Section 1.5 on magnetism). For Fe_3O_4, T_c = 858 K at which point the ferromagnetism transitions to paramagnetism.

Fe_3O_4 is not the most thermodynamically stable form and will readily oxidise to form γ-Fe_2O_3.

1.3.3 γ-Fe_2O_3

Maghemite, γ-Fe_2O_3, is the partially oxidised form of Fe_3O_4 and again is superparamagnetic within the nanoscale due to the unpaired electrons present in iron. It also exhibits an inverse spinel structure, but vacancies are present within the octahedral sites.[17]

In the macroscale, Fe_2O_3 has a high Néel temperature of ~950 K, compared to FeO = 198 K. The Néel temperature is analogous to the Curie temperature, only in relation to antiferromagnetic materials and not ferromagnetic. Likewise, it is the increased disorder of the magnetic moments trending towards paramagnetism within the materials.

1.3.4 Nanoscale iron oxide

Iron oxide typically exists in two desired forms at the nanoscale range, Fe_3O_4 and γ-Fe_2O_3, magnetite and maghemite respectively. It has become increasingly

common to produce such particles with the possibility to manipulate the size and shape to tailor the desired properties. Both Fe_3O_4 and γ-Fe_2O_3 possess magnetic moments when particle diameters of < 20 nm are present which are considered to be single domain (Figure 1.3), resulting in superparamagnetic iron oxide nanoparticles.[16]

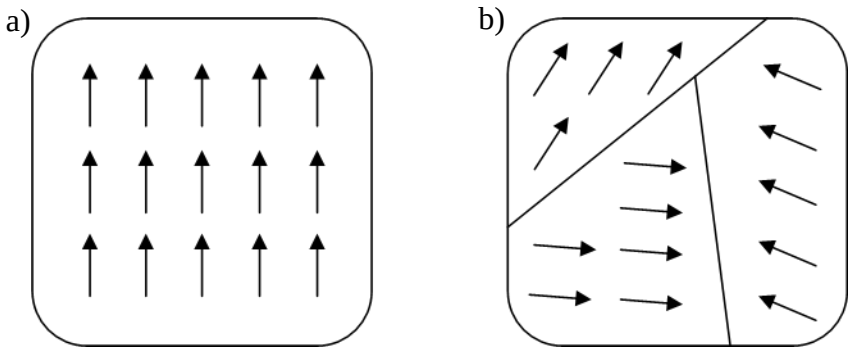

Figure 1.3. Graphic showing the comparison between a) single domain particles and b) multi domain particles.

The magnetisation of iron oxide nanoparticles is considered high, although the saturation magnetisation (M_s) is typically weaker than that of the bulk mineral. Experimental literature values for the M_s of nanoparticles is in the order of 30 – 80 emu/g with bulk Fe_3O_4 having M_s in the order of 100 emu/g.[18]

1.3.5 Synthesis

Iron oxide nanoparticles can be synthesised in a multitude of ways. There are two fundamental ways of creating nanoparticles, top down and bottom up. Top down involves reducing the size of a macrostructure down to the nanoscale. Bottom up is the opposite and involves synthesising nanostructures from their substituents into the desired form.

Here, this chapter will focus on the most common bottom up approaches. With each synthetic route having a large effect on a wide range of physical properties of the nanoparticles, including; size, shape, degree of polydispersity and surface chemistry.

Methods such as sol-gel syntheses,[9,19] microemulsions,[20,21] hydrothermal reactions,[22] and sonochemical reactions[23] are common within literature.

Within these sol-gel syntheses there are several fundamental mechanisms (Figure 1.4) Firstly, nucleation of particles, known as LaMer burst nucleation.[24] This occurs early in the reaction scheme where there are a high proportion of reactants. Generally, the more nucleation points there are, the smaller overall nanoparticles can be. These small nucleation points then precipitate out of the solution when the saturation point has been reached and act as seeds for further reaction. Then there is the growth stage of nanoparticle formation, from small nucleated seeds to stabilised nanostructures. This occurs through the thermodynamic process of Ostwald ripening. This is where small particles dissolve back into solution and re-precipitate onto larger ones. This is due to larger particles being more energetically favourable because of the reduction in surface area.[25,26]

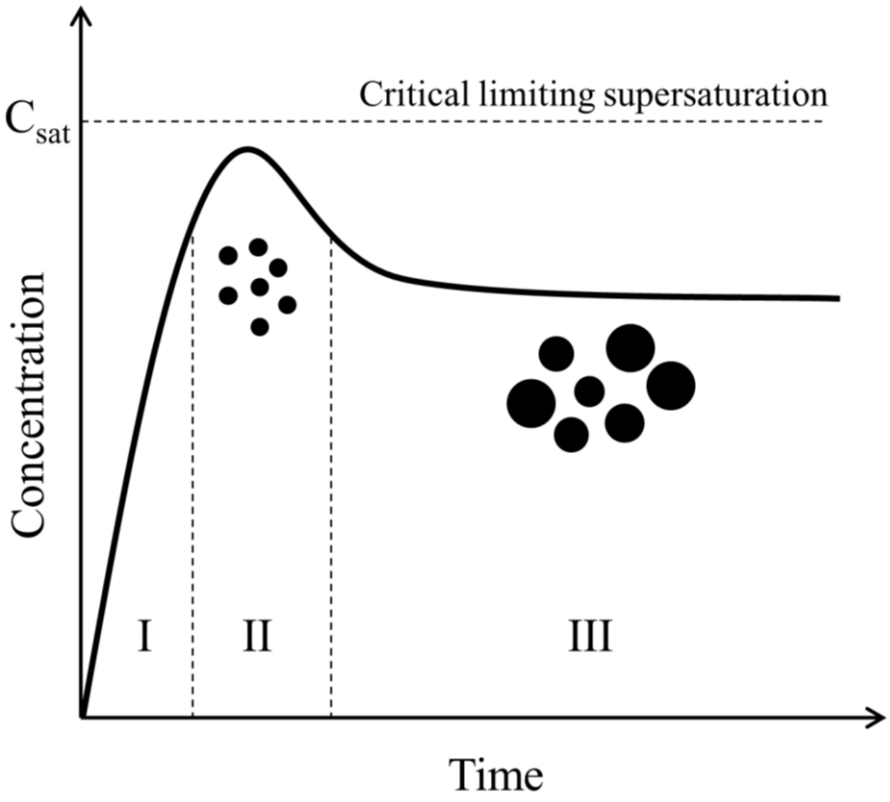

Figure 1.4. Graph showing the three stages of formation of a nanoparticle system from I) pre-nucleaction of monomers, II) nucleation of monomers to particle seeds and III) growth of the nanoseeds into nanoparticles through Oswald ripening. Further aggregation of nanoparticles can occur after growth.

Aggregation of the nanoparticles after the growth stage is also a common problem associated with nanoparticle synthesis that researchers are challenged with. A cluster of nanoparticles will also affect the surface energy and help to stabilise the nanoscale formations.

1.3.5.1 Co-precipitation

Co-precipitation is arguably the most common path for synthesising large scale magnetic iron oxide nanoparticles. It is used as a simple, reliable and cheap method for highly magnetic nanospheres. Typically achieved when dissolving, into aqueous solvent, transition metal salts of varying oxidation number and in the correct stoichiometric ratio. Then under an inert atmosphere, addition of a reducing agent precipitates the nanoparticles.[9] However, fine control over the size distribution is not available due to the kinetic forces at play.

Co-precipitation of iron oxide is increasingly common in literature. Recent developments show Roth *et al.* synthesising a wide range of nanoparticles (3 – 17 nm) with a variable degree of magnetisation from 26 – 89 Am^2kg^{-1}.[27] Furthermore, studies have started to use iron oxide nanoparticles synthesised *via* this route for more clinical applications. . Even more recently, we have seen exciting developments in the use of iron oxide nanoparticles, synthesised *via* a modified coprecipitation method, in the extraction of DNA.[28] Utilising electrostatic interactions, and surface functionalisation using silica or chitosan, it was seen that fast and versatile DNA separation was achievable. This is seen a promising avenue of nanobiotechnology, utilising the physiochemical properties and magnetism of the iron oxide cores.

Thomas *et al.* investigated heating through magnetic hyperthermia and anti-bacterial properties of iron oxide.[9] Concluding that given stabilising agents drastically improve the properties of the nanoparticles, achieving a heating power ((ILP), see section 1.6.1) of 6.1 x 10^{-9} H^2kg^{-1}, and a total kill of over 10^7 cfu

(colony-forming unit) of the bacteria *S. aureus.* Very recently similar research into chitosan functionalised iron oxide has been investigated into its potential antibacterial and antifungal activity.[29] Where here it is proposed that chitosan coated Fe_3O_4 cores could be used as an effective coating material for antimicrobial devices. Iron oxide nanoparticles have also been regularly used for imaging and MRI agents and current research is still developing such nanomaterials.[30,31]

Thermodynamics states that this reaction would precipitate Fe_3O_4 when a stoichiometric ratio 2:1 for Fe^{3+}:Fe^{2+} and a pH of 8 – 14.[32] The reduction reaction of the ferric and ferrous salts is shown as follows:[33]

$$Fe^{2+} + 2Fe^{3+} + 8OH^- \rightarrow Fe_3O_4 + 4H_2O \quad (1.4)$$

As mentioned in section 1.3.2, Fe_3O_4 is not the most thermodynamically stable form of iron, therefore readily undergoes oxidation (Figure 1.5) to a less-favourable product via:

$$Fe_3O_4 + 2H^+ \rightarrow \gamma\text{-}Fe_2O_3 + Fe^{2+} + H_2O \quad (1.5)$$

Ultimately, iron oxide nanoparticles will finally be oxidised to the unfavourable by-product as:

$$Fe_3O_4 + 0.25O_2 + 4.5H_2O \rightarrow 3Fe(OH)_3 \quad (1.6)$$

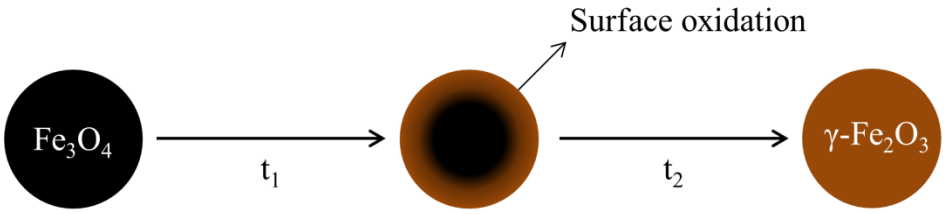

Figure 1.5. Scheme showing the initial surface oxidation of magnetite (Fe_3O_4) nanoparticles to maghemite (Fe_2O_3) over a given time, t_1, and complete oxidation of the particle to Fe_2O_3 after time, t_2, when in an oxygen rich environment.

Alternatively, another common way of forming highly ordered monodisperse iron oxide nanoparticles is *via* organic solution synthesis, as shown by Park *et al.*[34] This typically produces organic soluble iron oxide nanoparticles in high boiling point solvents, i.e. 1-octadecene. The disadvantage of this method being that the formed nanoparticles are only organically soluble due to the oleate coating, meaning that further functionalisation is required to make the iron oxide suitable for aqueous systems. This is also a much harsher synthetic procedure requiring volatile solvents – including hexane and 1-octadecene – and at very high temperatures exceeding 300 ^{o}C.

1.3.5.2 Hydrothermal

Hydrothermal synthesis occurs when the reaction is carried out under increased temperature and high pressures in an autoclave. Iron (II) chloride ($FeCl_2.4H_2O$) is dissolved in an aqueous medium at elevated conditions and NH_4OH is added as a

reducing agent allowing for the oxidation of Fe(II). The advantage of a hydrothermal methodology is the independency on an inert atmosphere and reflux conditions, resulting in more controllable oxidation of the iron.[35]

In 2009, Ge *et al.* synthesised Fe_3O_4 nanoparticles with controllable diameters, narrow size distribution, and tuneable magnetic properties. The particles were synthesised at 140 ^oC and 2 bar to give diameters in the range of 15-30 nm with magnetisation in the range of 53.3-97.4 emu/g.[36] With the ease of tuning the nanoparticle magnetisation, hydrothermal synthesis particles are commonly developed for MRI. Li *et al.* have recently demonstrated the facile synthesis of targeting MRI probes using a hydrothermal synthesis of iron oxide. Targeting was achieved *via* stabilisation by a polyethyleneimine (PEI) mediated approach and fluorescein isothiocyanate (FI) and hyaluronic acid (HA) ligand conjugation. HA-targeted Fe_3O_4 NPs are able to be uptaken specifically by specific cancer cells overexpressing CD44 antigen receptors.[37–39]

1.3.5.3 Micelle

A micelle, as shown in Figure 1.6, is a supramolecular structure formed of surfactant molecules that contain both a hydrophilic ‘head’ and hydrophobic ‘tail’. Due to this difference in hydrophilicity, the lipid will aggregate together to form an equilibrium between two immiscible solvents, the aqueous and the organic. A ‘typical’ (oil-in-water) micelle is in aqueous solution, therefore a monolayer of the hydrophilic head is in contact with the solvent and a hydrophobic organic centre is formed. This forms a nano-droplet within solution and acts as a nano-reactor for

any soluble reactants. A reverse micelle is the opposite orientation or in other-words a reverse of the ratio of aqueous solvent to organic solvent. In this regard, micelle reactions give a high degree of control over the size and shape of nanoparticles including spheres, cylinders and lamella phases.[27]

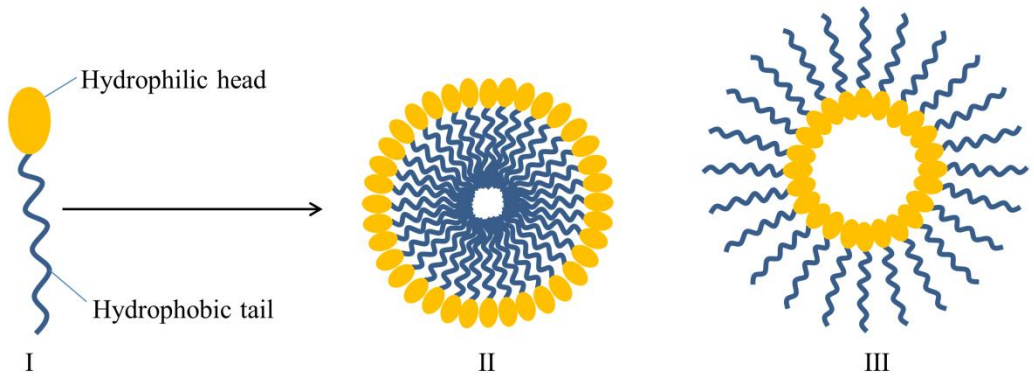

Figure 1.6. Diagram representing I) a surfactant monomer with a hydrophilic head and hydrophobic tail. These monomers for either II) a micelle with an organic solvent centre surrounded by aqueous solvent or III) a reverse micelle where the aqueous solvent is within the micelle.

For the synthesis of iron oxide nanoparticles in micelles, a water-in-oil emulsion is required. The chemistry within the micelles is the same as that of co-precipitation. The iron salts are water soluble however the micelle limits the reaction size resulting in the formation of highly monodisperse nanoparticles. The surfactant can be tailored to produce particles of different sizes and morphologies. *Lee et. al.*[20] have achieved the synthesis of gram-amounts of highly crystalline monodisperse iron oxide nanoparticles in which they are able to maintain the micelle phase.

There are difficulties with a reverse micelle reaction, including the formation of the micelle solution itself. The ratio of solvents to surfactant has to be precise with the surfactant concentration needing to be greater than the critical micelle concentration (CMC). Furthermore, large scale micelle formation of nanoparticles is challenging. A large amount of solvent is required for the synthesis of a relatively small yield and to maintain the micellular structure during the high temperature synthesis.[20]

1.3.5.4 Microwave

Microwave synthesis of iron oxide particles provides requires a closed sealed reaction vessel leading to convenient, reliable, and repeatable synthetic methodology. Heating is achieved through the dielectric effect giving rise to high temperatures at speed making microwave reactions remarkably rapid. Blanco-Andujar *et al.* showed how iron oxide nanoparticles coated with citrate can be synthesised *via* microwave assistance. These particles also proved effective for magnetic hyperthermia giving a high intrinsic loss parameters of up to 4.2 nHm^2kg^{-1}.[40]

By dissolving $FeCl_3.6H_2O$ into a polar solvent (e.g. ethylene glycol) the pressurised microwave reactor causes the rapid heating. The reaction can also be effectively scaled up as no thermal gradient effects are noted within the solvent medium. However, thermal control is difficult leading to 'hotspots' with the reaction and leading to some drastic morphological changes such as Fe_2O_3 nanorings[41] and Fe_3O_4 nanoroses.[42]

Table 1.1: Comparison of the synthetic methods for synthesis of iron oxide nanoparticles showing characteristics of each route.[43]

Method	Complexity	Conditions	Temperature/ °C	Time	Size Distribution	Shape control	Yield
Co-precipitation	Very Simple	Inert atmosphere	50-150	Minutes	Narrow	High	High
Thermal decomposition	Complex	Inert atmosphere	100-350	Hours	Very narrow	Very high	High
Hydrothermal	Simple	High pressure	150-220	Hours	Very narrow	Very high	High
Micelle microemulsion	Complex	Ambient	20-80	Hours	Narrow	High	Low
Microwave assisted	Simple	Ambient	100-200	Minutes	Medium	High	Good
Biosynthesis	Complex	Ambient	Room temp.	Days	Broad	Poor	Low

Form Table 1.1, it is therefore possible to establish the most suitable reaction mechanism, however this is all dependant on the overall properties of the iron oxide that are desired. In this research, the co-precipitation reaction was the most desirable, giving a narrow size distribution whilst having little synthetic complexity and yielding aqueously soluble nanoparticles.

Thermal decomposition is another widely used synthetic route to highly desirable iron oxide nanoparticles. This is the least complex method of forming highly monodispersed nanoparticles with finely tuned morphologies. However, the particles are often stabilised with an organic surfactant, oleic acid[34], which for use in biological systems, requires multiple synthetic steps to achieve ligand functionalisation.

In this thesis, I will mostly explore the potential of the co-precipitation reaction for the reasons mentioned above. However, interest is high in the preparation of highly monodisperse particles; therefore, you will also see attempts at using this method.

1.3.6 Coatings and stabilisation

One of the most important factors to consider when synthesising nanoparticles is the surface coating and stabilisation.[16,43,44] For iron oxide nanoparticles this retains the uniform monodisperse nature in both biological and magnetic environments preventing aggregation of the colloidal ferrofluid. There requires an equilibrium between the attractive and repulsive electrostatic forces, the repulsive steric hindrance between individual nanoparticles and, in magnetic nanostructures,

the magnetic dipole attractions. To achieve this equilibrium manipulation of charged electrostatic forces or the steric repulsion is necessary.

1.3.6.1 Monomeric ligands

One of the most common stabilising agents developed by Turkevich *et al.*[45] and still in use widely today is citrate ions *via* the addition of sodium citrate or citric acid. The surface of nanoscale iron oxides acts much like a Lewis acid and will readily accept a donated electron lone pair. In an aqueous medium this results in coordination and hydroxylation of the surface iron ions. Likewise, it has been shown that citrate will bind effectively to the surface of magnetite through the coordination of one or two of the carboxyl functional groups available. Due to the structure of citrate, this leaves an exposed carboxylate group resulting in a surface that is negatively charged and hydrophobic. Other monomeric ligands that can stabilise iron oxide nanoparticles are sulfates and phosphates as shown by Thomas *et al.*[9] and Sahoo *et al.*[46,47]

1.3.6.2 Organic polymers

Encapsulation of nanoparticles with polymers is seen as an effective way to achieve bio-stability and nontoxicity. Encapsulation can be achieved *in situ* during the growth of the particles or post-synthesis for example the functional PEG coated SPION's for *in-vivo* MR imaging developed by Lee *et al.*[48] The most

common polymers derivatives seen in literature are polyethylene glycol (PEG), chitosan and dextran.

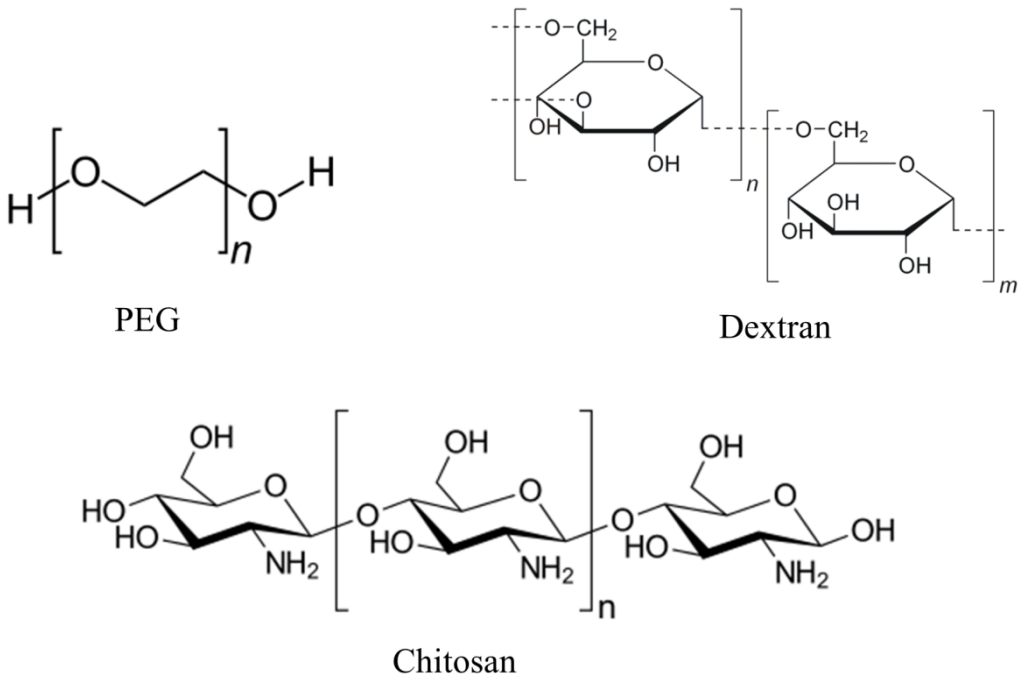

Figure 1.7: Chemical structures of the common stabilising polymers polyethylene glycol (PEG), dextran and chitosan used for increasing nanoparticle stability and biocompatibility.

These polymers are highly flexible and water soluble with well-known biocompatibility, and many publications report on the use of encapsulation to improve the biocompatibility and retention times of nanoparticles. An important factor in the choice of polymers, especially dextran, appears to be the favourable size of the chains, up to 40000 Daltons. This can enable optimum polar interactions through chelation and hydrogen bonding with iron oxide surfaces.

However, encapsulation is generally a physical process, in which there are no covalent interactions there is concerns about desorption of the polymer chains and break up of structures, i.e. release of the nanoparticles from inside the polymer.

1.3.6.3 Inorganic shells

Several inorganic materials and metals have been reported to aid in the stabilisation and functionality of iron oxide nanoparticles. Silica has been greatly exploited for the coating of iron oxide predominantly for its inert qualities and high controllability. A silica coating will also reduce aggregation by creating shielding of the magnetic dipole attraction.

As such, Jang *et al*. have synthesised an iron oxide – silica core shell nanoparticle conjugated with a fluorescent dye for use an imaging probe.[49] The single iron core of ~13 nm diameter is coated with silica of between 5 – 50 nm thickness. The silica, as well as being a stable surface for dye conjugation provided protection to fluorescent quenching from the iron oxide core.

Gold is another inorganic material that has seen recent interest in the coating of iron oxide nanoparticles. Like silica, gold is a very inert and biologically stable material, making it ideal for the bio-protection of nanoparticles, whilst giving a basis for further organic functionalisation. Another benefit for a gold coating is the inherent optical properties of gold (see section 1.4). Briefly, gold has long been used in biomedical imaging and sensing. To combine and synergise the optical advantages of gold with the high intrinsic magnetisation of iron oxide nanoparticles is highly desirable. However, given the surface energy of oxides is

typically lower than that of a metal, a continuous homogenous coating of gold is difficult to achieve.

There are literature reports for the synthesis of iron oxide – gold nanostructures most notably that of Lyon *et al.* which showed the synthesis of gold coating onto iron oxide nanoparticles through iterative hydroxylamine seeding. Fe_3O_4 was synthesised in a co-precipitation method being reduced with NaOH with the addition of $HAuCl_4$ and hydroxylamine promoting an Au^{3+} surface catalysed reduction, rather than monometallic Au particle nucleation.[50] From personal attempts of this method, it becomes evident that the mechanism for the gold coating is highly unpredictable and often unreliable.

In light of the benefits and challenges that arise from inorganic coatings of magnetic nanoparticle cores there are several defined morphologies. Firstly there are core – shell particles in which an individual iron oxide core is coated wholly by the functional coating material.

Dumbbell or Janus morphologies are seen when one side of the nanostructure consists of iron oxide and the alternate side consistent of the functional material, such as two individual nanoparticles joined together.

This has been shown by Yu *et al.* who demonstrated an Au-Fe_3O_4 nanostructure made up of a 2 – 8 nm magnetic iron oxide particles bound to an individual 5- 20 nm diameter Au particle. This structure is formed *via* epitaxial growth of iron oxide on the Au seed particles.[51] Xu *et al.* further developed the dumbbell particles as a nanocarrier for therapeutic platin molecules.[52] Again, these

mechanisms are highly complex and need to be very specifically formulated to get the tailored nanostructures repeatedly and uniformly.

1.4 GOLD

The precious metal, gold, as well as being highly sought after in its macroscale is also a valuable material when looking into nanoscale properties. The section will discuss the benefits of gold, and specifically optical and chemical properties.

Gold has been known to be used in its nanoscale form for millennia. Earliest examples are of decorative red coloured glass, such as the 4th century roman Lycurgus Cup. This ornate vessel has colloidal gold and silver within the glass material forming a dichroic effect. An effect which causes the glass to display and undergo a colour change when in varying lighting conditions. When lit from the front, a green colour is seen, but from behind, a red colour is displayed due to the difference in wavelength absorption of the nanoparticles. Similarly, gold nanoparticles have been used in stained glass windows and cranberry glass which forms a distinctive red or pink colour.

In the 1850's Michael Faraday was the first to synthesize a pure sample of colloidal gold and study the optical properties, coming to the conclusion that small gold nanoparticles were causing the refraction of different wavelengths of light, also known as the Tyndall effect.

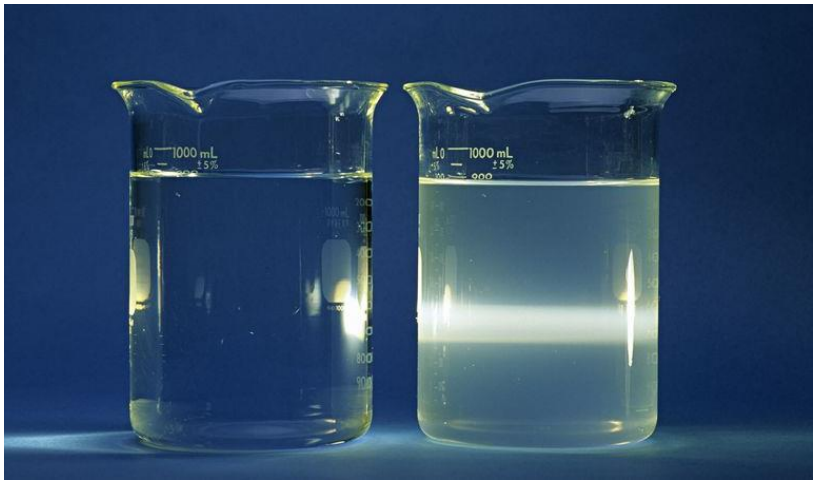

Figure 1.8. Photo showing the Tyndall effect, in which the light beam passes through the pure solution (left) and is refracted due to the presence of nanoparticles in the colloidal suspension (right) thus making the beam of light visible[53]

Likewise, gold has been used in medicine for generations. First seen in text by Pliny the Elder (AD 23-79), he describes the properties and formulation of gold remedies. Later, In the Middle Ages, alchemists used gold as a curative treatment for various different diseases through drinkable gold – 'Aurum potabile' – and as a youth tonic.

In more modern times, technology has advanced leading to greater detail and comprehensive studies on gold nanoparticles in medicine. The optical surface plasmon resonance effect (SPR) properties of gold nanoparticles are key for the development of medical applications. SPR is the diffraction of an incident wave caused by the excitation of the surface plasma waves in a metal.[54,55] At optical wavelengths, this is found in gold and silver. It is therefore ideal for measuring the

refractive index of very thin layers of mater on a metallic surface, including bio-markers and antibodies in chemical sensors.[56]

Gold nanoparticles have also been utilised by MSOT and photoacoustic imaging due to these strong and highly tunable absorption bands.[57,58] There are a wide range of morphologies that are achievable through the synthesis of gold nanostructures; all with a highly specific absorption wavelengths from anywhere between 520 – 2000 nm. Including nanospheres, nanorods, nanostars, and nanoprisms.[59–62] This wavelength variation is critical for the nanoparticle NIR absorption in the wavelength range of the 'biological window' (650–1100 nm), where the least amount of biological attenuation occurs.[63]

Furthermore, the optical properties of gold can be used for therapeutic means in photodynamic therapy (PDT). Where red light (600 – 700 nm) is theorised to excite a photosensitizer which, through an energy transfer, excites ground state triplet oxygen into excited singlet oxygen ($^1O_2$) radicals. If uptake in a malignant tumour is great enough, the singlet $^1O_2$ will react with and chemically destroy the cells. Hone *et al.*[64] reported that phthalocyanine stabilised nanoparticles can be used as a safe reliable photosensitiser and Srivatsan *et al.*[65] further enhanced the efficiency of PDT by using a gold nanocage to act as both a photosensitizer and for photosensitizer drug delivery.

The reactivity of gold is highly significant to its wide use in these biomedical applications, most notably, the affinity of sulfur to metallic gold.[66] This is well observed in the surface functionalisation of gold nanostructures with thiolated polymers, commonly thiol functionalised poly(ethylene) glycol (PEG-SH)[67,68].

The thiol functional group provides facile and effective coordination to the metal core whilst the polymer, as with FeO surface functionalisation (Section 1.3.6), can have inherent properties, such as targeting moieties and high bio-compatibility and bio-stability.[69]

1.4.1 Synthesis

The simplest and most common synthetic route to gold nanoparticle synthesis is that pioneered by Turkevich *et al.* in 1951.[70] Aqueous gold ions (Au^{3+}, from chloroauric acid ($HAuCl_4$)) are reduced to metallic gold (Au^0) *via* the addition of a reducing agent, sodium citrate. Au^0 atoms will act as nucleation points for the further reduction of Au^{3+} thus forming nanoparticles, which are then stabilised from aggregation and excessive growth through capping from the citrate ligands.

This forms the characteristic ruby red colour of gold colloid solution with the particles of good monodispersity and having a mean diameter in the range of 5-20 nm. To vary this diameter alteration can be made to the percentages of reagents used but above 50 nm the citrate stabilisation is ineffective and polydispersity arises.[71] However, Bastús *et al* achieved gold particles upwards of 180 nm in dimeter using citrate stabilisation following a kinetically controlled seed mediated growth.[72]

Another viable synthetic route to gold nanoparticles is through the Brust-Schiffrin method.[73] Wherein $HAuCl_4$ undergoes a phase-transfer from aqueous to organic solvent (toluene) *via* a phase-transfer reagent such as tetraoctylammonium bromide (TOAB). Reduction of Au^{3+} to Au^0 is then achieved with a sodium

borohydride ($NaBH_4$) reducing agent and reliably produces large quantities of relatively monodisperse samples of small nanocrystals (1-6 nm) and facilitates a one pot synthesis for thiol functionalised nanoparticles (Au-SR).[74] This can been as the chemical equations:

$$HAuCl_{4(au)} + TOAB_{(org)} \rightarrow HAuCl_{4(org)} \tag{1.7}$$

$$HAuCl_{4(org)} + R\text{-}SH_{(org)} + NaBH_{4(aq)} \rightarrow Au\text{-}SR_{(org)} \tag{1.8}$$

1.5 MAGNETISM

Magnetism is a physical phenomenon that has been widely recognised since the ancient Greeks, in naturally occurring Fe_3O_4 (lodestone). It is where materials are affected by a magnetic field which arises from the quantum nature of electrons within the atoms. An electron has a very small magnetic dipole moment, defined as the torque experienced on a vector when subject to an external magnetic field which arises from quantum electrodynamics. As a magnetic field is the product of a moving electrical current and electrons are charged (-1e, where *e* is the unit of elementary charge (q = 1.60217662 × 10^{-19} coulombs)) a magnetic dipole is formed when it spins, thus creating a magnetic field.[75]

The magnetic fields are donated by $\boldsymbol{B}$ or $\boldsymbol{H}$-fields which are closely related and are proportional to one another. Where in a vacuum;

$$\boldsymbol{B} = \mu_0 \boldsymbol{H} \tag{1.9}$$

With μ_0 is the permeability of free space, i.e. the degree of resistance to the formation of a magnetic field in a classical vacuum.

Within a material, the magnetic susceptibility, χ_m, indicates whether a material will be attracted to or repelled from a magnetic field through the equation:

$$\chi_m = \mu_m - 1 \tag{1.10}$$

Where μ_m is the magnetic permeability of the material. A positive χ_m results in attraction to a magnetic field, such as a paramagnet, whereas a negative value leads to repulsion as seen in a diamagnet.

These magnetic materials follow the Curie law, which states that the magnetic susceptibility is inversely proportional to the temperature.

$$\boldsymbol{M} = \chi_m \boldsymbol{H} = \frac{C}{T}\boldsymbol{H} \tag{1.11}$$

Here, C is the Curie constant, and the resultant magnetism, $\boldsymbol{M}$, increases when the temperature, T, decreases. Alternatively, when T increases the thermal energy disrupts the alignment and net magnetisation decreases. This temperature is called the Curie temperature (T_C).

When the electron shells of an element or material are full, the individual magnetic moments are then cancelled by their opposite electron. Therefore only

materials with partially filled orbitals form a net magnetic moment. Magnetism is a physical property that is governed by environmental conditions, such as temperature and humidity. This section will discuss the multiple forms of magnetism, with the most commonly seen being diamagnetism, paramagnetism, ferromagnetism, antiferromagnetism and ferrimagnetism.[76,77]

1.5.1 Diamagnetism

Diamagnetism is the most observed form of magnetism, although not the most familiar, as it is present in all materials. It arises from paired electrons and induces repulsion when applied to a magnetic field. Diamagnets have small magnetic susceptibility, and other forms of magnetism will dominate, so only when it is the only contribution to the magnetism can a material be classed as a diamagnet. The magnetic susceptibility is negative resulting in repulsion from a magnetic field. Bismuth is the only naturally occurring diamagnet and superconductors are prime examples of perfect diamagents (χ_m = -1), where given the correct conditions can cause total repulsion of the magnetic fields from the inside of the material thus causing levitation.[78,79]

1.5.2 Paramagnetism

Paramagnetism occurs from the unpaired electrons within an atom. In a paramagnet, the magnetic moments are initially randomly orientated as thermal motion is great enough to overcome the weak order of magnetism. Upon the introduction of an external magnetic field, the magnetic spins align with the applied field forming internally induced magnetic fields (Figure 1.9). This is an attractive force between the external field and the induced fields due to the small but positive magnetic susceptibility, where $\chi_m > 1$. When the external magnetic field is removed, there is no longer any influence over the internal moments and the magnetic properties are not retained.

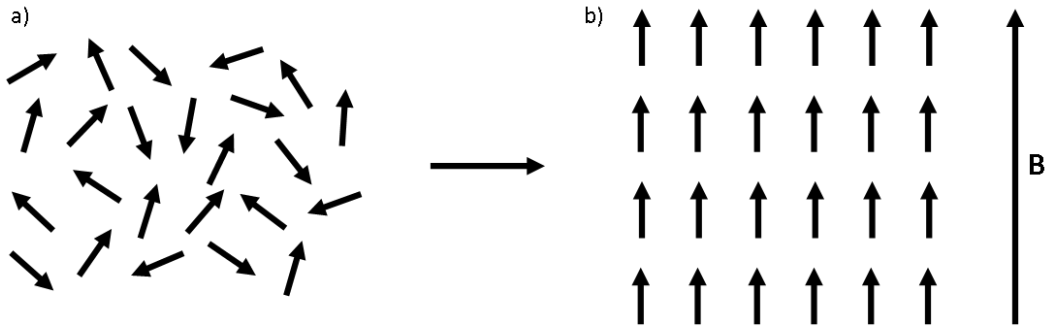

Figure 1.9. Schematic of a) randomly orientated magnetic moments in a paramagnet resulting in zero net magnetisation and b) the alignment of the magnetic moments when an external field is applied. B denotes the direction of the applied magnetic field.

1.5.3 Ferromagnetism

Ferromagnetism is the strongest and most commonly recognised form of magnetism. It is exhibited when a material has a permanent magnetic moment from when the individual magnetic moments within the material align forming a long range order to the magnet. The parallel magnetic moments are then in a preferred lower-energy state and remain the magnetism.

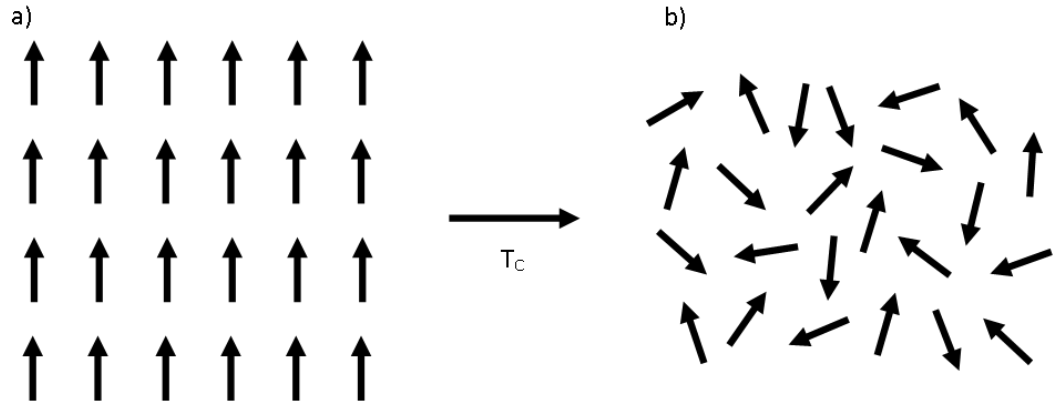

Figure 1.10. Schematic showing a) the alignment of the individual magnetic moments in a ferromagnetic material and b) The effect of the Curie temperature (T_C) on randomising the magnetic moments.

The Curie temperature (T_C) is the critical temperature at which the intrinsic magnetic moments are no longer perfectly aligned (Figure 1.10). This is caused by the thermal energy applied being greater than the decrease from the ferromagnetic ordering. Some of the most common ferromagnetic atoms are Co, Fe and Ni.

1.5.4 Anti-ferromagnetism

Antiferromagnets occur when the magnetic moments align in an antiparallel order. The moments are of equal value therefore there is no net magnetisation in the material (Figure 1.11). This occurs bellow the Néel temperature (T_N, which is synonymous to the Curie temperature, and typically occurs in the order of 10 – 100 K.

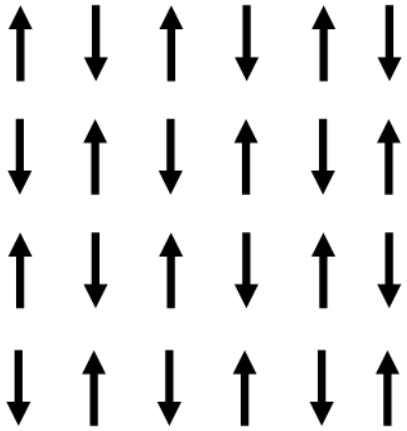

Figure 1.11. A schematic of the magnetic moments present in an antiferromagnet bellow the Néel temperature, which results in a net zero magnetic field as the opposing spins cancel.

1.5.5 Ferrimagnetism

Similarly to antiferromagnetism, ferrimagnets have antiparallel magnetic moments; however, the opposing spins do not have the same magnitude (Figure 1.12). This difference in environments results in a net magnetic moment. For a ferrimagnet, when the thermal energy is great enough it will overcome the short range order of the magnetic moments resulting in randomised magnetic moments

and no overall net magnetisation. This is known as the ferrimagnetic Néel temperature (T_{fN}).

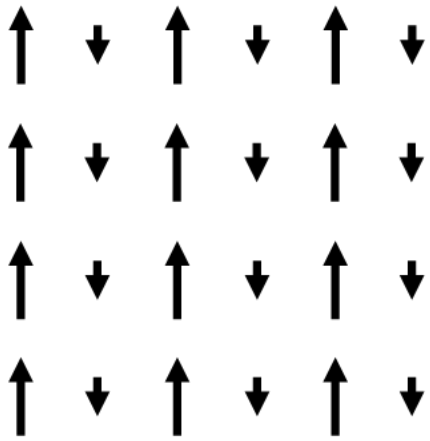

Figure 1.12. Schematic of the spin alignment present in a ferrimagnet. The opposing spins have a lower magnitude resulting in a net magnetic field.

1.5.6 Hysteresis

Magnetic hysteresis (Figure 1.13) is a phenomenon in which magnetic dipoles in a ferromagnet align themselves with an external magnetic field. This demonstrates that the magnetisation, $\boldsymbol{M}$ (Am^{-1}), is not proportional to the applied field, $\boldsymbol{H}$. After magnetic saturation (M_0) is reached, the magnetic dipoles retain a degree of magnetisation, known as the remanent saturation, m_{rs}, and therefore do not fully relax back to zero. M_0 can therefore be seen as a sum of all the magnetic dipoles in a material. Applying $\boldsymbol{H}$ in the opposite direction can manipulate the dipoles back to zero. The degree of $\boldsymbol{H}$ required to reduce $\boldsymbol{M}$ back to its zero value is known as its coercivity, h_c.[76,77]

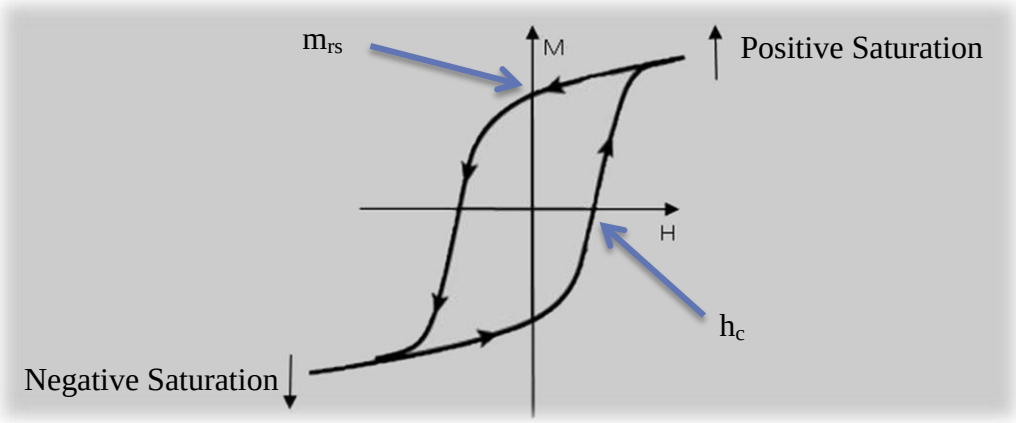

Figure 1.13. Graph showing magnetic hysteresis in a ferromagnetic material and the effect of an external field. Intensity of the applied magnetic field, magnetisation of the material, remanent saturation and coercivity are all displayed.

Hysteresis can then be used to categorise different types of magnetic materials; between hard and soft magnets. Hard magnets have a wide hysteresis loop, which denotes that a large h_c is present. This means a larger external field is required to neutralise the magnetisation. This has therefore become a key component of digital storage[80] whereby soft magnets have a narrow hysteresis and small values of h_c meaning they can be easily demagnetised.

In a single-domain particle, due to the magnetic anisotropy, there is time dependant relaxation of the two stable antiparallel dipole orientations. Known as Néel relaxation (τ_N), it is the mean time taken for the magnetic dipole vector to alternate between these energy minima due to thermal fluctuations and is given by the Néel-Arrhenius equation:[81]

$$\tau_N = \tau_0 \exp\left(\frac{KV}{k_B T}\right) \tag{1.12}$$

Where τ_N is the attempt time of the material (typically between 10^{-9} – 10^{-10} s), K is the magnetic anisotropy energy density, V is the particle volume, k_B is the Boltzmann constant and T is temperature.

1.6 BIOMEDICAL APPLICATIONS

As previously mentioned, iron oxide nanoparticles have great potential as biomedical applications. Here, magnetic alternating current hyperthermia (MACH) and the medical imaging techniques of multispectral optoacoustic tomography (MSOT), magnetic resonance imaging (MRI), and surface enhanced Raman scattering (SERS) are the main focus of this study.

1.6.1 Magnetic AC hyperthermia (MACH)

The process of MACH causes localised heating when magnetic nanoparticles are subjected to an alternating magnetic field. This has been proven to be helpful in the treatment and necrosis of tumorous cells and bacteria.[9,82] When the SPIONs are placed into an AC (alternating current) magnetic field the magnetic moments align with the field. As the field alternates it causes the magnetic vector to flip which provides energy to the particles and *via* hysteresis excess energy is transferred to heat. This is known as Néel rotation. Brownian rotation, a random physical rotation and movement of a particles in solution, also provides some

small amount of frictional heating as well.[83] Brown also devised that the Néel relaxation will possess randomised Brownian motion about the magnetic equilibria. This combination of heating is therefore known as Néel-Brownian rotation.[84,85]

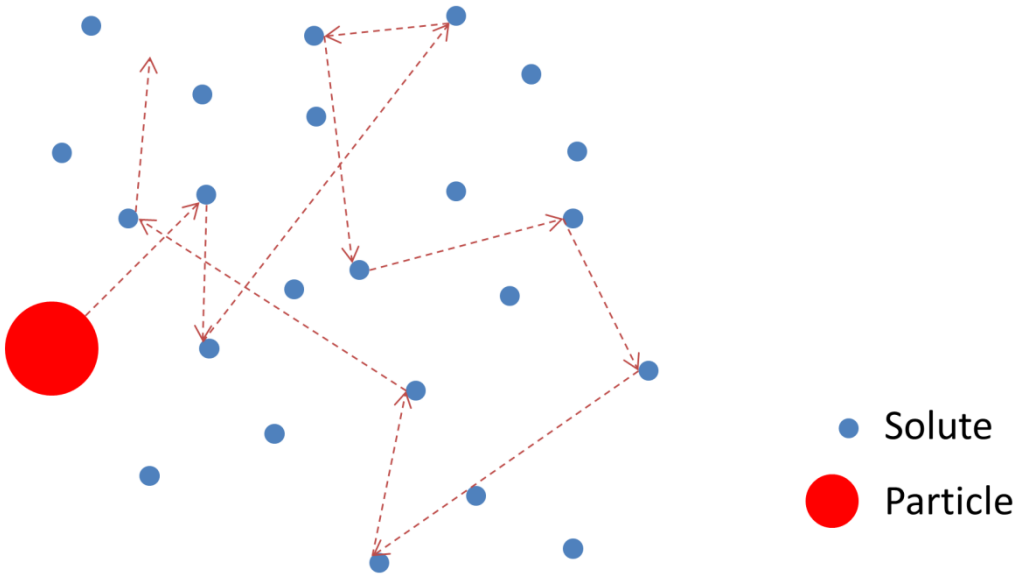

Figure 1.14. Scheme of Brownian motion, showing the completely randomised motion of a nanoparticle as it moves through and interacts/collides with the solute.

Localised heating of 41 – 56 ^{o}C can cause damage and ultimately lead to necrosis malignant cells at long exposure times.[86] SPIONs can also be used cooperatively with chemotherapy drugs for this heating and increases the blood flow to the cells which in turn increases the effectiveness of the drugs.[87,88] This ability for the nanoparticles to heat is typically recorded *via* the specific absorption rate (SAR) or the intrinsic loss power (ILP).[89] SAR shows the amount of energy absorbed

per unit mass when affected by an AC magnetic field and is shown by the equation:

$$SAR = \frac{\Delta TC}{tm_{Fe}} \tag{1.13}$$

Where ΔT is the change in temperature of the sample, C is the specific heat capacity of the material, t is the time over which the AC field is applied and m_{Fe} is the mass of the iron.[90,91]

This is then related to the IPL via:

$$ILP = \frac{SAR}{H^2 f} \tag{1.14}$$

Where H is the power of the alternating magnetic field and f is the frequency of said field.[91] This removes the dependence of the field strength and frequency from the SAR, which gives an easily comparable value for measuring hyperthermia across different systems.[89]

In the literature, previously synthesised commercial magnetic nanoparticles have an ILP of 0.15 – 3.1 nHm^2kg^{-1}, with Bayer-Schering's Resovist nanoparticles having the greatest ILP. It is also currently the only medically approved ferrofluid for use in clinical trials.[90]

Blanco-Andujar *et al.* has also synthesised citrate stabilised iron oxide nanoparticles through microwave synthesis.[23] This produced iron oxide nanoparticles with an ILP of up to 4.1 nHm^2kg^{-1} at a diameter of 17.1 nm.

Tiopronin stabilised iron oxide nanoparticles have been synthesised by Thomas *et al.* producing an iron oxide particle with a high ILP of 6.1 nHm2kg-1.[9] These nanoparticles were then shown to be powerful antimicrobial solutions. The particles themselves showed no antimicrobial activity, only when an alternating magnetic field was applied.

Kossatz *et al.*[92] has recently synthesised, *via* aqueous co-precipitation, magnetic nanoparticles with an ILP of 8.7 nHm^2kg^{-1}. They then showed good response to magnetic hyperthermia in animal tumours studies.

There have been several detailed reviews and studies into the desired location of the SPION's for the effectiveness of hyperthermia treatments.[82,93,94] Intravenous injection of the particles into the blood stream with an external magnetic field can manipulate the particles to a desired site. Although, it has been shown that foreign iron oxide in the blood stream is quickly removed by the liver. This means a longer retention time is required to achieve an effective dosage at the tumour.[94] Surface functionalisation of the iron oxide nanoparticles with a cancer binding drug would also give the particles specificity over where it binds. It is also possible for direct intratumoral delivery, which is beneficial to sites which are easily accessible and in regions where there is low blood flow such as Glioblastoma – a grade IV astrocytoma.[82] Currently there is a clinical patient study in Germany, Europe where magnetite nanoparticles are being used in conjunction with radiotherapy.[93]

In this thesis will be a discussion towards a way of synthesising and using a gold shell coating onto an iron oxide core to help improve stability, functionality and

hyperthermia properties (See Chapter 2). It has been shown by Li *et al.*[13] that gold concentrations are important to the morphology of the Fe_3O_4–Au colloids. We now want to see how different morphologies can affect the magnetism and the ability of heating *via* magnetic hyperthermia.

1.6.2 Multispectral optoacoustic tomography (MSOT)

MSOT is a technique that makes use of photoacoustic properties of a molecule.[95] Fundamentally, a laser pulse of given wavelength is absorbed by a molecule. This molecule then oscillates due to the increased energy and the molecule propagates a sounds wave. The frequency and amplitude of the sound waves can then be detected *via* an inducer and provides detailed information about the propagation of the sounds waves. This wavelength (λ) and positional ($\boldsymbol{r}$) dependency produces multispectral optoacoustic images, $P(\boldsymbol{r}, \lambda)$, which gives a non-linear relationship with respect to the concentrations of the absorbing molecules. This can be shown through the equation:

$$P(\boldsymbol{r},\lambda) = C(\boldsymbol{r})\Phi(\boldsymbol{r},\lambda) \cdot \sum_i c_i(\boldsymbol{r})\varepsilon_i(\lambda) \tag{1.15}$$

Where $C(\boldsymbol{r})$ is a scaling factor with respect to the system effects and the photoacoustic efficiency (Grüneisen parameter $\Gamma(\boldsymbol{r})$),[96] $\Phi(\boldsymbol{r},\lambda)$ represents the wavelength dependant optical fluence, $c_i(\boldsymbol{r})$ is the associated concentrations at position $\boldsymbol{r}$, and $\varepsilon_i(\lambda)$ is the wavelength dependent molar extinction coefficients.[97] Ultimately, due to the Grüneisen parameter, this means that the photoacoustic effect is very sensitive to the external environment factors. As such, a change in

temperature or pressure can greatly affect the photoacoustic properties of any material.

For the multispectral optoacoustic tomography generation, briefly, a tuneable optical parametric oscillator (OPO) pumped by an Nd:YAG laser provides excitation pulses with a duration of 9 ns at a repetition rate of 10 Hz with a wavelength tuning speed of 10 ms and a peak pulse energy of 100 mJ at 730 nm. Ten arms of a fibre bundle provide even illumination of a ring-shaped light strip of approx. 8 mm width. PA signals were acquired using a 512-element concave transducer array spanning a circular arc of 270°. During MSOT measurements, the phantom is translated through the transducer array along its axis to acquire the transverse image slices set.

Due to this, MSOT is rapidly becoming an attractive bio-imaging tool due to the ability to generate anatomical images with a deep penetration depth (5-6 cm) whilst keeping a high spatiotemporal resolution, all while being a non-radiative process.[98] Typically; a short wave near-infrared (NIR) source pulses and irradiates the biological tissue and photoacoustic (PA) probe. The NIR pulse is absorbed, which generates a small temperature spike resulting in the generation of low scattering sound waves *via* thermoelastic expansion in the tissue medium and the probe molecule. Ultrasound transducers detect the incoming acoustic waves which can then be processed into ultrasound images.[99] One beneficial property of an exogenous PA dye is the ability of spectral unmixing. Endogenous molecules such as oxy (HbO_2) and deoxy-hemoglobin (Hb), melanin and water all exhibit a characteristic photoacoustic spectrum.[100] Because of this, literature studies typically use NIR photoacoustic (PA) dyes, with absorption in the region of 700 –

1000 nm. Most commonly used dyes are aromatic organic structures, such as indocyanine green (ICG)[101,102], methylene blue, thalocyanine[103], and chlorin e6[104]. Gold nanomaterials have also been developed to make use of their high degree of optical absorbance, such as in gold nanorods. Nanorods are critical because the increased length in one dimension gives rise to a higher wavelength of absorption than spherical particles of upto 800 nm.[105]

With MSOT, it is then possible to track the dye and analyse specific cellular or molecular processes. Therefore a useful tool for the imaging of tissue oxygenation and hypoxia, and blood vessel imaging for the likes of vascular disease or melanoma.[106]

Photoacoustic imaging is becoming a popular modality in conjunction with other modalities to provide complementary information. The advantage of a dual modality MSOT-MRI probe is to provide the combination of detailed functional and molecular information from MSOT with the very high anatomical resolution given by MRI imaging. Kircher *et al*. have shown the development of a multimodal nanoparticle probe capable of MRI-PA-Raman imaging.[107] Using a 532 nm laser they demonstrate a high photoacoustic efficiency of 2.75×10^{10} $cm^{-1}M^{-1}$ from a gold core shell particle coated in a Raman active dye and Gd^{3+} ions for MRI.

Furthermore, the use of a series of single molecule Raman-PA probes has been shown by Dinish *et al.*[58] Achieved by incorporating the NIR absorbance required for PA imaging into the inherent structure of a cyanine molecule used for Raman spectroscopy.

1.6.3 Magnetic resonance imaging (MRI)

MRI is an incredibly useful imaging technique that gives high quality imaging of inside the body using the fundamentals of nuclear magnetic resonance (NMR). High strength radiofrequency energy is used to excite and detect the relaxation of given atomic nuclei when situated inside an electromagnetic field.[108] This gives a high spatial resolution and infinite penetration depth which are highly advantageous for imaging the contrast in soft tissues. Hydrogen nuclei are the most observed, and are abundant in the water and fats of the soft tissues. MRI has therefore become a staple in the diagnosis of many different conditions and diseases; from various types of cancer tumour screening[109–111] to brain functionality, such as the atrophy in Alzheimer's disease[112] and strokes[113].

Exogenous contrast agents are typically used to alter the signal generation of the endogenous nuclei by decreasing the relaxation times. T_2 contrast agents decrease the T_2 relaxation times and give rise to a strong negative contrast in the image. It is the superparamagnetic properties of ultra-small iron oxide nanoparticles give rise to a strong T_2 spin-spin relaxation contrast,[114,115] whereas, in contrast, chelated gadolinium contrast agents proved a strong T_1 spin-lattice relaxation[116,117]. T_2 relaxation is typically a faster process than the corresponding T_1 relaxation.

T_2 relaxation is the time taken after excitation for the magnetic resonance signal to decay $1/e$, or 37%, of its original value. This leads to relationship between M_{xy},

the transverse component of the magnetization vector, and *t*, the time for which the decay occurs, as seen by the equations:[118]

$$M_{xy}(t) = M_{xy}(0)e^{\frac{-t}{T_2}} \tag{1.16}$$

$$r2 = \frac{1}{T_2 \cdot [C]} \tag{1.17}$$

Where *r2* ($mM^{-1}s^{-1}$) is the relaxivity and is the concentration, [C], dependant correlation to the inverse of T_2 relaxation times.

For examples, literature reports show the *r1* and *r2* contrasts of various iron oxide nanoparticles, each functionalised or synthesised by various routes, differs in values.[119] With the highest *r2* values seen in literature being within the order of >800 $mM^{-1}s^{-1}$ for Zn^{2+} doped magnetic nanoparticles.[120] In very recent developments, Wei *et al.* studied ultra-small iron oxide nanoparticles to enhance the T_1 contrast; making a Gd-free positive contrast agent, with very little chance of iron overload in the body.[121]

The combination of multiple nanoscale materials into one functional nanoparticle imaging probe has been challenging. Developments from Jin *et al.* have been able to synthesise an iron oxide – gold core – shell nanoconstruct with well-defined structural and functional properties. They show that separation of the iron oxide and gold layers with a dielectric polymer layer leads to uniform particles with good functionality in the NIR range. The combination of magnetic and optical properties has therefore enabled a new style of imaging modality in magnetomotive photoacoustic (mmPA) imaging.[122] These are critical

developments in the developmental use of multimodal imaging techniques involving PA and MRI.

1.6.4 Surface enhanced Raman scattering (SERS)

Raman scattering, discovered and published in the 1920's by physicist C. V. Raman, is the inelastic scattering of a photon caused by a molecule.[123] The incident photon interacts with the molecule, an energy transfer occurs, and a shift in the photon wavelength is seen.

SERS spectroscopy is a surface sensitive technique for the sensing of absorbed molecules on a metallic surface which enhances the molecules Raman spectra. Enhancement can be up to a factor of 10^{15} making SERS a highly sensitive spectroscopic technique able of the detection of minimal quantities of molecules and even single molecules.[124,125]

The true mechanism of SERS has yet to be fully understood though experimental research and two predominant theories are available. The electromagnetic theory states that excitation is caused by localised surface plasmons on the surface of the substrate. This can apply to most cases of SERS observed, whereas the chemical theory requires a chemical bond between the substrate and analyte to allow a surface charge transfer mechanism.

Most substrates make use of the high optical SPR effects of gold and silver nanostructures either as colloidal nanoparticle solutions, nanoparticles grafted to a silica (glass) surface, or plasma splutter deposition coatings.[126–129]

Being as sensitive as it is, SERS is widely used as a chemical sensor. Detection of proteins and antibodies in bioassays is common in industrial laboratories. Explosives detection is also important, as low amounts of explosive residue can be detected for concealed explosives in terrorism and in old landmines. As such, Dasary *et al.* have reported a highly selective cysteine modified gold nanoparticle capable of recognition of 2 picomolar (pM) levels of trinitrotoluene (TNT) in aqueous solution.[130]

There is currently great interest in developing highly sensitive and selective SERS substrates for chemical sensing. Research is also actively searching for reusable and more cost effective materials for SERS such as aluminium and paper sensors.[131–133]

1.7 THESIS OUTLINE

This thesis will report on the research undertaken in the synthesis of metallic nanoparticles – mostly iron oxide – and their functional applications as thermotherapy agents in magnetic hyperthermia and imaging probes in MSOT and MRI spectroscopies.

Chapter 2 starts with the synthesis of iron oxide nanoparticles though the common co-precipitation method for their use in magnetic hyperthermia. In an attempt to further functionalise the particles, gold was added to the synthetic procedure.

Chapter 3 will describe the start of a multimodal imaging probe based on an iron oxide core. This chapter will show the attempts to making iron oxide

nanoparticles SERS active through the functionalisation of the surface with the aforementioned gold. Furthermore, gold nanoparticles and nanostars were synthesised to show their potential SERS properties.

Finally, the development of a MSOT-MRI iron oxide nanoparticle probe is outlined in Chapter 4. This takes the synthesised iron oxide nanoparticles and the covalent attachment of PA dyes to its surface. With these probes *in-vivo* measurements of MSOT and MRI were obtained to demonstrate the effective nature of the synthesised nanoparticles.

This thesis is then completed with a compressive conclusion to the research and a proposal for the future direction of this work and any research related to this subject matter.

2 MAGNETIC HYPERTHERMIA

2.1 INTRODUCTION

Iron oxide nanoparticles have been known to exhibit significant magnetic heating properties when under the influence of an external magnetic field, as described in Chapter 1. Within this chapter, the synthesis of iron oxides with various stabilising ligands, were explored as to the effects of attempting to use gold as a capping agent to enhance functionality.

As is necessary for nanoparticles, stabilisation of the surface is required. For this, the proposal of a gold shell was a promising proposition. As seen commonly in literature, capping agents take multiple forms. From organic polymers,[18,134,135] inorganic coatings[136–138] and metallic shells. Of these, gold coatings on iron oxide nanoparticles have been seen of importance.[139–142] Importantly the addition of gold can facilitate the easy covalent binding of ligands and polymers to further enhance the nanoparticle usefulness. As is common in chemistry, and biological engineering, thiols have a high affinity to metallic gold. It is also proposed that a gold coating can be an effective way to limit the surface oxidation and overall degradation of the iron oxide nanoparticle. Due to the chemical stability and labile reactivity of gold to ambient conditions, a surface coating can protect the magnetic core. However to achieve a comprehensive surface coating on the iron

oxide surface can be difficult when dealing with such scales and surface potentials.[143] Still, even some addition of gold to the iron oxide may be desirable. This can present itself as partial encapsulation of a nanoparticle, a dumbbell particle, or as an intimately mixed nanocomposite material. The gold can then be employed, as mentioned, to improve bio-compatibility and functionality. Additionally, gold has a wide range of beneficial optical properties including SPR bands, SERS and PA imaging for optical imaging and chemical detection. Gold is also a key component in the cancer therapy PDT (photodynamic therapy). The combination of magnetic hyperthermia and PDT would then be a multimodal attack in the fight against cancer.

To focus on the therapeutic nature of gold – magnetite/maghemite nanoparticles, it is important to consider both materials. Great attention has been given to the heating phenomenon when a nanoparticle is placed within an electromagnetic field. For iron oxide this involves a rapidly alternating magnetic field (frequency, $f \approx 100$ kHz to 1.5 MHz) at high field strength (amplitude $H > 5$ kA/m) to achieve clinical hyperthermia wherein at 40-44^{o}C cell apoptosis occurs.[5] Pathogens and cancer cells are notably more susceptible to this heating, thus make more conventional therapies, i.e. chemo/radiotherapy, much more potent. As described in Section 1.6, this heat can be quantified by the specific absorption rate (SAR/ W/g_{FeOx}) which can then be related to the intrinsic loss parameter (ILP/ nHm^2/kg_{FeOx}). Typically, literature shows that a good quality iron oxide magnetic nanoparticle will demonstrate an ILP in the range of 1 - 3 nHm^2/kg_{FeOx}.[89,91]

In this chapter therefore a discussion and analysis of the effect on the magnetic heating properties of iron oxide-gold nanocomposite materials is achieved. Using

a novel method, a Turkevich reduction of $HAuCl_4$ was modified to add Au to the previously-synthesised citrate capped iron oxide nanoparticles.[45] It was noted that the gold did not form core-shell particles or a homogenous capping layer over the iron oxide core. However, gold nanoparticles were synthesised amongst the iron oxide nanoparticles and the size of the gold nanoparticles grew with positive correlation to the amount of $HAuCl_4$ added in the synthetic methodology. The iron oxide nanoparticles remained largely unchanged during this post production reaction. This lead to the remarkable discovery that the ILP of iron oxide increased three fold upon addition of chloroauric acid under optimum conditions.

2.2 MATERIALS & METHODS

2.2.1 Materials

All chemicals and were used as received and without further purification. Iron(III) chloride hexahydrate ($FeCl_3.6H_2O$) (99%), iron(II) chloride tetrahydrate ($FeCl_2.4H_2O$) (98%), and tetramethylammonium hydroxide (TMAOH) (99%, 25% w/w water) were purchased from Alfa Aesar. Ammonium hydroxide (NH_4OH) (25% in water w/w), citric acid (99%), tiopronin (99%), trisodium citrate dihydrate and chloroauric acid ($HAuCl_4$) were all purchased through Sigma Aldrich. All water used was distilled to 15 MΩ.

2.1.1 Synthesis of tiopronin-stabilised iron oxide nanoparticles

Fe_3O_4 nanoparticle co-precipitation requires a 2:1:1 molar ratio of Fe(III): Fe(II): surfactant. $FeCl_3.6H_2O$ (2.703 g, 10 mmol), $FeCl_2.4H_2O$ (0.995 g, 5 mmol) and tiopronin (0.816 g, 5 mmol) were added to degassed H_2O (20 mL) under N_2. The orange solution was heated to 70^oC and addition of TMAOH (21 mL) was added drop wise over 5 minutes, turning the solution black. The solution was allowed to cool to room temperature, washed by dialysis (cellulose membrane, M.W. 12 400, average flat width 76 mm) for 5 days, and collected with a permanent magnet. A black ferrofluid was recovered which was dried at -55^oC at reduced pressure yielding a fine black powder (~ 300 $mgmL^{-1}$).

2.1.2 Synthesis of citrate-stabilised iron oxide nanoparticles

This co-precipitation synthesis of Fe_3O_4 is a slightly adjusted method of the tiopronin Fe_3O_4 particles. Similarly; into degassed H_2O (80 mL) $FeCl_3.6H_2O$ (4.44 g, 16.4 mmol) and $FeCl_2.4H_2O$ (1.632 g, 8.2 mmol) were dissolved showing an orange solution. The temperature was then raised to 70^oC under N_2 and NH_4OH (20 mL) was added, turning the solution immediately black, and held for 30 minutes. Citric acid (4 mL, 0.5 g/mL) was added and the temperature was raised to 90^oC under reflux for 60 minutes. The black solution was cooled to room temperature, washed with H_2O and collected *via* a permanent magnet producing a fine black powder (~ 250 $mgmL^{-1}$). To obtain these concentrations, the suspension was freeze dried under reduced pressure to produce a magnetic black powder which was then re-dispersed in H_2O (50 $mgmL^{-1}$) with the aid of ultrasonication.

2.1.3 Hydrothermal synthesis of oleate-stabilised iron oxide nanoparticles

To contrast the co-precipitation synthesis mainly used in the this thesis, attempts at creating organic soluble iron oxide nanoparticles through the common hydrothermal synthesis pioneered by Park *et al.* were made. Briefly, $FeCl_3.6H_2O$ (2.16 g, 8 mmol) and sodium oleate (7.3 g, ….. mmol) were dissolved in a mixture of ethanol (16 mL), hexane (28 mL) and water (12 mL) giving a deep orange solution. This was heated to reflux (70^oC) for 4 hours to form an iron oleate intermediate. The products were washed and separated with water (3 x 30 mL), and the organic solvents were evaporated under reduced pressure leaving a red waxy solid.

For the formation of the nanoparticles from this product, the iron oleate (7.2 g) and oleic acid (1.14 g) were dissolved in 1-ocatadecene (40 g (at room temperature)). This mixture was then heated to reflux, at 320^oC, at a constant 3^oC/min at which the solution turned from red to brown to black as the temperature rose. Excess ethanol was then added to precipitate out the nanoparticles, which yielded a black oily product. Where further attempts to dry the product under reduced pressure were not successful.

2.1.4 Synthesis of FeO@Au nanocomposites

Using the pre-synthesised Fe_3O_4 nanoparticles, it was possible to use the citrate binding of the SPIONs as a reducing agent for $HAuCl_4$ akin to the Turkevich synthesis, with some slight modifications. Firstly, $HAuCl_4$ (20 mL) of varying concentration (0.1 - 5.0 mM) was heated to boiling and the previously synthesised

citrate-stabilised Fe_3O_4 (10 mL, 5 $mgmL^{-1}$) was added instantaneously. With continued heating and mixing for 10 minutes, the solution turned from yellow to black to deep red/brown. The solution was then cooled to room temperature, washed with H_2O and collected with a permanent magnet. The solution was then dried as before at -55^oC and under reduced pressure producing red/brown powders (2-3 $mgmL^{-1}$).

2.1.5 Synthesis of gold nanoparticles

Gold nanoparticles were synthesised *via* the Turkevich synthesis so as to be comparable to the iron oxide – gold nanocomposites. For this synthesis, a solution of trisodium citrate dihydrate (1.6 mL, 0.5%) was added to a solution of $HAuCl_4$ (20 mL, 0.18 mM) at 65 ^oC. Upon a colour change from yellow to red, the mixture was then boiled at 100 ^oC for 20 minutes.

2.1.6 Particle size and morphology

Particle size and morphology was performed using a combination of transmission electron microscopy (TEM), dynamic light scattering (DLS), and both UV-vis and infra-red (IR) spectroscopy. TEM was performed using a JEOL 1200EX MKII TEM microscope using an accelerating voltage of 120 kV. TEM samples were prepared by aqueous liquid drop of as-synthesised ferrofluid onto perforated carbon grids. DLS was performed on the aqueous ferrofluid with a Malvern Zetasizer Nano, using 1 mL samples in a 4.5 mL plastic cuvette. Ultra-violet

spectra were obtained on a Lambda 25 UV-Vis spectrometer from wavelengths 300 – 1000 nm with a step size of 0.5 nm. The analyte was as-synthesised in an aqueous medium and recorded in a 4.5 mL cuvette. Infra-red spectroscopy was performed on a Perkin Elmer Spectrum 100 FTIR/ATR Spectrometer in the wavenumber range 600 – 4500 cm^{-1}.

2.1.7 Mössbauer spectroscopy

The chemical composition was assessed using room temperature ^{57}Fe Mössbauer spectroscopy, with the assistance from Dr Lara Bogart. Freeze dried samples were mixed with sucrose using a pestle and mortar and gently packed into a 22 mm diameter, ca. 2 mm thick disk-shaped sample holder. Transmission Mössbauer spectroscopy was performed at room temperature using a ^{57}Co foil source embedded in a rhodium matrix with an initial activity of 25 mCi. The source was driven over a range of velocities from -15 mm/s to +15 mm/s via a SeeCo W302 spectrometer using a constant-acceleration drive with triangular reference signal. Data were accumulated in a SeeCo W202 detector with 1024 channels (unfolded) that was calibrated against the Mössbauer spectrum of a standard α-Fe foil at room temperature. All spectra were fitted using the Recoil data analysis programme.[35]

2.1.8 X-ray spectroscopy

X-ray photoelectron spectroscopy (XPS) was obtained with a K-Alpha X-ray Photoelectron Spectrometer system using monochromatic aluminium K-alpha X-rays (0.83386nm, 1.4867 KeV). Energy-dispersive X-ray (EDX) spectra were obtained on a Philips XL30ESEM microscope. The crystal structure was investigated using powder X-ray diffraction (PXRD) which was achieved on a STOE STADI P transmission diffractometer using Mo $K_{\alpha 1}$ radiation (17.48 keV, $\lambda K_{\alpha 1}$ = 0.7093 Å) at 50 kV and 30 mA. The 2θ scan was performed between 2.000^{o} and 50.015^{o} at steps of 0.495^{o} with a scan duration of 10 s/step.

2.1.9 Magnetic heating

The intrinsic loss parameters (ILPs) of the samples were measured using a Magnetic Alternating Current Hyperthermia (MACH) system built by Resonant Circuits Limited (London). This instrument comprised a purpose-built 6-turn copper solenoid operating at 967 kHz that produced a sinusoidally varying magnetic field of peak amplitude 6.6 kAm^{-1}. Thermal heating curves were recorded as a function of time on application of the radio frequency (RF) field. Samples comprising 500 μL of fluid were placed into glass vials in the centre of the RF coil, and temperature variations were recorded by averaging the data from two Luxtron FOT fluoroptic probe thermometers (LumaSense Technologies, USA) immersed within the fluid.

2.3 RESULTS & DISCUSSION

2.3.1 Synthesis

2.3.1.1 Initial Reactions

Initial reactions for the repeatability and suitability of the iron oxide synthesis were carried out, with all iron oxide nanoparticles being synthesised *via* the co-precipitation method. This method has been widely studies, with this being a continuation of previous literature[9] from the Parkin lab. Here ferric and ferrous chloride salts were dissolved and heated to 70^{o}C and reduced with ammonia alongside a stabilising ligand; citric acid or tiopronin.

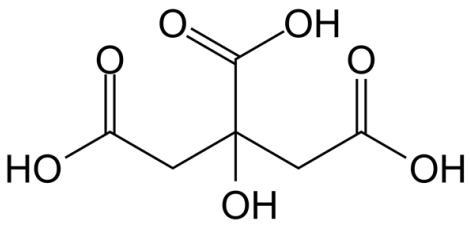

Citric acid

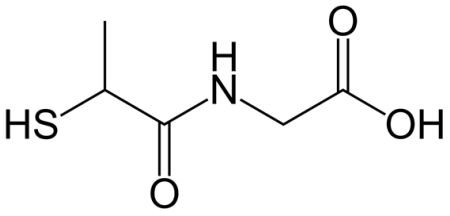

Tiopronin

Figure 2.1. Chemical structures of the stabilising ligands citric acid and tiopronin. Note that both molecules contain a carboxyl group, which is significant for the bidentate binding of the binding of the ligand to the iron oxide surface.

These products were purified with water and isolated to black powders through freeze drying and from here classified as FeOx-tiopronin and FeOx-citrate respectively.

Furthermore, it was through varying the reaction conditions, especially temperature, which yielded suitably repeatable nanoparticles. The synthetic temperature was varied from room temperature (25^{o}C) through to 90^{o}C.

2.3.1.2 Citrate-capped iron oxide synthesis

After repeated synthesis of both citrate-capped and tiopronin-capped iron oxide nanoparticles, FeOx-citrate was repeatedly synthesised in the aforementioned method before further functionalisation with gold. The iron oxide nanoparticles were added to varying concentrations of boiling chloroauric acid and heated until the colour change ceased. Again these products were purified with water and dried *via* freeze drying, at reduced pressure and -55^{o}C, and classified as FeOx-Au_x where x = Au concentration in mM. All products were then readily dispersible in water and formed strong ferrofluids.

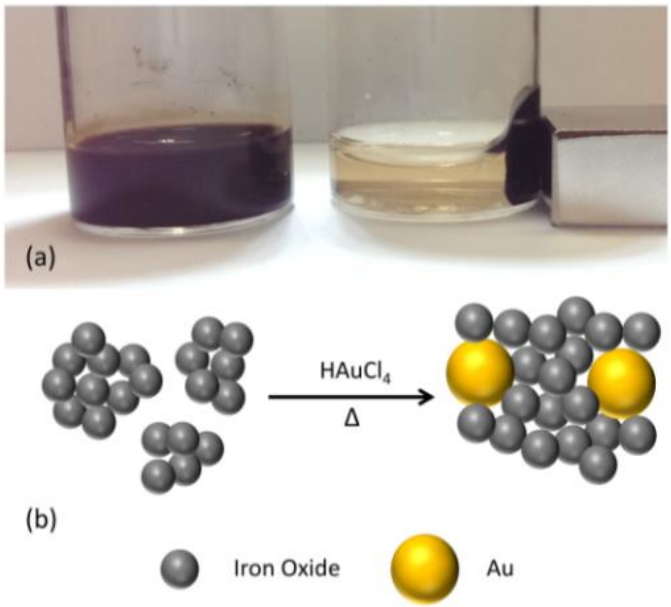

Figure 2.2. (a) Photograph showing the citric acid stabilised ferrofluid FeOx-citrate with and without the influence of an external magnetic field. In the absence of the magnetic field the ferrofluid forms a stable suspension in water. (b) Graphic showing the morphology of the FeOx-Au_x nanoclusters formed from hydrogen tetrachloroaurate reduction by citrate capped iron oxide nanoparticles.

2.3.2 Structural characterisation of iron oxide nanoparticles

2.3.2.1 Size and morphology

Figure 2.2 shows the tunnelling electron microscopy of FeOx-citrate. The particles in the image can be seen to be roughly spherical in shape with the accompanying histogram showing a mean physical diameter of 8.0 nm with a standard deviation of 1.8 nm (147 particles).

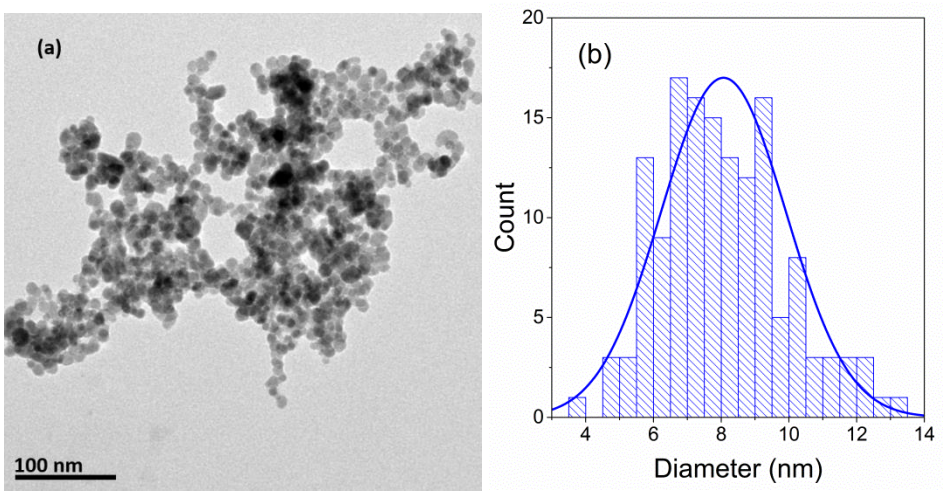

Figure 2.3. (a) Transmission electron micrograph of the as-synthesised citrate-coated iron oxide nanoparticles and (b) the TEM-derived size distribution histogram for the inorganic cores.

The particles appear to be synonymous with co-precipitation reaction schemes. There are characteristic size and shape particles, with some degree of polydispersity. There is also some aggregation of the nanoparticles when in solution. It also helps to show that each particle will, in all probability, possess only one magnetic domain which will occur when said particles are < 20 nm in diameter.

The same can be seen in the dynamic light scattering (DLS) analysis performed on the FeOx-citrate nanoparticles. Firstly, the hydrodynamic diameter, φ_H, is given as 252 nm when measured by intensity and a polydispersity index (PDI) of 0.27. The φ_H is considerably larger than the 8.0 nm seen via TEM analysis and can be attributed to the aggregation of the individual nanoparticles into larger clusters.

2.3.2.2 X-ray spectroscopy

Powdered X-ray diffraction (PXRD) was used to identify the phases and crystallinity of the synthesised nanoparticles. This confirmed that FeOx-tiopronin and FeOx-citrate featured iron oxide in its cubic structure (Figure 2.4), showing the main characteristic peaks of (220), (311), (400), (511) and (440) at 13.76°, 16.12°, 19.49°, 25.39° and 27.73° 2θ respectively. As these peaks are synonymous with both Fe_3O_4 and γ-Fe_2O_3 it cannot confirm which state of state of iron oxide is present, especially in the nanoparticle state.[144]

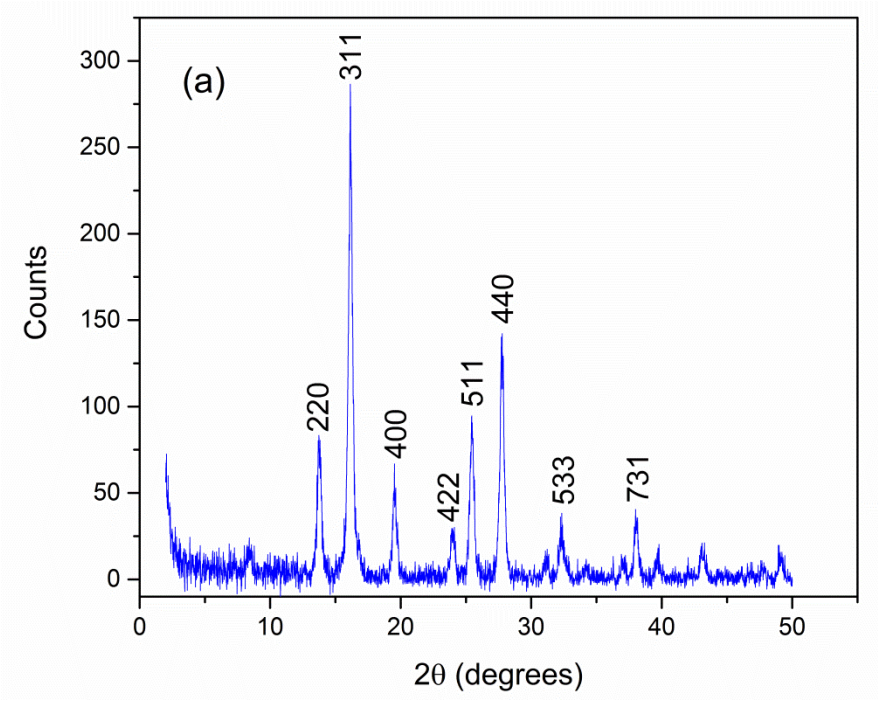

Figure 2.4. Mo-K_α θ-2θ powder diffraction pattern of FeOx-citrate nanoparticles, indexed against its cubic lattice miller indices. Note the high crystallinity due to the high signal to noise ratio.

High signal to noise ratio shows that the particulates are of a fine texture resulting in the clean and sharp diffraction pattern. From the Scherrer equation, the crystallite size was determined.[145] This was calculated as 17 nm using the FWHM of the (311) plane at 16.1^{o} 2θ. The PXRD spectra was achieved for both FeOx-citrate and FeOx-tiopronin, of which both had the same diffraction pattern. FeOx-citrate however was shown with lower intensity, suggesting a lower degree of crystallinity. This is reinforced by the Scherrer equation analysis showing a crystallite size of 9 nm.

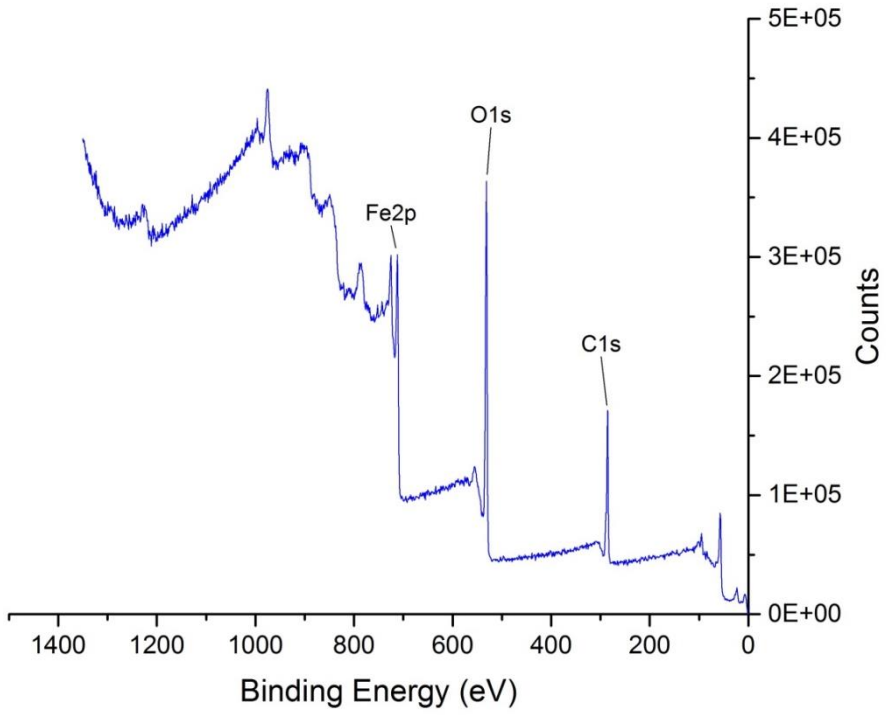

Figure 2.5. XPS scattering pattern of FeOx-citrate nanoparticles showing the presence and binding energies of Fe, O and C environments within the nanoparticles.

Preliminary X-ray photoelectron spectroscopy (XPS) data has been utilised to establish the elemental components and their environments within the nanoparticles.

As seen in Figure 2.5 there are prominent scattering peaks for the carbon 1s electrons at 285 eV, oxygen 1s electrons at 530 eV and iron 2p electrons at 710 eV. These are all expected to be present within the iron oxide nanoparticles. The Fe2p is exclusively from the nanoparticles, whereas the O1s electrons are present in both the nanoparticles and the stabilising ligands. Here FeOx-citrate is analysed, with the citrate ligands containing a high proportion of oxygen atoms. The citrate ligand also gives rise to the C1s electrons. This has then shown that the iron oxide nanoparticles including ligands, contains an atomic % of 15% iron from the Fe2p binding energy.

2.3.2.3 Mössbauer spectroscopy

Room temperature Mössbauer spectroscopy (Figure 2.6) of the FeOx-citrate as-prepared material shows the distinguishing magnetic hyperfine splitting of the magnetite/maghemite series of iron oxides. This is shown as a distinctive six line absorption pattern. The best fit to the spectrum was obtained using Voigtian line profiles, following the quasi-phenomenological model recently described for fitting the Mössbauer spectra of Fe_3O_4/γ-Fe_2O_3 mixtures or solid solutions.[146] Voigtian line-shapes are used to represent a Gaussian distribution of hyperfine fields. The splitting of these fields can arise from physiological reasons, such as; a

range of morphologies, crystallographic impurities, or the presence of collective excitations.[147]

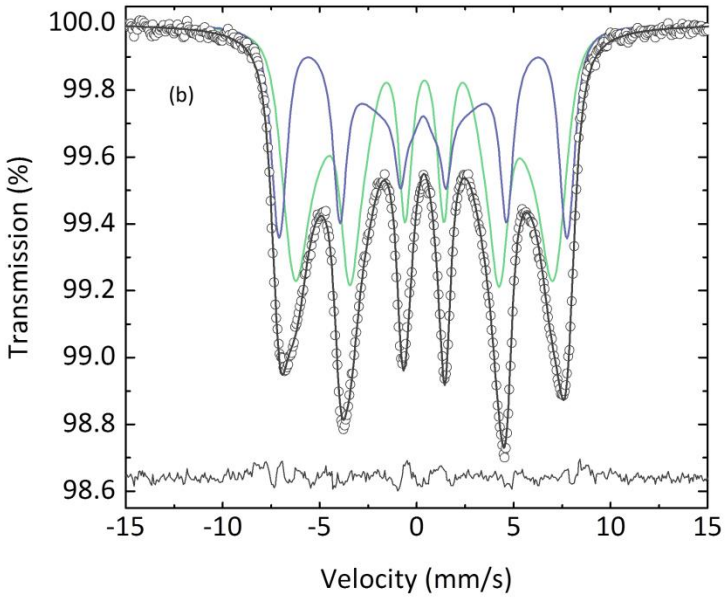

Figure 2.6. Room temperature Mössbauer spectrum of the as-prepared citrate-coated iron oxide nanoparticles (FeOx-citrate) sample. The best fit to the observed spectrum was obtained using two Voigtian sextets, each comprising two sub-component spectra. The residual between the observed data and the model is indicated by the lower trace

The cumulative mean isomer shift or centre of gravity of the spectrum (i.e. the average over all the contributing subcomponent spectra) was determined to be $\bar{\delta}_{RT}$ = 0.37 ± 0.01 mm/s, which lies between that of pure maghemite ($\bar{\delta}_{RT}$ = 0.32 mm/s) and pure magnetite ($\bar{\delta}_{RT}$ = 0.53 mm/s). Given that it is more likely that the material is a mixture of phases than for it to be a solid solution – the latter being

more characteristic of bulk systems, while the former is known to be a characteristic of fine particle magnetite/maghemite systems[147] – we can use the $\bar{\delta}_{RT}$ measurement to estimate the composition of the mixture.

Following an established procedure,[147] $\bar{\delta}_{RT}$ = 0.37 ± 0.01 mm/s equates to a magnetite content of 23% ± 5% w/w – meaning that 23 ± 5 wt.% of the as-prepared iron oxide is in the form of magnetite, and the remaining 77 ± 5 wt.% is in the form of maghemite.

2.3.3 Structural characterisation of iron oxide – gold nanocomposites

Upon the addition of $HAuCl_4$ into the synthetic procedure, there were significant changes detected in several aspects of the material. The post-production of iron oxide nanoparticles into iron oxide – gold nanocomposites was achieved through a Turkevich style gold reduction. Briefly, to boiling concentrations of $HAuCl_4$ the as-synthesised citrate-coated iron oxide (FeOx-citrate) was added, where a colour change of black to burgundy was noted. This colour change was the first indication that a gold nanostructure had formed, with gold nanoparticles having a very distinctive and characteristic red colour. A series of gold-containing samples was synthesised, and from here-on will be classed as FeOx-Au_x where x = [$HAuCl_4$] used in synthesis.

2.3.3.1 Size and morphology

Electron microscopy was used to study the morphological changes seen with the FeOx-Au_x series of nanomaterials as a function of gold addition. TEM images seen in Figure 2.7 show these changes for a range of $HAuCl_4$ concentrations and the corresponding histograms are in Figure 2.8.

Most notably about the microscopy is that the size and shape of the iron oxide nanoparticles has remained largely unchanged. They appear as mostly spherical particles, with a diameter of 8-10 nm. This is as expected and can be used to show that the iron oxide is merely a carrier of the reducing agent in the form of citric acid. However, it can be clearly seen that the size of the Au nanoparticles shows consistent growth over the series. Larger and increasingly polydisperse collections of particles appear as the $HAuCl_4$ concentration increases. Interestingly too, the iron oxide appears to be aggregating around the lager Au nanoparticles.

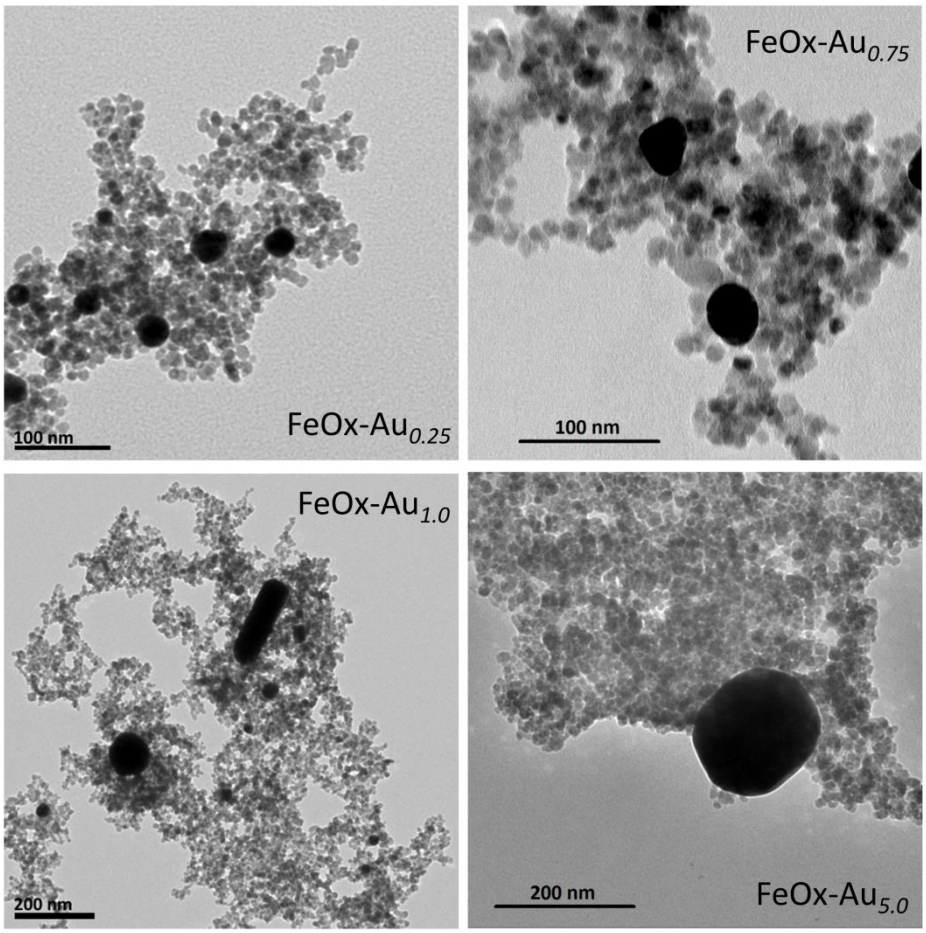

Figure 2.7. Representative TEM images of a selection of FeO-Au_x iron oxide-gold nanocomposites, showing that the Au nanoparticles increase in size as the molar concentration increases, and that the iron oxide nanoparticles form aggregates surrounding the gold nanoparticles.

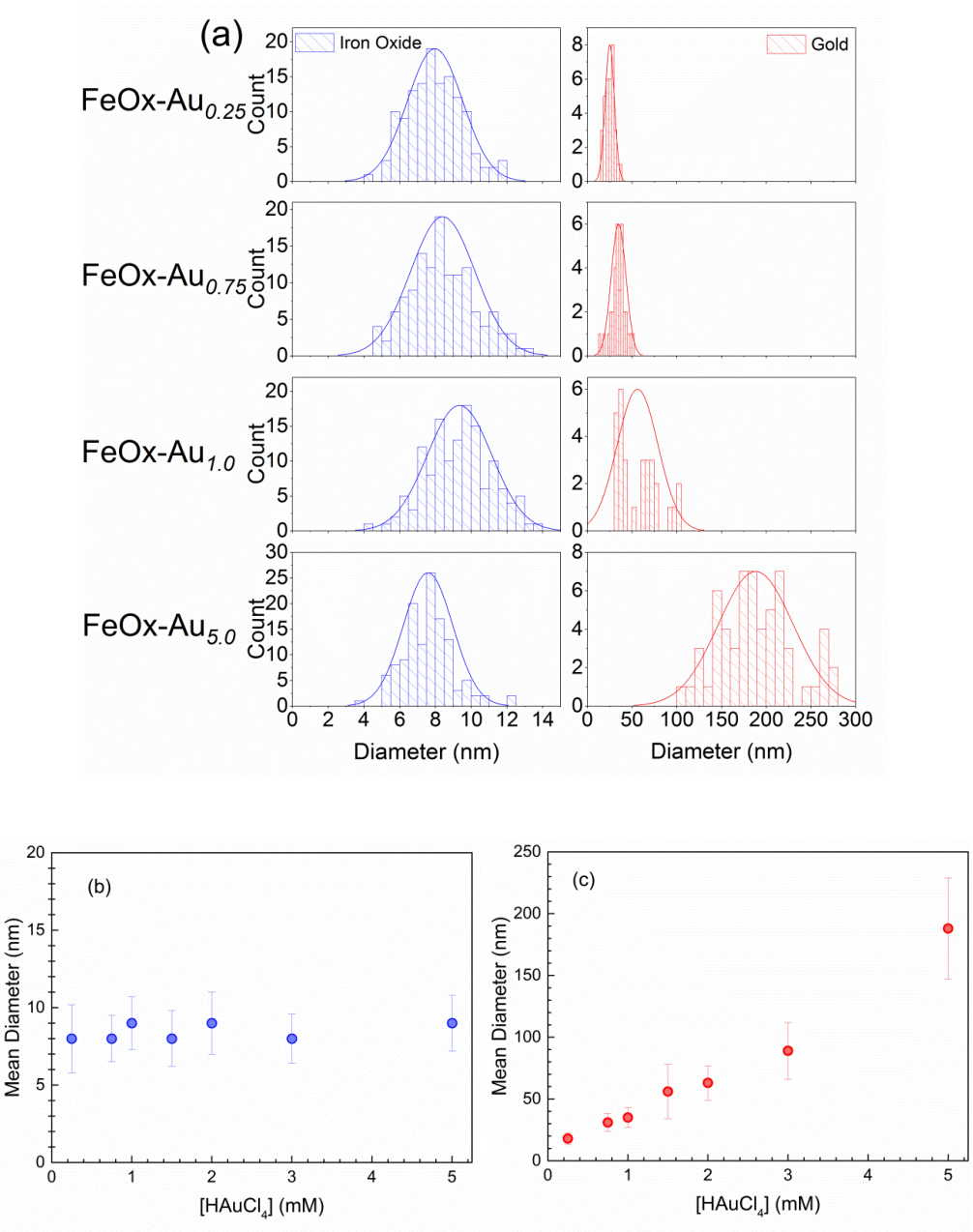

Figure 2.8. (a) Particle size distribution histograms derived from TEM data such as that shown in Figure 2.7 for a selection of FeOx-Au_x iron oxide-gold nanocomposites. (b) Means and standard deviations of the iron oxide and (c) the gold particles as a function of the $HAuCl_4$ concentration used during synthesis. Note that both the mean size and the polydispersity of the gold nanoparticles changes significantly over the series, while the iron oxide nanoparticles remain largely unaltered.

Furthermore, this can be confirmed with DLS data of the gold containing samples, which indicates that the particles were agglomerated *in situ*. Z-average hydrodynamic diameters, φ_H, of order 270 nm in FeOx-$Au_{0.75}$ and 960 nm in FeOx-$Au_{5.0}$, both with PDI's of order 0.3.

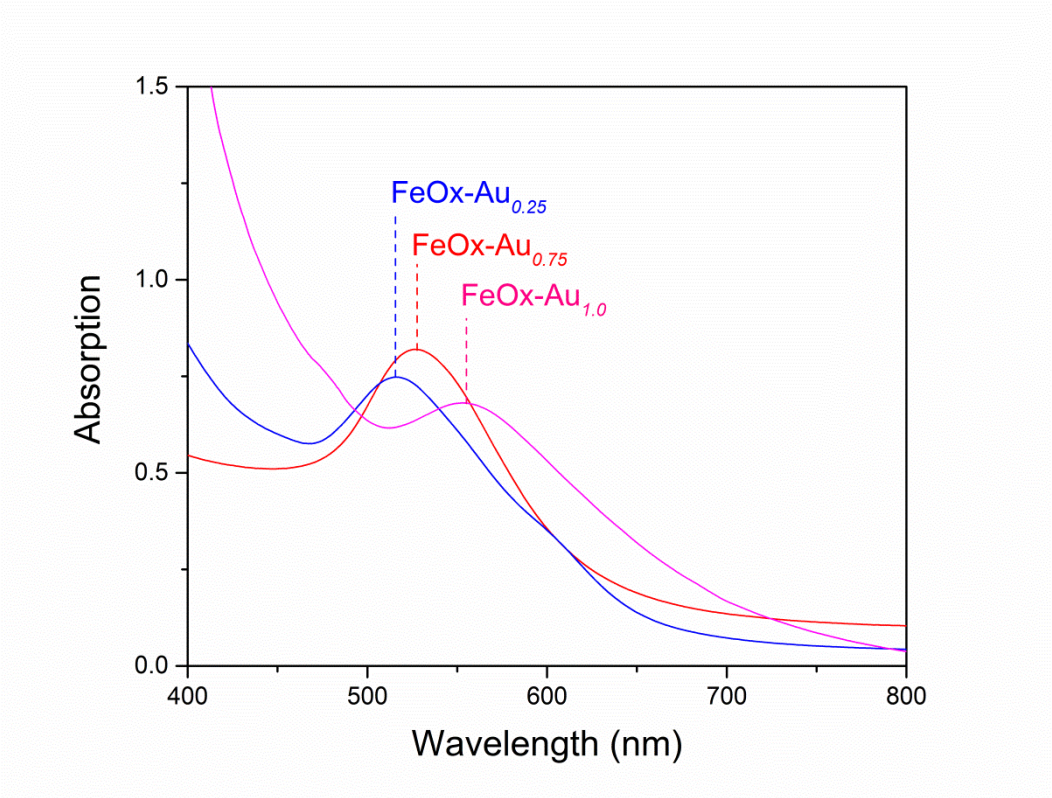

Figure 2.9. UV-vis spectra of FeOx-Au_x samples with [Au] concentration x = 0.25, 0.75 and 1.0 mM, showing the red shift in the gold absorption peak as the Au concentration increased.

UV absorption profiles of FeOx-Au_x also supported this growth of Au nanoparticle size. As seen in Figure 2.9, the surface plasmon resonance (SPR) absorption band of gold increases in wavelength as the concentration of $HAuCl_4$ increases. Depending on the size of the nanoparticles the wavelength at which

gold absorbs radiation varies with larger particles red-shifting the wavelength. Gold typically absorbs light in the range of 520-550 nm. Absorption here occurs from 516 nm (0.25 mM), to 526 nm (0.75 mM), and 556 nm (1.0 mM) for varying [Au]. Gold nanoparticles, of diameter 4 nm are shown to have an absorption at aproximately λ = 520 nm[148,149] which is similar here to the smallest gold nanoparticles at 0.25 mM [$HAuCl_4$]. As the gold nanoparticles subsequently increase in size, so too does the SPR band red-shift to longer wavelengths.

2.3.3.2 X-ray spectroscopy

PXRD was then obtained for FeOx-Au_x particles, using the same parameters. As is shown in Figure 2.10a), the crystal structure of gold is present with the (111), (200), (220) and (311) planes at 17.36^o, 20.02^o, 28.48^o and 33.55^o 2θ respectively. As well, there are the predominant peaks from the FeOx-citrate diffraction pattern therefore clarifying that the nanocomposites have been formed. There is a lower signal to noise ratio present compared to FeOx-citrate detailing that FeOx-Au_x are coarser in morphology. Gold is known to grow unevenly when forming nanoparticles and coatings, which could cause this courser texture. PXRD also shows that there is no structural change between the different nanocomposites for either the (311) iron oxide peak or the (111) gold peak (Figure 2.10b) with both exhibiting the same diffraction peaks at different gold concentrations.

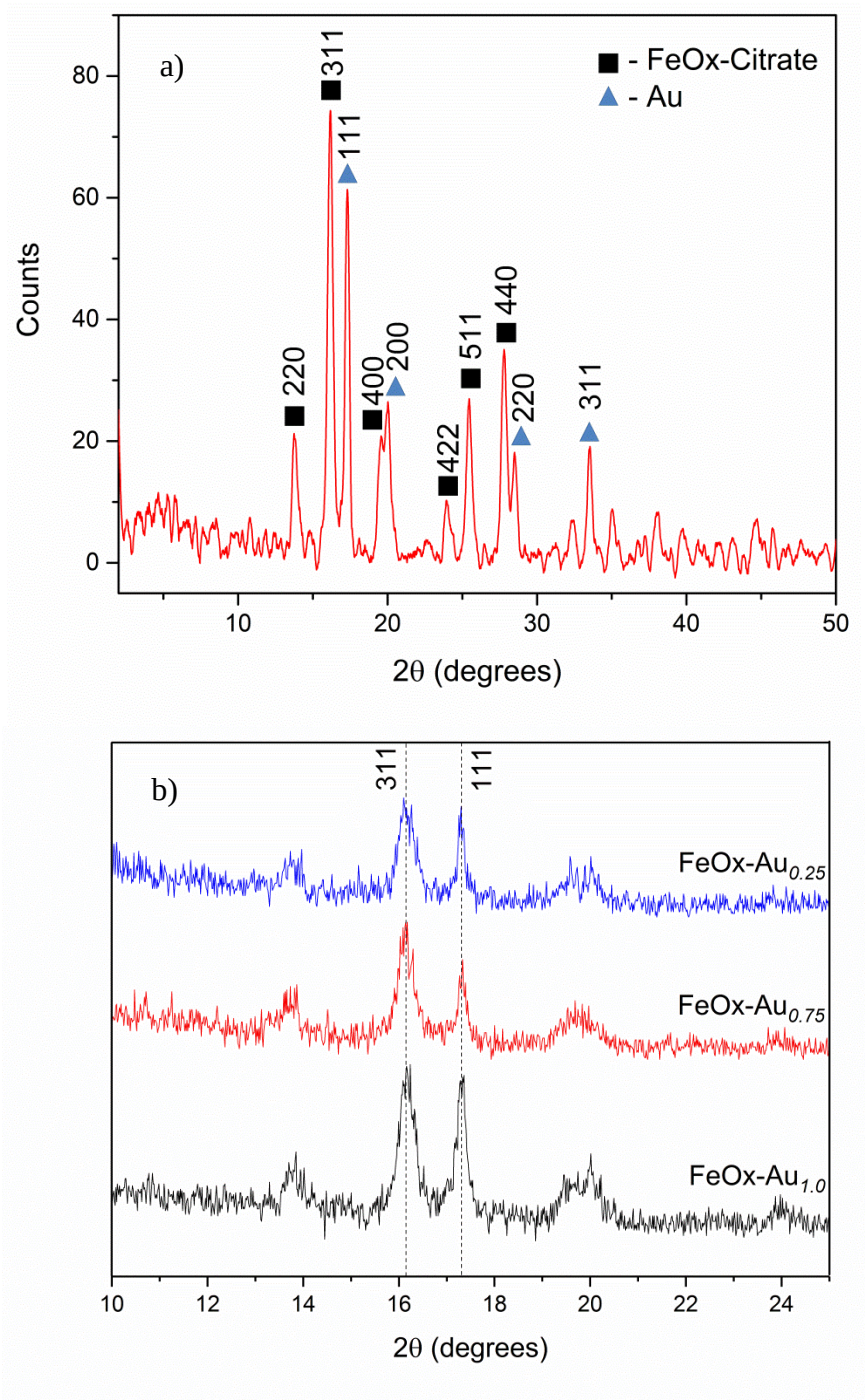

Figure 2.10. Mo-K_α θ-2θ powder diffraction patterns of FeOx-Au_x nanocomposites showing (a) the FeOx and Au reflections in the FeOx-$Au_{0.75}$ sample; and (b) the coincidence of the (311) iron oxide and (111) gold diffraction peak positions across the FeOx-Au_x series.

XPS was then used to detect the presence and atomic % of gold within the FeOx-Au_x nanoparticles. Figure 2.11 shows the presence of gold in the nanocomposites with Au4f7 and Au4f5 having a binding energy of 84.3 and 88.1 eV respectively. This represented an atomic % of 1% gold.

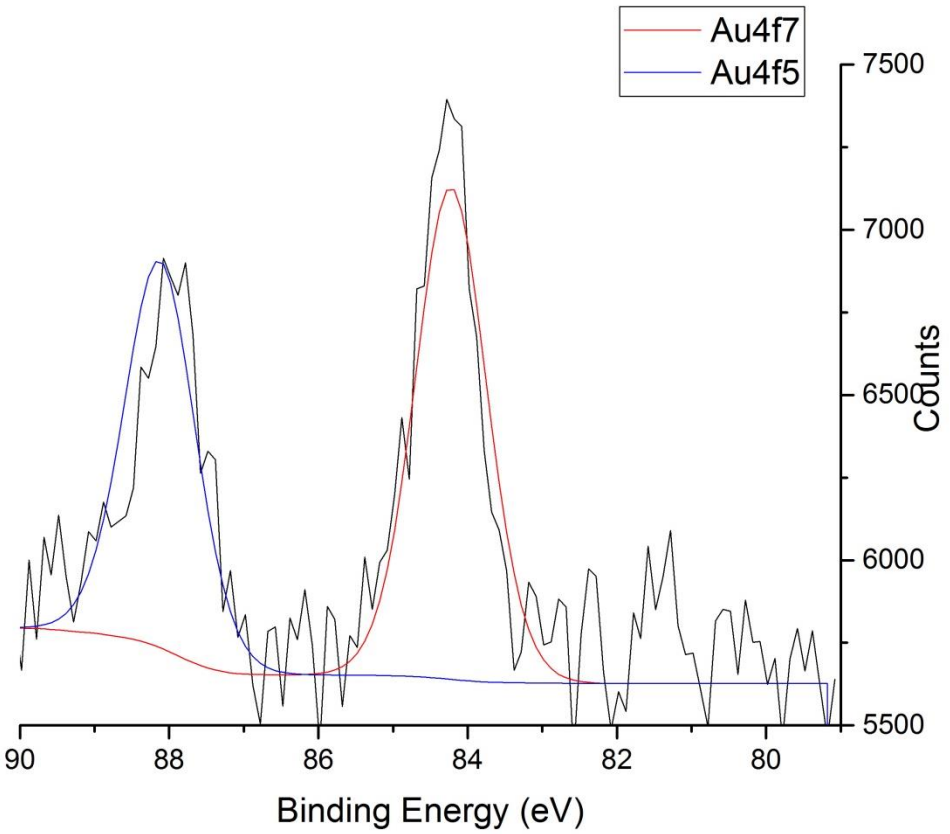

Figure 2.11: XPS of the Au specific binding energy region (between 80-90 eV) showing the presence of Au electrons showing the Lorentzian fitting for the Au 4f7 and 4f5 orbital electrons.

A depth profile of the nanocomposite was then analysed to get some insight into the morphology (Figure 2.12). The depth profile showed there is little to no change in the form of the scattering of the gold peaks. Thus, this is indicative of the formation of iron oxide – gold nanoparticle clustering over iron oxide – gold core-shell nanospheres. This is depicted in the scheme which shows the possible formations of iron oxide – gold nanocomposites.

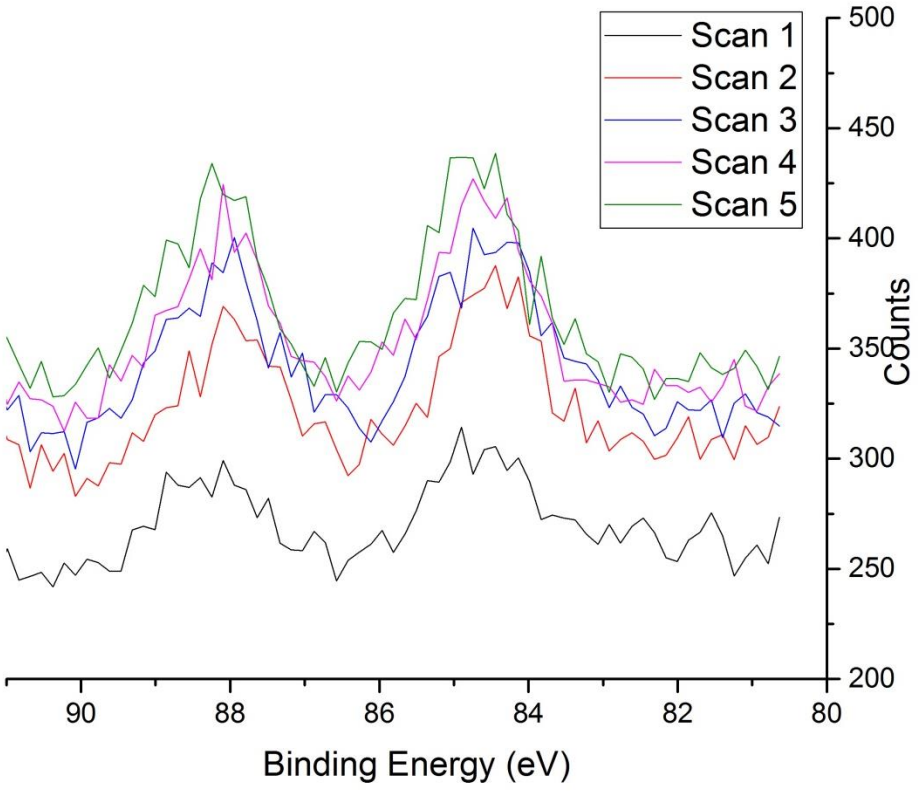

Figure 2.12: XPS depth profile scattering of Au particles within the iron oxide - gold nanocomposite FeOx-$Au_{0.75}$. Note that there is no loss off peak with each subsequent scan determining that gold is present throughout the whole sample.

2.3.3.3 Mössbauer spectroscopy

^{57}Fe Mössbauer spectroscopy was recorded for the series of gold containing iron oxide nanomaterials, FeOx-Au$_x$. This is shown in Figure 2.13, and it can be noted that the spectra vary considerably over the series. This is more clearly seen in Figure 2.13.b) which shows the difference spectra between the normalised FeOx-citrate (x = 0) and each given [Au] concentration ($x \geq 0$). At lower concentrations of gold and as the concentration increases from x = 0.1 – 0.75 mM, the spectra become broader in the central region, but the innermost lines still remain, whilst the outermost lines lose intensity. This is corresponding to a broad positive singlet peak superimposed over the original sextet at low [Au] ($x \leq 0.75$ mM).

In contrast, as the gold concentration increases further ($x \geq 1.0$ mM) there is a recovery of the original (FeOx-citrate) sextet line shape, becoming a negative component with sharp peaks. The broad singlet that grew in the early samples, has all but disappeared when x = 5.0.

As previous, for a more detailed analysis, fitting of the Mössbauer spectra was achieved with quasi-phenomenological model based on Voigt profiles (Figure 2.14.a)).[146] The same two sextet fittings were used as were used with the FeOx-citrate spectrum (Figure 2.6) as well as a further sextet, and the other being best described as a broad quadrupole split doublet. The fitted parameters confirm the change in behaviour of the nanomaterial over the gold concentration range (x = 0 to 5.0 mM). This is most notably in the area and splitting of the additional sextet component (Figure 2.14.b))

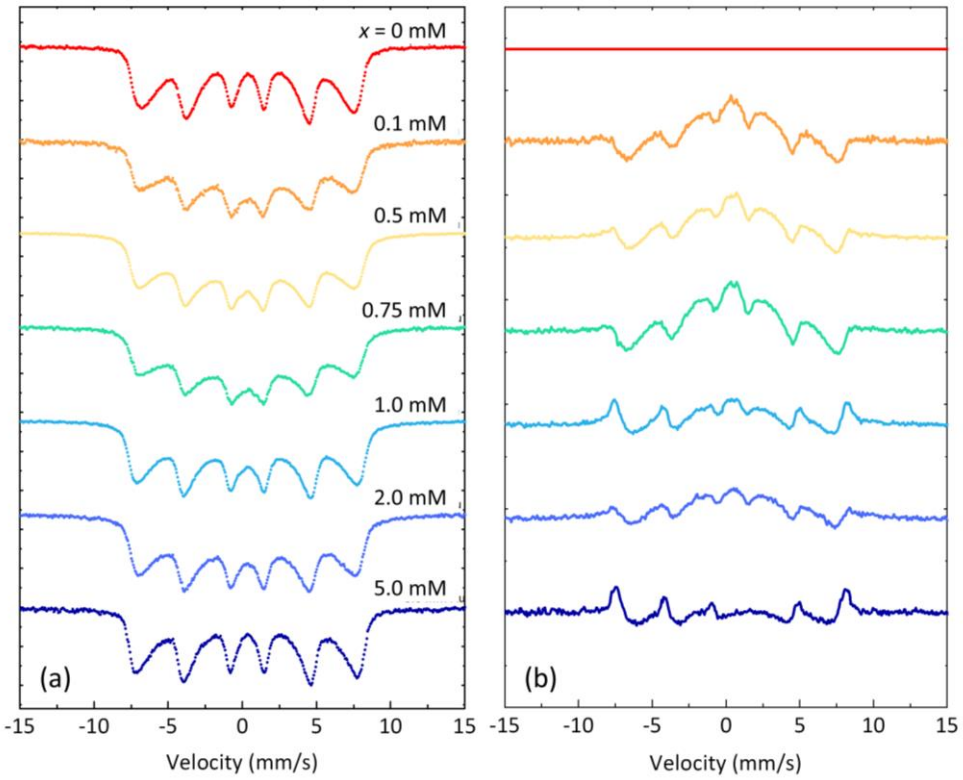

Figure 2.13. (a) Mössbauer spectra measured at room temperature for increasing amounts of gold in the FeOx-Au$_x$ samples, from x = 0 (the iron oxide only sample, FeOx-citrate) to x = 5.0 mM. (b) Mössbauer 'difference spectra' obtained by subtracting the FeOx-citrate spectrum from the FeOx-Au$_x$ spectra. These spectra provide a model-independent visual indication of how the Au-containing x > 0 spectra differ from that of the precursor FeOx.

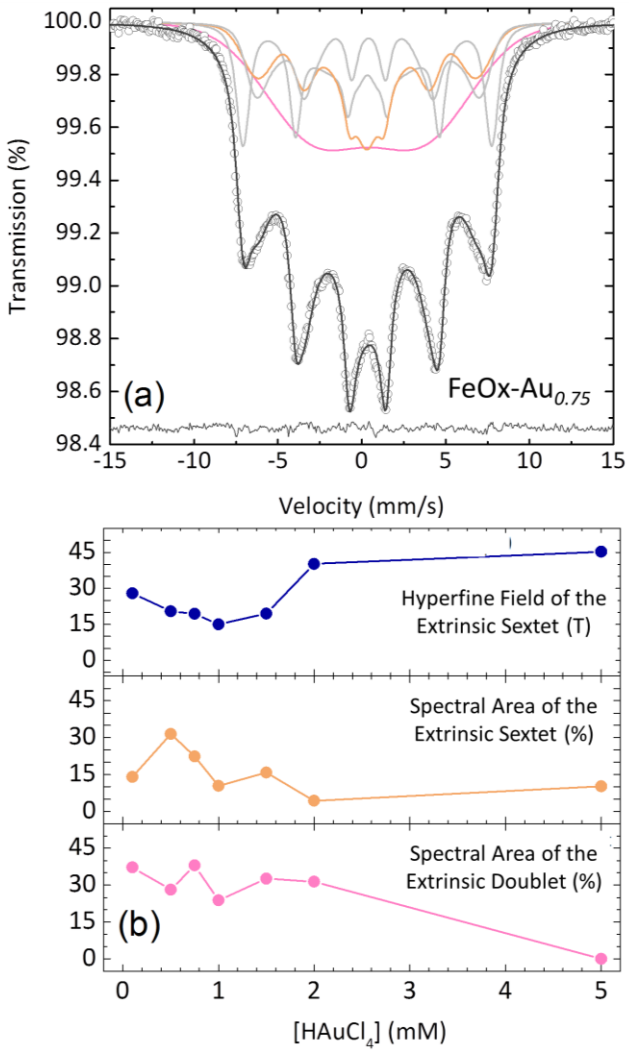

Figure 2.14. (a) Representative fit to the Mössbauer spectrum of sample FeOx-$Au_{0.75}$ using a quasi-phenomenological model. The constrained subcomponents of the initial FeOx-citrate spectrum are shown in grey, with additional ('extrinsic') subcomponents highlighted in orange (sextet) and pink (doublet). (b) Variation of some of the fitted Mössbauer parameters as a function of the $HAuCl_4$ concentration *x*: the percentage spectral areas of the extrinsic doublet and sextet components, and the mean hyperfine field (H_{hf}, in Tesla) of the extrinsic sextet component.

Although difficult to be decisive, there are several factors that could be attributed to this change in Mössbauer spectroscopy. It is clear to see that there has in fact been a change over the FeOx-Au_x series, even from the lowest [Au] concentration sample FeOx-$Au_{0.1}$. This could likely be due to the additional synthetic methods needed for the formation of the iron oxide – gold nanocomposite materials. Additional heating and processing is required for all samples, and this could be in an indication of further oxidation of iron oxide, from magnetite to maghemite, after primary synthesis. The mean isomer shift of the samples trended towards a slightly lower value of $\bar{\delta}_{RT}$ = 0.36 ± 0.01 mm/s across the series, which lends some weight to this hypothesis. This could also be showing a change in the properties of both iron oxide and gold at the interface between FeOx and Au phases. The presence of the doublet component is hence showing a less magnetic environment.

2.3.4 Magnetic hyperthermia

The fundamental application for the iron oxide nanoparticles in this study was primarily hyperthermia generation. This was analysed by using a 6 turn RF (Resonant Frequency) coil [resonant circuits ltd][150] to determine the heating potential including both the specific absorption rate (SAR) and intrinsic loss power (ILP)[90] of the iron oxide and the iron oxide – gold nanostructures.

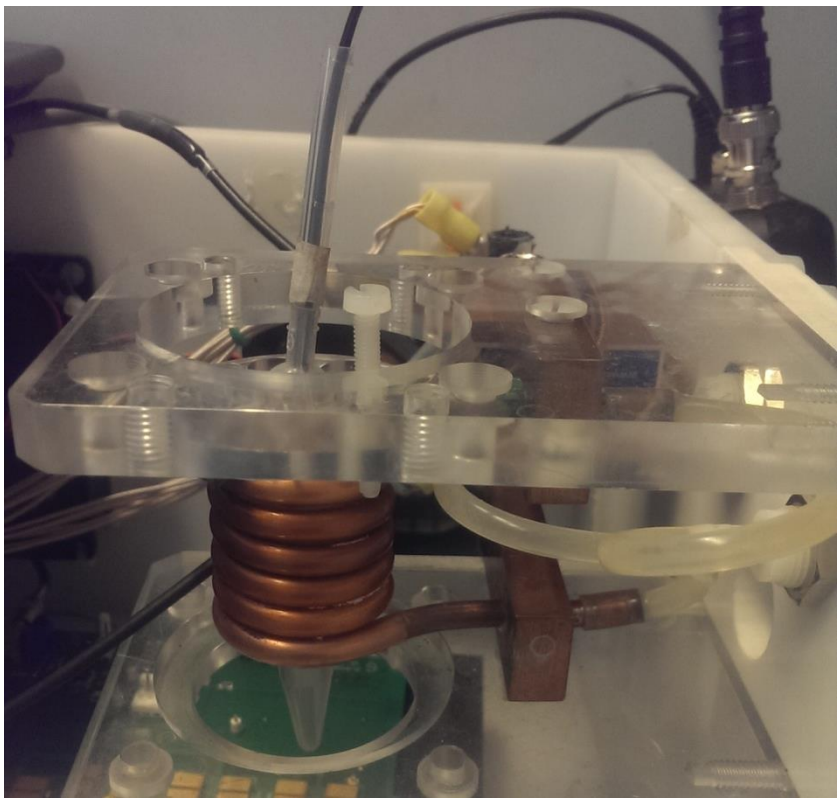

Figure 2.15. Photograph showing the 6-turn radio frequency induction coil that was used to generate the alternating magnetic field which caused heating *via* magnetic hyperthermia. The sample sits inside the centre of the coil to give a uniform field strength, with an optical temperature probe located in the sample. [resonant circuits ltd][150]

2.3.4.1 Iron oxide nanoparticles

Of the two iron oxide nanoparticle samples, it has been shown in Figure 2.16 and Table 2.1 that the citric acid stabilised particles, FeOx-citrate, have more efficient heating. This is shown by both the temperature rise of 63.8^{o}C and the calculated SAR and ILP values of 33.9 W/g and 0.81 nHm^{2}kg^{-1} respectively. These values are comparative to other commercially available biologically stabilised super paramagnetic iron oxide nanoparticles (SPIONs)[90]. The tiopronin stabilised particles however, have ΔT = 20.8^{o}C, a SAR of 7.7 W/g and an ILP of 0.18 nHm^{2}kg^{-1}. For comparative reasons, both samples were made to a concentration of 50 mgml^{-1}.

The size and shape of the nanoparticles is partially responsible for this alteration in the temperature achieved. Fe_3O_4 nanoparticles with a single magnetic domain possess the highest potential magnetisation, however agglomeration can occur in which aggregates of multiple nanoparticles assemble. Thus, forming a cluster of particles with multiple domains which when aligned can result in ferromagnetic properties, where the particles retain magnetisation and are not exclusively paramagnetic. Therefore from this data, we can assume that citrate-stabilised Fe_3O_4 has a greater stability towards magnetic agglomeration.

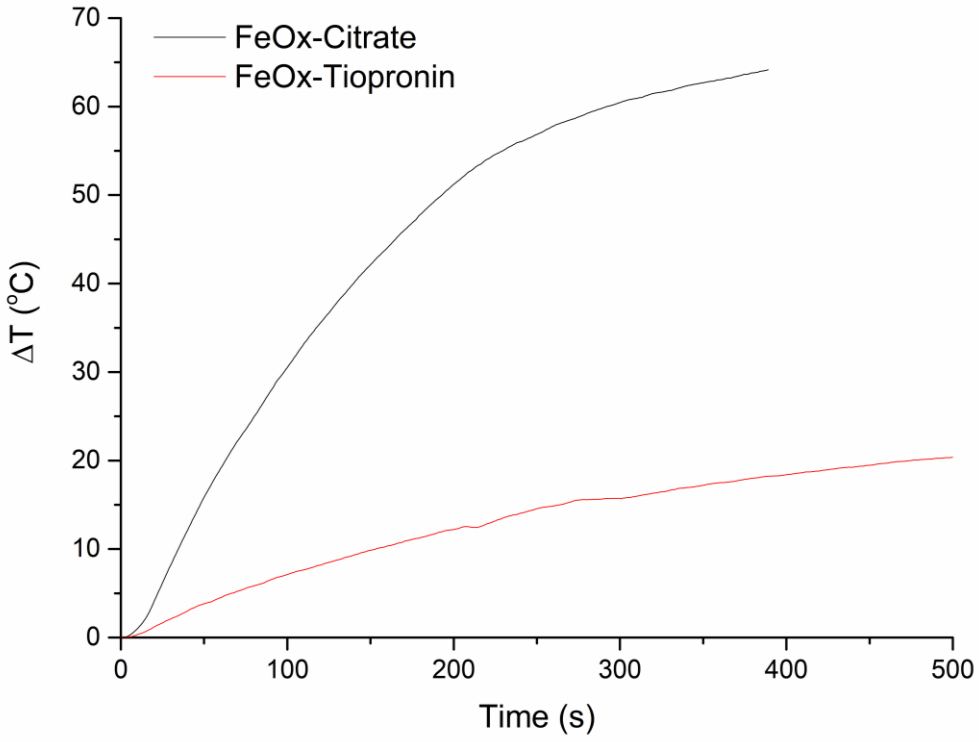

Figure 2.16: Heating curve generated by FeOx-citrate and FeOx-tiopronin from exposure to an external alternating magnetic field in an aqueous solution.

2.3.4.2 Iron oxide – gold nanocomposites

Similarly, MACH analysis was performed on the FeOx-Au_x samples. A similar method was employed where the as-synthesised iron oxide – gold nanoparticles were analysed within a 6 turn electromagnet at a fixed frequency of 964 kHz. Again heating was seen and to varying degrees for different Au concentrations. As shown, the highest temperature recorded was $\Delta T = 17.1^{o}C$ for FeOx-$Au_{0.75}$. Whereas, $\Delta T = 5.0^{o}C$ for the weakest heating FeOx-$Au_{0.25}$. Between these

maximum and minimum heating samples, $\Delta T = 13.3^{o}C$ for FeOx-$Au_{0.5}$, $\Delta T = 11.2^{o}C$ for FeOx-$Au_{1.5}$ and $\Delta T = 9.2^{o}C$ in the case of FeOx-$Au_{3.0}$.

Although these temperatures are much lower than the $\Delta T = 63.8^{o}C$ seen for FeOx-citrate nanoparticles, they are concentration dependent. The as-synthesised Fe@Au nanoparticles are of a much lower concentration, with as little as 5% of the concentration of FeOx-citrate. This also relates to the ILP and SAR values seen in Table 2.1.

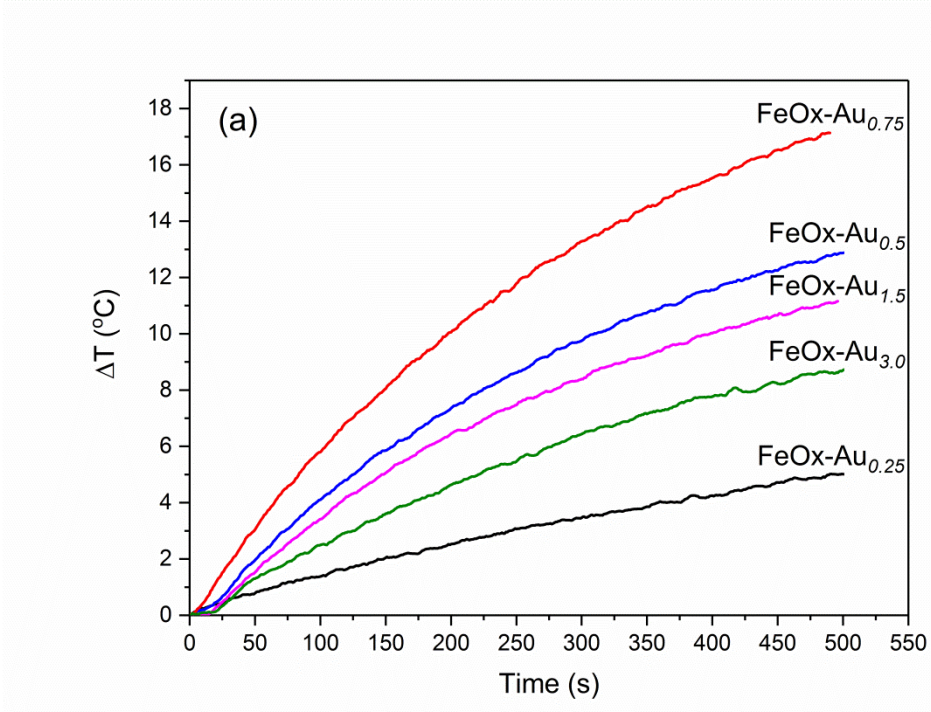

Figure 2.17: Heating curves generated from MACH analysis of FeOx-Au_x nanoparticles. Where x = 0.25, 0.5, 0.75, 1.5 and 3.0 mM concentrations of Au.

Table 2.1. Table showing the comparative values for the concentration of gold (mM), iron oxide particle mass ($mgml^{-1}$), specific absorption rate (SAR / Wg^{-1}) and how this correlates to the intrinsic loss power (ILP / nHm^2kg^{-1})

Sample	**[Au] / mM**	**Particle Mass / $mgml^{-1}$**	**SAR / Wg^{-1}**	**ILP / nHm^2kg^{-1}**
FeOx-tiopronin	0	50	7.7	0.18
FeOx-citrate	0	50	33.9	0.805
FeOx-$Au_{0.25}$	0.25	1.6	39.0	0.925
FeOx-$Au_{0.4}$	0.40	3.7	57.5	1.37
FeOx-$Au_{0.5}$	0.50	3.4	71.9	1.67
FeOx-$Au_{0.6}$	0.60	2.3	78.2	1.86
FeOx-$Au_{0.75}$	0.75	3.3	88.3	2.1
FeOx-$Au_{1.0}$	1.0	2.2	72.4	1.72
FeOx-$Au_{1.5}$	1.5	3.6	51.4	1.25
FeOx-$Au_{2.0}$	2.0	2.8	39.4	0.934
FeOx-$Au_{3.0}$	3.0	2.8	42.9	1.02
FeOx-$Au_{5.0}$	5.0	2.9	36.8	0.852

This table can then be visualised as a graph (Figure 2.18) giving a clear comparison of the SAR and ILP values for the different nanocomposites. It shows how there is an ideal gold concentration of 0.75 mM for the synthesis of highly tuned magnetic gold nanoparticles. This has given rise to an IPL of 2.1 nHm^2kg^{-1}. Even at higher concentrations of gold the ILP is still greater than that of the magnetic precursor FeOx-citrate. Gold concentrations of 3.0 and 5.0 mM have

shown an increase up to 1.02 and 0.852 nHm^2kg^{-1} respectively, compared to FeOx-citrate ILP of 0.805 nHm^2kg^{-1}.

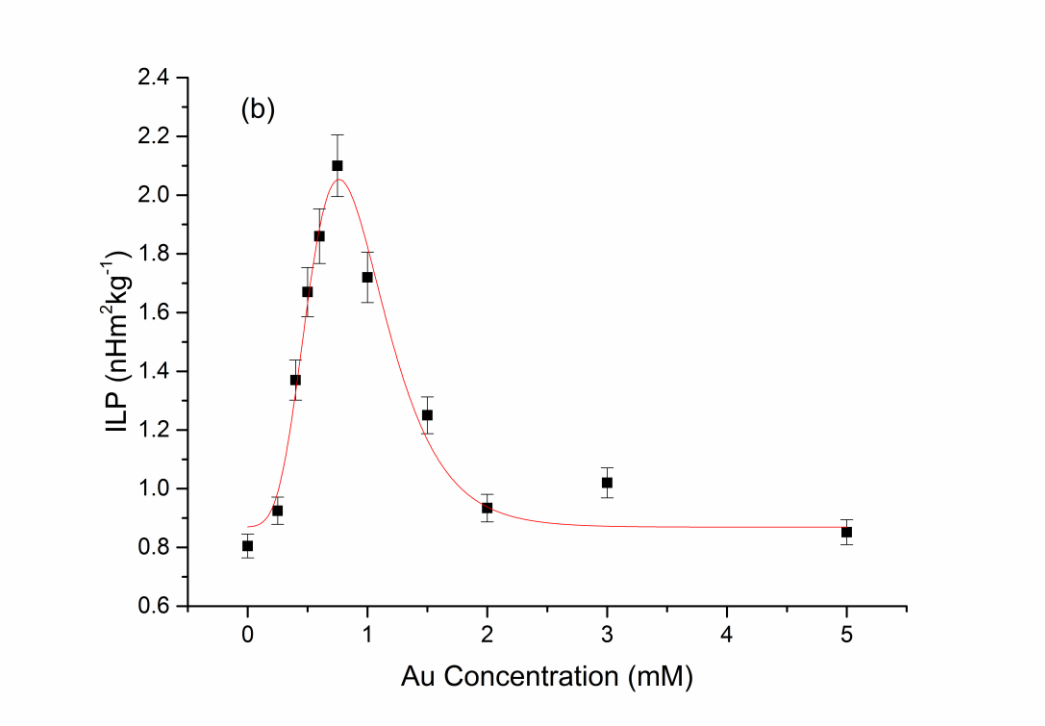

Figure 2.18. The corresponding intrinsic loss parameters across the series, illustrating a ca. 3x increase in heating capacity in the vicinity of x = 0.75 mM.

These figures correspond well with other literature studies performed. For instance, Kandasamy *et. al.* have recently synthesised iron oxide nanoparticles coated with novel short chain surfactants amino-terephthalic acid (ATA) and terephthalic acid (TA) under co-precipitation conditions.[151] These particles are shown to have a SAR in the range of 46.0 – 129.8 Wg^{-1} under specific frequencies. The range of coating of iron oxide nanoparticles in varying surfactants to make the particles more effective for magnetic hyperthermia is always growing.

Table 2.2: Table of particle mass, specific absorption rate (SAR) and intrinsic loss power (ILP) for the comparison of FeOx-citrate to the control samples of FeOx with sodium chloride or hydrochloric acid, FeOx-NaCl and FeOx-HCl respectively.

Sample	**Particle Mass / $mgml^{-1}$**	**SAR / Wg^{-1}**	**ILP / nHm^2kg^{-1}**
FeOx-citrate	50	33.9	0.805
FeOx-NaCl	3.7	35.1	0.834
FeOx-HCl	3.2	35.8	0.870

Finally, to try and establish the effect the gold was having on the ILP, several control experiments were performed which were compared with FeOx-citrate and FeOx-$Au_{0.75}$. It was established whether the ionic strength of the $HAuCl_4$ was having an effect on the structural packing and ordering of the iron oxide particles. This was therefore achieved by substituting $HAuCl_4$ with NaCl within the reaction.

Secondly, the effect the pH had on the reaction mixture was studied. As $HAuCl_4$ is acidic, it was replaced with HCl of an equal concentration to determine if it was this acidic nature of $HAuCl_4$ that increases the ILP values.

From Table 2.2 it can be seen that the neither NaCl nor $HAuCl_4$ had affected the heating potential of FeOx-citrate. As neither the sodium chloride nor the hydrochloric acid had an effect on the ILP values for FeOx-citrate then it determines that the addition of $HAuCl_4$ is the sole cause for the improved hyperthermia. The addition of the gold has caused some morphological changes

which could reduce the amount of agglomeration and loss of superparamagnetism. However, more investigation is needed to determine the causes of these improved results. Guardia *et. al.* have also described the effects of Cl^- ions on the heating achieved *via* magnetic hyperthermia and the growth of dumbbell like Fe-Au particles.[152] Stating that the Cl^- ions aid in the formation of dimers giving a record value of specific absorption rates (SARs) up to 1300 Wg_{Fe}^{-1} at 330 kHz and 24 kAm^{-1} was measured for dimers with an iron oxide domain of 24 nm in size, and concluding that the presence of gold possibly helped the heat dissipation to reach such remarkable values. However these particles were synthesised using a high temperature hydrothermal oleylamine synthesis in contrast to the co-

precipitation used in this thesis.

Likewise, different sizes of iron oxide nanoparticles have been analysed for magnetic hyperthermia.[153,154] With debate still ongoing about the optimum size of an magnetic iron oxide core to be.

This hydrothermal synthetic method was attempted multiple times throughout this research, where the iron salts were dissolved in an organic solvent, 1-octadecene, with oleic acid surfactant, and heated to high temperatures in excess of 320^oC. A constant heating gradient was needed for the monodisperse nature of these particles, which was challenging with the high temperatures required. Literature reports a gradient of 3^oC/min provides the most monodisperse particles. Furthermore, the organic nature of the nanoparticle surface caused unforeseen issues. Attempts to isolate the oleic acid-capped Fe_3O_4 precipitate with large amounts of ethanol did not succeed. As the ethanol was added, the polarity of the

solvent solution changes, which in theory should precipitate Fe_3O_4. However, the yielded product resembled thick black oil, in which there were still residue organic solvents that were unable to be removed via traditional evaporation under reduced pressure due to very high boiling point of 1-octadecene (315^oC). It was concluded that these particles had formed as intended, as they were not a fine a black precipitate and nor did they appear to possess any paramagnetic properties when introduced to a permanent magnetic field.

2.4 CONCLUSION

In conclusion, it can be seen that a simple co-precipitation synthesis of iron salts can produce highly tuneable superparamagnetic iron oxide nanoparticles. The co-precipitation of $FeCl_3$ and $FeCl_2$ with the addition of a stabilising ligand and a reducing agent has repeatedly synthesised SPIONs to a high quality. The particles have been shown to be roughly spherical in shape and composed of a mixture of Fe_3O_4 and Fe_2O_3 compositions as shown from TEM and XRD. This mixture of compositions is due to the readiness of Fe_3O_4 to oxidise in air.

This report has shown that it is possible to change the capping ligands on the nanoparticles to a positive effect. As is seen where citric acid stabilisation was superior to tiopronin giving an ILP increase of 450% from 0.18 to 0.81 nHm^2kg^{-1} for tiopronin and citrate stabilised particles respectively. This has given insight into the continued ability to modify and tune an iron oxide core and how these steps can generate a meaningful contribution to oncology and nanomedicines.

With more research and development this could be a suitable alternative to harsh chemotherapies, radiotherapies and surgeries.

Although there are obvious positives of a non-invasive thermal therapy of a multitude of cancers, this work can also highlight the issues with reproducibility and consistency of iron oxide nanoparticle synthesis. As shown in this data, tiopronin-capped iron oxides yielded a ILP of only 0.18 nHm^2kg^{-1}, which is significantly lower than that synthesised by Thomas *et. al.* which showed a heating ILP of 6.1 nHm^2kg^{-1}. Therefore, it is critical to establish well-known and reliable protocols if the use of iron oxide nanoparticles will ever become truly viable.

This research has also demonstrated that it is possible to further improve the magnetic hyperthermia characteristics of citrate iron oxide nanoparticles by the addition of $HAuCl_4$. The addition of the gold has altered the chemical structure and morphology of the iron oxide and hence increased the magnetic behaviour. TEM has shown that the gold has increased the size distribution of the iron oxide nanoparticles, theorising that some gold coating has been achieved. This has also been confirmed from UV spectrometry which shows a red shift for the gold coated iron oxide nanoparticles. The gold has also formed large particles to which have caused increased agglomeration of the iron oxide nanoparticles

Finally, the gold has been seen to increase the magnetic hyperthermia potential of these particles. From using the citrate-stabilised nanoparticles as a core, the gold has over doubled the ILP values seen form 0.81 up to 2.1 nHm^2kg^{-1}. This is a highly positive outcome for these particles showing that gold has a positive effect

on hyperthermia, with a high degree of potential future applications, such as cancer therapy. It is yet to be fully understood why the addition of gold in a specific concentration has made such a vast change to the heat generation. Although, a possible hypothesis for this is that at x = 0.75 mM $HAuCl_4$, the gold nanoparticles are formed in the most ideal spatial distribution to disrupt the overall localised magnetic field of the iron oxide aggregates. So that when the iron oxide particles cluster, each individual magnetic moment does not interact with as many nearby particles. It is believed here that x = 0.75 mM, is this optimum value where the gold structures are not too big nor too small, so that they disrupt this relationship between the individual iron oxide particles.

The gold also exhibits strong surface plasmon resonance bands, seen in the UV spectrum, which is a key property of photodynamic therapy of cancer cells. Combined with hyperthermia, there is the potential to make a multimodal cancer therapy treatment.

More applications are also possible for the iron oxide nanoparticles other than hyperthermia. There is current investigation into the use of these particles as MRI contrast agents (see Chapter 4) and in ultrasound probes, but only initial studies have currently been explored. With promising data, it will be a pathway to the development of a whole new category of possible medicines.

3 SURFACE ENHANCED RAMAN SCATTERING

3.1 INTRODUCTION

SERS spectroscopy is a powerful vibrational analysis leading to highly selective structural detection.[155] Excitation of localised surface plasmon resonances enhances the electromagnetic fields and allows detection of very low concentrations of analyte. This amplification of vibrational signal from light occurs mainly in small nanoscale gaps, cracks, crevices and points of a plasmonic material. These so-called 'hot spots' are therefore desirable and typically occur in noble metals i.e. gold, silver, copper.[156,157]

As such, gold nanoparticles have been widely explored as a highly selective sensing medium through the optically sensitive SPR bands. As detailed in Chapter 1, this is useful for SERS detection of molecules and antibodies in biomedicine and security devices. The use of gold as a SERS substrate has developed greatly in recent years; changing from rough electrochemically etched materials with nanoscale gaps but poorly defined uniformity and reproducibility,[158,159] to well defined uniform nanoparticles of many differing morphologies, such as spheres, rods and stars. For instance, *Chaney et. al.* show how highly structured and orientated silver nanorod arrays can produce a high sensitivity SERS substrate.[160]

Gold nanostars have been widely used recently as a possible highly sensitive and selective SERS probe with Khoury *et. al.* showing the difference in SERS enhancement factors for variable sized gold nanostars with an highest average enhancement of 5×10^3 for 53 nm sized stars.[161]

In this Chapter, an exploration into the developments and use of gold nanostructures is seen. Gold nanoparticles can be seen in a wide range of sizes, structures and designs. Gold nanospheres are the most common and simplest synthetically, being achieved *via* a citrate reduction to form mostly uniform monodisperse spheres. As well as spheres, gold nanostars are seen as desirable nanostructures for SERS spectroscopy. Most notably, they contain highly tailorable peak aspect ratios which contribute to the localised SPR bands and produce vast amplification due to high levels of 'hot spots' *via* 3-dimensional orientation and clustering.

Furthermore, the development of iron oxide – gold nanocomposite materials, synthesised in Chapter 2, could prove of interest. With the ability to hold both magnetic properties and the optical localised SPR properties is of value.

3.2 MATERIALS & METHODS

3.2.1 Materials

All chemicals and reagents were used as received and without further purification. For gold synthesis; chloroauric acid ($HAuCl_4$), silver nitrate ($AgNO_3$), citric acid (99%), and ascorbic acid were all purchased through Sigma Aldrich. For iron

oxide synthesis; iron(III) chloride hexahydrate ($FeCl_3.6H_2O$) (99%), iron(II) chloride tetrahydrate ($FeCl_2.4H_2O$) (98%), ammonium hydroxide (NH_4OH) (25% in water w/w), citric acid (99%) and trisodium citrate dihydrate were all purchased through Sigma Aldrich. The dyes used for Raman analysis were crystal violet (CV) and malachite green isothiocyanate (MGITC), purchased through Sigma Aldrich. All water used was ultrapure and distilled to 18.0 MΩ.

3.2.2 Synthesis of gold nanospheres

Gold nanoparticles were synthesised as previously detailed via the Turkevich synthesis. As before, a solution of trisodium citrate dihydrate (1.6 mL, 0.5%) was added to a solution of $HAuCl_4$ (20 mL, 0.18 mM) at 65 ^oC. Upon a colour change from yellow to red, the mixture was then boiled at 100 ^oC for 20 minutes.

3.2.3 Synthesis of gold nanostars

The synthesis of gold nanostars was achieved *via* the reduction of $HAuCl_4$ with ascorbic acid and silver nitrate aiding the seed mediated growth of the vertexes. Briefly, $HAuCl_4$ (400 μL, 10 mM) and $AgNO_3$ (40 μL, 10 mM) were well dispersed in H_2O (20 mL) and mixed for 2-3 minutes at room temperature; giving a molar ratio of Au/Ag = 10. To this an aqueous solution of ascorbic acid (80 μL, 100 mM) was quickly added and mixed *via* agitation (avoid stirring) for 20 seconds. A colour change from colourless to a red-blue hue occurred. The

nanostars were then collected *via* centrifugation (10000 rpm, 10 mins) and re-dispersed in water.

3.2.4 Synthesis of iron oxide – gold nanocomposites

Synthesis of FeO–Au nanocomposite materials was achieved as previously stated (Chapter 2). Briefly, Fe_3O_4 nanoparticles were initially synthesised *via* a co-precipitation method in which iron chloride salts, $FeCl_3.6H_2O$ and $FeCl_2.4H_2O$, were dissolved in H_2O in a 2:1 Fe^{3+}:Fe^{2+} stoichiometric molar ratio. The orange solution was heated to 70 ^oC for 30 minutes in a N_2 atmosphere where NH_4OH (5 mL, 28%) was added dropwise turning the solution black and heated for a further 30 minutes. Citric acid (4 mL, 0.5 g/mL) was added and the temperature was raised to 90^oC under reflux for 60 minutes.

$HAuCl_4$ (20 mL, 0.2 mM) was heated to boiling after which the citrate stabilised Fe_3O_4 (1 mL, 0.3 $mgmL^{-1}$) was added instantaneously. With continued heating and mixing for 10 minutes and addition of excess citric acid (0.5 mL, 0.25 mg), the solution turned from pale yellow to red. The solution was then cooled to room temperature, washed with H_2O and collected with a permanent magnet.

3.2.5 Microscopy

TEM images were obtained using a JEOL JEM-2100F TEM microscope using an accelerating voltage of 120 kV. TEM samples were prepared by aqueous liquid drop of as-synthesised nanoparticles onto perforated carbon grids. Ultraviolet

visible absorption spectra were obtained on a Hitachi U-2900 UV-Vis spectrophotometer from 300 – 1100 nm wavelengths with a step size of 0.5 nm. The analyte was as-synthesised in an aqueous medium and recorded in a 1.0 mL plastic cuvette.

3.2.6 Surface enhanced Raman spectroscopy

SERS was achieved using a Renishaw inVia™ Qontor® confocal Raman microscope from wavenumber 600 – 2000 cm^{-1} with a 633 nm and 785 nm laser using an extended grating scan type. Laser power was scalable from 10% - 0.1% depending on the levels of enhancement to reduce the possibility of saturation of the spectra.

Samples preparation was done by mixing the nanoparticles (Au or FeO-Au) with a crystal violet (CV) or malachite green isothiocyanate (MGITC) dye in a given molar ratio. Ratios used were 9:1, 1:1, 1:9, Au:dye equating to 9, 5 or 1 μM solutions. This means that using CV and MGITC stock solutions prepared at 10 μM and diluted to as low as 1 μM was achieved with the SERS active particles. Samples (20 μL) were dropped onto a slilica substrate and either scanned as solution or scanned after dried in a vacuum (0.4 bar) for 4 hours.

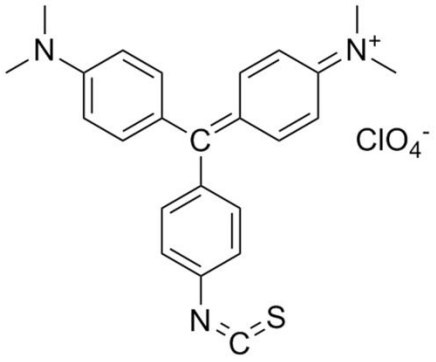

Malachite green isothiocyanate

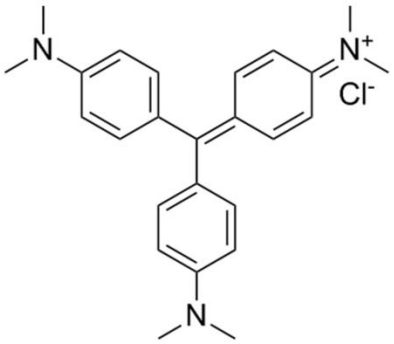

Crystal violet

Figure 3.1. Chemical structures of the triarylmethane-based Raman sensitive dyes malachite green isothiocyanate (MGITC) and crystal violet (CV).

3.3 RESULTS & DISCUSSION

3.3.1 Synthesis

Spherical gold nanoparticles were synthesised using the Turkevich method of the reduction of Au^{3+}, in $HAuCl_4$, with citric acid. Typically, $HAuCl_4$ was brought to boiling where citric acid was then added. Citrate here acted as both a reducing agent and a stabilising ligand to form the monodisperse particles, leaving a ruby red solution.

For gold nanostars (Au Stars) a synthetic procedure as described by Cheng *et al.*[162] and further studied by Raghavan *et al.*[163] was used. This seedless method to spiked gold nanoparticles was a facile one pot synthesis, in which a solution of $HAuCl_4$ and silver nitrate ($AgNO_3$) were mixed in a precise molar ratio of 10:1 Au:Ag. Reduction of Au was achieved at room temperature with ascorbic acid.

The silver ions in solution act as nucleation points for the formation of the spikes. A colour change from colourless to blue is observed as the nanostars form.

Iron oxide - gold nanocomposite materials were synthesised by the same route detailed in Chapter 2, with the iron oxide cores being formed *via* the co-precipitation method. Excess citric acid was used as a stabilising ligand and as a reducing agent upon the post-synthetic addition of chloroauric acid. $HAuCl_4$ was added at a concentration of [0.4 mM], giving rise to a red magnetic precipitate and colourless supernatant when collected on a permanent magnet. This goes some way to showing that the gold is bound to the magnetic iron oxide cores.

Literature studies show the iterative hydroxylamine seeding to promote the reduction of Au^{3+} on the iron oxide surface to create a core-shell nanoparticle.[50] This synthetic method was attempted in this thesis, however the seeding was unsuccessful with little to no coating of gold achieved on the iron oxide surface as determined though absorption spectrometry.

3.3.2 Microscopy

For the high levels of enhancement required for SERS spectroscopy, a high degree of uniformity in the nanostructures is required. To assess the gold nanoparticles synthesised TEM images were collected.

Gold nanospheres are shown in Figure 3.2.a), which shows highly dispersed uniform gold nanoparticles of a mean diameter of 4 nm and standard deviation, σ,

of 0.85 (measured over 113 particles). This is common for a citrate reduction synthesis and has been well documented in literature.

Figure 3.2.b) shows the TEM images of gold nanostars. These nanoparticles are much larger than and less uniform that the spherical particles, with some particles reaching in excess of 200 nm from point to point. These nanostars are much more aggregated than the spherical nanoparticles, which can be attributed to the lack of stabilisation by ascorbic acid of the high surface charges. Furthermore, the gold nanostars have no functional polymer coating, which can be considered to improve the stability and dispersion of the particles. Noticeably, the points of the particles are sharp in nature, and not rounded. This is important for the localised surface plasmon resonance absorption profile of the particles and will be ideal for the surface enhanced Raman scattering spectroscopy.

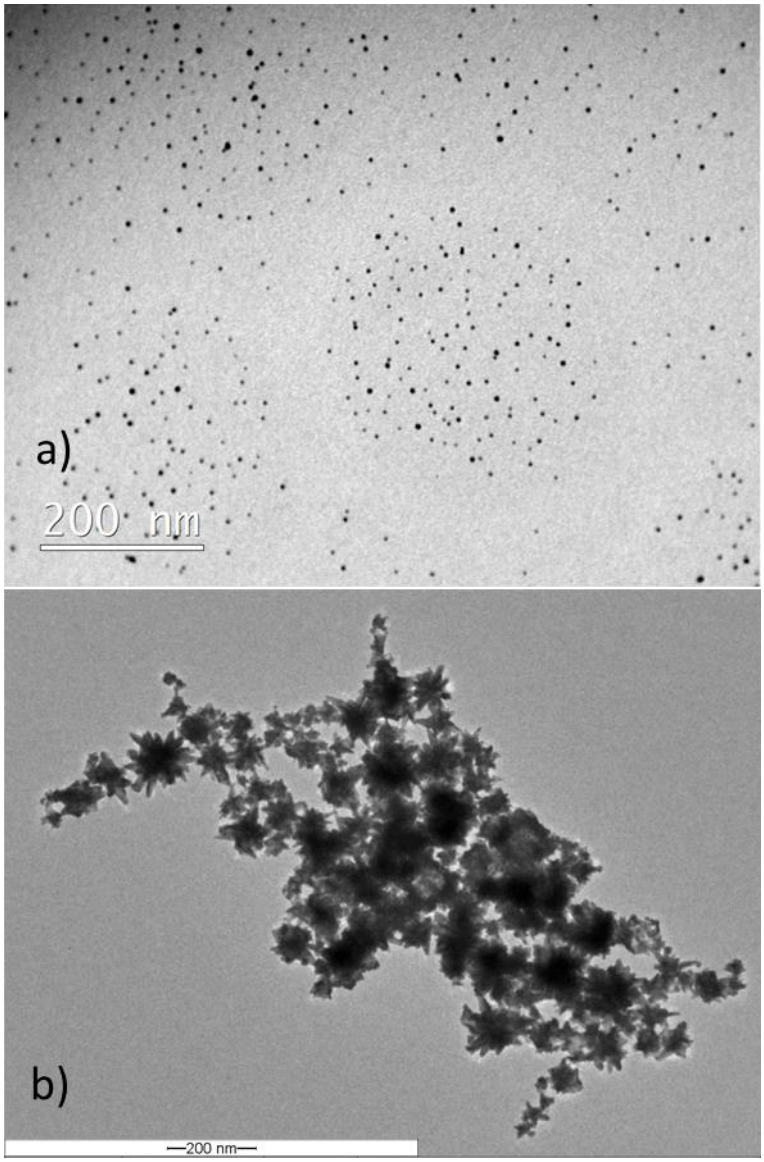

Figure 3.2. TEM micrographs of a) spherical gold nanoparticles synthesised *via* the Turkevich method of Au^{3+} reduction by citric acid and b) spikey gold nanostars formed with silver nitrate ($AgNO_3$) and ascorbic acid.

The UV/Vis absorption spectra of the gold nanoparticles (Figure 3.3) shows this increased size of the nanostars structures. Firstly, it can be seen that the absorption peak for gold nanospheres is narrow and at the standard 540 nm. The gold nanostars however, have a red-shifted absorption with a broad spectrum which

peaks at 642 nm. This red shift is synonymous with growth of a gold nanoparticle, and this broad overall spectrum is seen because of several factors. Firstly, from the TEM images we can see there is a lack of uniformity in the particles size. Additionally, constructive overlap of the absorption profiles of the core of the particle and the spikes can contribute. The centre of a nanostar is representative of a nanosphere, thus absorbing in the 550 nm region, as with all colloidal gold nanospheres. This is combined with the higher 700 nm absorption of the longer aspect ratio spikes. Raghavan *et al.*[163] however synthesised gold nanostars with high uniformity and polydispersity resulting in dual plasmonic bands.

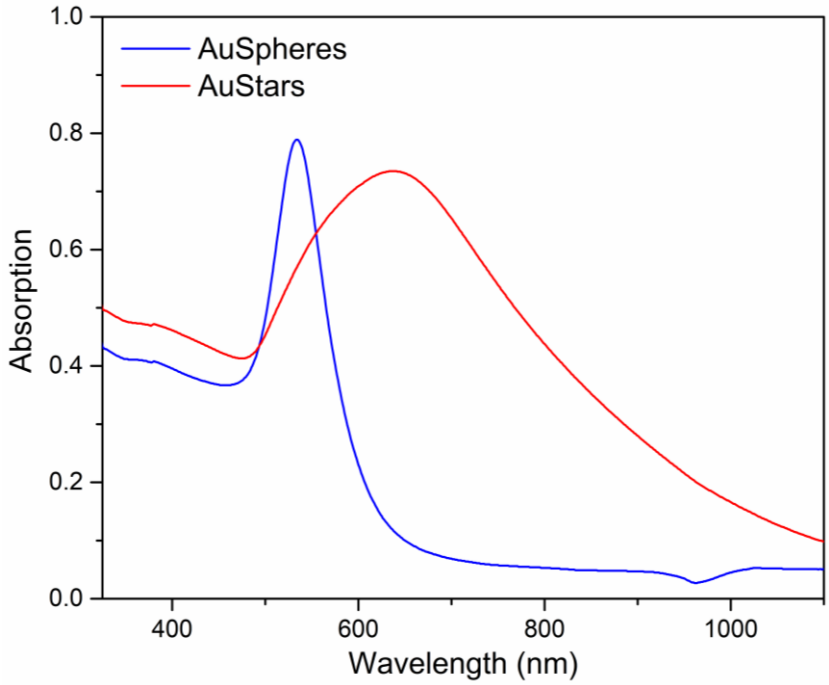

Figure 3.3. Spectra of the different morphologies of gold nanostructures, nanospheres and nanostars. Note that the Au stars have a much broader absorption profile due to the variation in size and star spike aspect ratio.

3.3.3 Surface enhanced Raman scattering

3.3.3.1 Gold nanoparticles for SERS

Surface enhanced Raman scattering spectroscopy was firstly carried out to see the degree of enhancement achievable from the gold nanostars particles. For this Figure 3.4 shows the comparison between the surface enhancement of crystal violet (CV) dye for the gold nanostars and nanospheres. In the same molar ratio of 1 part gold, 1 part CV, relating to an overall concentration of CV of 5 μM, the spectra align exactly, with major peaks at 1170 cm^{-1}, 1375 cm^{-1} and 1618 cm^{-1}.

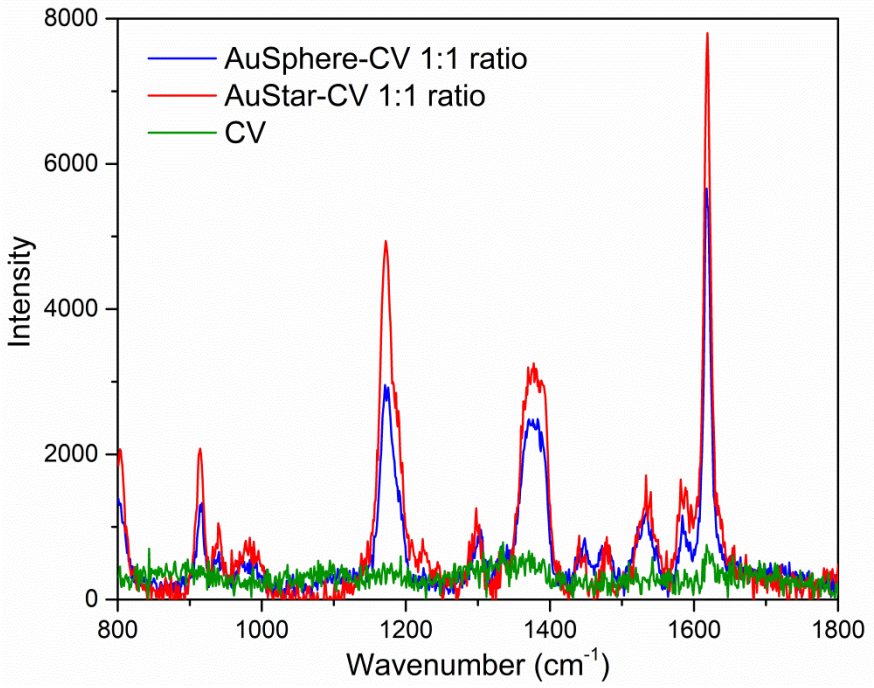

Figure 3.4. SERS spectra contrasting the enhancement of crystal violet (CV) dye with spherical gold nanoparticles and spikey gold nanostars.

From these spectra gold nanostars are shown here to have a higher intensity and greater effect of SERS than the spherical gold particles. It can be theorised that the localised spatial proximity of each spike is in a more suitable position for surface enhancements. The peak to peak intensities of this spectra are shown as 730, 5600 and 7800 for CV, gold spheres and gold stars respectively.

It is important to note that these solutions are assumed to be homogenous, therefore the concentration of gold nanostructures – CV will be constant. This means that the data is highly reproducible.

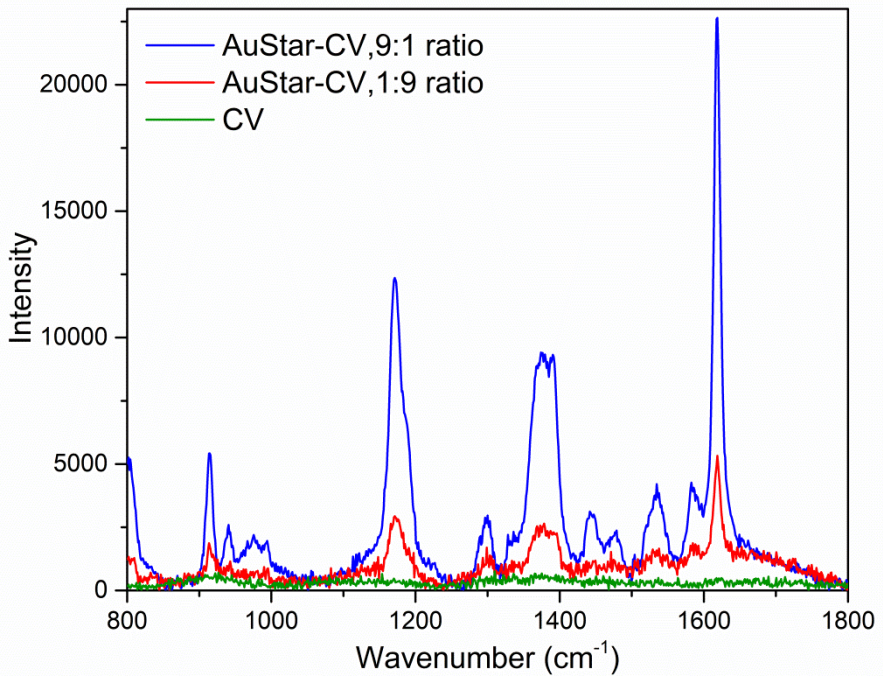

Figure 3.5. Raman spectra comparing the SERS signal enhancement of crystal violet (CV) solution without gold nanoparticles and with Au nanostars in either a 9:1 or 1:9 Au:CV molar ratio. Greatest enhancement was achieved using a 9:1 ratio of Au stars.

Furthermore, Figure 3.5 shows the difference concentration and the molar ratio of the SERS substrate (here gold nanostars) has on the levels of enhancement achieved. The SERS effect was greatest when the molar ratio between gold nanostars and CV was at 9:1, (i.e. a 1.0 μM CV solution) giving a max intensity of 22500 at 1620 cm^{-1}. This is over a four-fold increase in SERS compared to Au stars in a 1:9 molar ratio with CV (9.0 μM CV solution). At the same wavenumber of 1620 cm^{-1}, intensity = 5300. This can be attributed to both an increase in number of gold particles able to enhance the spectra, and a less saturated solution of CV. Also, compared to the intensity of 500 for pure CV, the gold nanostars can be stated to have a 50x peak to peak intensity enhancement.

To determine if there is a noticeable effect when analysing SERS for a sample as a solution or dried on a substrate, gold nanostar solution was further compared to an equal amount of solution dried on a silica glass substrate under vacuum. Both materials greatly enhance the Raman signals of CV having a peak intensity of 21200 at the Raman shift of 1618 cm^{-1}.

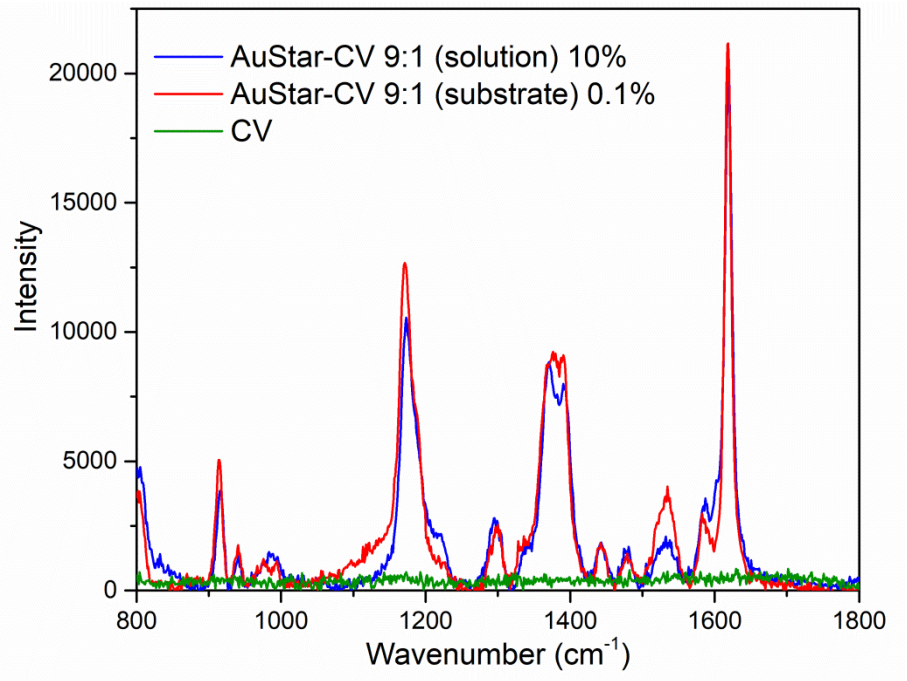

Figure 3.6. Raman spectra showing SERS effect on crystal violet (CV) when gold nanostars (9:1 Au:CV) are in solution or dried onto a silica substrate. Enhancement peaks are comparable but 633 nm laser power for aqueous solution = 10%, and dry substrate = 0.1%

Although both materials give comparable intensity in a 9:1 Au:CV ratio, it has to be noted that the laser power for each spectra is different. To avoid saturation of the spectrum, the dried nanostar substrate was obtained at a far reduced power of 0.1%. However the same signal intensity was achieved for the solution based sample at 10%. This shows that the surface bound dried sample is a much more effective SERS analyte. Reasoning for this is due to the increased fluidity in a solution, resulting in a constant relocation of nanoparticles and a shifting of potential SERS active sites. Whereas, when dried to a silica surface the nanostars are locked into position. Homogeneity of the sample can also be affected by a

surface bound sample. Meaning there could likely be areas of the silica surface with a much greater concentration of both dye and SERS analyte giving rise to a pseudo-signal of higher than average intensity.

This can be seen in Figure 3.7 where the issues with the homogeneity of the dried material can be seen. At given locations on the slide, there will be significant amounts of gold and CV giving a strong Raman enhancement. Whereas, due to the so called 'coffee-ring' effect, the distribution of the gold nanoparticles is not even across the slide.[164] So although the spectra are of CV and have the same predominant peaks, they are all unfortunately at different enhancement levels.

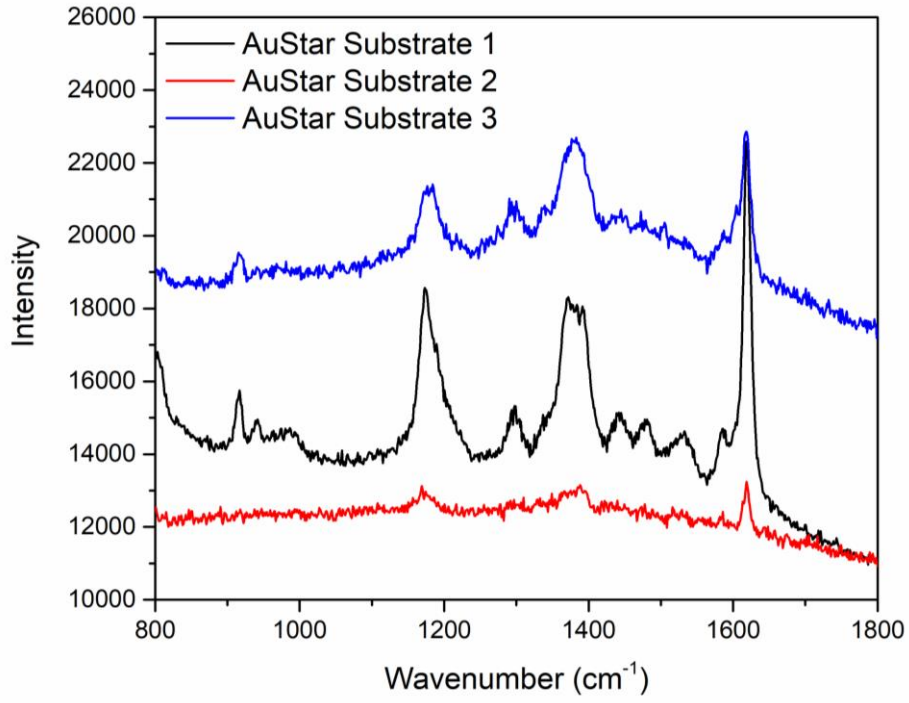

Figure 3.7 Raman spectra showing SERS effect on crystal violet (CV) when gold nanostars are dried on substrate. Note that the enhancement is different across all three substrates showing that reproducibility is a key issue.

3.3.3.2 Iron oxide - gold nanoparticles for SERS

Using Au nanoparticles as a control, it can be seen that FeO-Au nanoparticles can enhance some of the same Raman peaks, but only on a silica substrate. The standard peaks for malachite green isothiocyanate (MGITC) enhancement are seen at 1176 cm^{-1}, 1366 cm^{-1} and 1618 cm^{-1}.[165]

In solution there is very little intensity over the whole spectra. This can be attributed to the lack of localised gold concentration, i.e. the gold nanoparticles within the FeO-Au nanomaterial are too far apart (as seen in the TEM images of Chapter 2, Figure 2.7) that resonance 'hot spots' cannot be formed.

The sharp peaks occurring in the FeO-Au do coincide with MGITC enhanced with Au spheres at some wavenumbers, such as at 1170 cm^{-1}, 1380 cm^{-1} and the pair of peaks at 1600 cm^{-1}. The intensity of these peaks is also much lower than those seen for Au spheres.

Some of the peaks in FeO-Au on the substrate do not correspond to any of the MGITC peaks. Nor can they be attributed to the inherent Raman signal of Fe_3O_4 which is present in the nanomaterial.[166] The peak at 1000 cm^{-1}, for instance, has high intensity and very sharp, which is accredited to the Si-O-Si asymmetric bond stretching vibration in the glass substrate.[167]

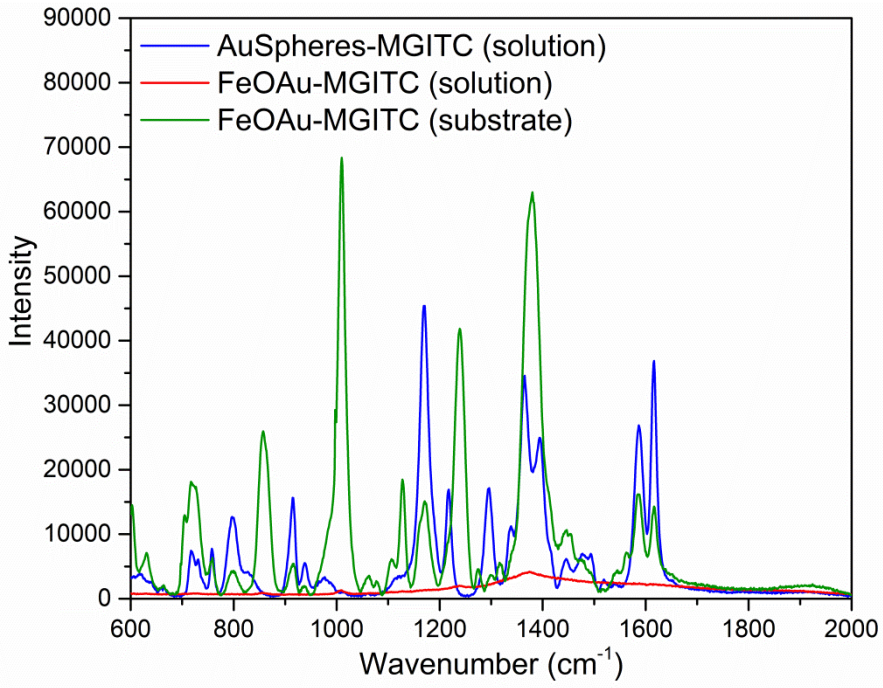

Figure 3.8. SERS spectra of malachite green isothiocyanate (MGITC) dye showing the enhancement of peaks using gold nanoparticle solution, and iron oxide – gold nanocomposite solution and substrate.

3.4 CONCLUSION

In conclusion, it has been shown that it is possible to synthesise gold containing nanoparticles of different morphologies in a facile manner for the use as surface enhanced Raman scattering spectroscopy probes. It can be shown that gold nanostars are a more effective SERS substrate than gold nanospheres due to the optimal spatial positions of the spikes. Au stars gave rise to a 1.4 fold increase in enhancement over Au spheres and a 50-fold peak-to-peak increase over pure crystal violet. Furthermore, a 9:1 Au:CV molar ratio is seen to be most sensitive, showing a 4x enhancement over a solution containing a a 1:9 Au:CV molar ratio.

Finally, FeO-Au nanoparticles have been synthesised and exhibit a unique SERS spectra of MGICT, which still needs further development. Some of the characteristics of the SERS spectra are dissimilar between the FeO-Au and Au enhancement. It could be possible there is an artefact causing these peaks, as seen with the silica substrate, or more interesting perhaps the magnetic iron oxide cores are manipulating the gathering of SERS spectra.

4 MULTIMODAL IMAGING

4.1 INTRODUCTION

In this chapter the aim is to further investigate the adaptability of iron oxide nanoparticles. As discussed in Chapter 1, iron oxide nanoparticles have been a key material for MRI over the years and have seen wide development in multiple fields and technical applications, including biomedicine, due to the manipulation of its diverse properties and high intrinsic magnetisation. Likewise, more and more development into multi-modal imaging is occurring to collate as much data as possible from each probe material, and achieve a two-in-one imaging probe. For this we have shown the development of an iron oxide core nanoparticle being efficiently coated directly with a photoacoustic dye. Using well-known esterification chemistry we have been able to covalently bind carboxyl-functionalised PA dyes onto the surface of the iron oxide nanoparticles.

With the increased potential for exploiting magnetic properties, iron oxide nanoparticles are therefore ideal material candidates for bio-optical probe development. Using different synthetic routes and surface modifications, nanoparticles can be tailored for very specific applications. The size and morphology can be manipulated to the preferential formation to deliver particular properties. This can be achieved through the various synthetic routes in which

iron oxide can be formed. The most common in literature being co-precipitation and hydrothermal syntheses.[44,168,169] The former being used commonly as a facile mechanism for aqueous soluble nanoparticles.

This also applies to the surface functionalisation of the particles; which can give improved aqueous stability, bio-distribution, and add or enhance intrinsic properties.[18] Nanoparticles have to be stabilised in solution due to the high surface to body ratio and charged surface. This is typically achieved with neutral organic molecules and polymers, or inorganic and metallic shells.[14,142,170,171] Thus aiding the colloidal stability and reducing aggregation whilst improving the possibility for further functionalisation. Furthermore, surface functionalisation can add targeting moieties for even greater biological affinity and impact.[172] Using a photoacoustic organic dye to fulfil this role is of particular interest as they have the potential to both stabilise the colloidal solution and impart novel characteristics through its natural absorption profile. Thus, iron oxide based nanoparticles can lead to an attractive multimodal imaging platform with many future possibilities.

As MRI contrast agents, iron oxide nanoparticle materials have changed the way we look inside the human body due to its infinite penetration depth and high spatial resolution and contrast of soft tissues. As a non-radiative imaging technique, high strength magnetic fields are deployed to detect the relaxation of atomic nuclei. Contrast agents are employed in MRI to facilitate the modification of the relaxation times T_1 and T_2. Fe_3O_4 nanoparticles give a strong T_2 contrast in which the signal intensity decreases in a T_2-weighted image. FeOx nanoparticles can also be considered more biologically sustainable and less toxic than some

commonly used gadolinium based T_1 contrast agents which increase the signal intensity on T_1-weighted images.[173] For example, literature reports show the *r1* and *r2* contrasts of various iron oxide nanoparticles, each functionalised or synthesised by various routes and resulting in different values.[119] With the highest *r2* values seen in literature being within the order of >800 $mM^{-1}s^{-1}$ for Zn^{2+} doped magnetic nanoparticles.[120] In very recent developments, ultra-small iron oxide nanoparticles have been seen to enhance the T_1 contrast; making a Gd-free positive contrast agent, with very little chance of iron overload in the body.[121]

Multispectral Optoacoustic Tomography (MSOT) is another attractive bio-imaging tool due to the ability to generate anatomical images with a deep penetration depth (5-6 cm) whilst keeping a high spatiotemporal resolution, all whilst being a non-radiative process. Typically; a short wave near-infrared (NIR) source pulses and irradiates the biological tissue and photoacoustic (PA) probe. The NIR pulse is absorbed, which generates a small temperature spike resulting in the generation of low scattering sound waves *via* thermoelastic expansion in the tissue medium and the probe molecule. Ultrasound transducers detect the incoming acoustic waves which can then be processed into ultrasound images. One beneficial property of an exogenous PA dye is the ability of spectral unmixing. Endogenous molecules such as oxy (HbO_2) and deoxy-haemoglobin (Hb), melanin and water all exhibit a characteristic photoacoustic spectrum.[174] Because of this, literature studies typically use NIR photoacoustic (PA) dyes, with absorption in the region of 700 – 1000 nm. Most commonly used dyes are aromatic organic structures, such as indocyanine green (ICG), methylene blue,

thalocyanine, and chlorin e6 (C e6)[104]. With MSOT, it is then possible to track the dye and analyse specific cellular or molecular processes. MSOT imaging is therefore a useful tool for the imaging of tissue oxygenation and hypoxia, and blood vessel imaging for the likes of vascular disease or melanoma.[175]

Henceforth, multimodal probe development for biological imaging is quickly becoming significant to facilitate the fast, effective and efficient gathering of the vast amounts of data necessary for quick, decisive medical diagnoses. This interest ultimately leads to multimodal probes with a combination of MSOT and MRI. The advantage of a dual modality MSOT-MRI probe is to provide the combination of detailed functional and molecular information from MSOT with the very high anatomical resolution given by MRI imaging. Combining the properties of multiple techniques gives the ability to analyse quickly and decisively by providing complementary information. Dual modality imaging techniques are common in bio-imaging; typically with MRI scanners often paired with positron emission tomography, in PET-MRI scanners to provide complementary information, with the use of nanoparticle-based probes.[176] With new development of imaging probes, variations of multimodality can be achieved, as such, recent developments have shown the use of magnetofluorescent T_2 MRI contrast agents for targeted MR and fluorescence imaging of neural stem cells.[177]

With this desire to formulate a multimodal imaging probe based on iron oxide nanoparticles, in this manuscript we report on the synthesis and characterisation for novel photoacoustic functionalised iron oxide nanoparticles. Attachment of ICG and Flamma®774 dyes were achieved through activation and esterification between the magnetic particles cores and PA molecule; with the structural

characteristics of the iron oxide cores largely unchanged. This initial study reveals that Flamma®774 PA molecule attachment can achieve suitable MRI contrast agents that also produce a significant MSOT signal, under optimum conditions.

4.2 MATERIALS & METHODS

4.2.1 Materials

Indocyanine green N-hydroxysulfosuccinimide sodium salt (ICG sulfo-NHS) and Flamma®774 N-hydroxysulfosuccinimide sodium salt (Flamma®774 sulfo-NHS) were supplied by BioActs (BioActs, Korea).

Iron(III) chloride hexahydrate ($FeCl_3.6H_2O$), iron(II) chloride tetrahydrate ($FeCl_2.4H_2O$), ammonium hydroxide (NH_4OH), citric acid, 2-(N-morpholino)ethanesulfonic acid (MES) buffer, 1-[3-(dimethylamino)propyl]-3-ethylcarbodiimide hydrochloride (EDC) , N-hydroxysulfosuccinimide sodium salt (Sulfo-NHS) and chlorin e6 trisodium (C e6) were all acquired from Sigma Aldrich. All reagents were used as receive without purification with ultra-pure double distilled water (18.2 MΩ)

4.2.2 Synthesis of iron oxide nanoparticles

The iron oxide nanoparticles were synthesized *via* a co-precipitation method previously used but with modifications[168]. This comprised of dissolving a 2:1

stoichiometric ratio of iron(III) : iron(II) in water and the addition of a strong base in an inert atmosphere.

In a typical reaction, iron(III) chloride, $FeCl_3.6H_2O$ (135 mg, 50 mM) and iron(II) chloride, $FeCl_2.4H_2O$ (50 mg, 25 mM) were added to H_2O (5 mL) degassed under the continuous flow of N_2, forming an orange solution. The solution was heated at 70^oC for 30 minutes upon which ammonium hydroxide, NH_4OH (28%, 5 mL) was added dropwise. The solution immediately formed a black precipitate which was then heated at 70^oC for 30 minutes. Citric acid (4 mL, 0.5 gmL^{-1}) was added as a stabilising ligand and heated at 90^oC reflux for 1 hour. The black precipitate was then collected on a permanent magnet and washed with H_2O (10 mL x3). The strong ferrofluid was dried under reduced pressure leaving a black powder.

This reaction, although reproducible, produced nanoparticles that were not stabilised with a surfactant or a ligand. This results in a nanoparticle solution that readily undergoes aggregation to a point where the desired properties were no longer achievable. When the material aggregates, they become too large and heavy to be suspended in solution, therefore sonication of the material was used to re-disperse the colloidal suspension.

4.2.3 Photoacoustic dye functionalisation of iron oxide

For the attachment of photoacoustic (PA) ligands, shown in

Figure 4.1, to the iron oxide nanoparticle cores, a modification of a previous technique for esterification was used. This focused on the attachment of three PA

dyes, chlorin e6, ICG, and Flamma®774. For easy of experimentation and in the interest of time, ICG and Flamma®774 were purchased having already been activated with the sulfo-NHS moiety.

Initial reactions involved the attachment of C e6 onto the iron oxide core. This was trialled *via* multiple techniques. Firstly, a control experiment was carried out, to determine if any conjugation of the PA dyes would be achieved through the mixing of pre-synthesised iron oxide nanoparticles and the stock solution of dye chlorin e6. The dark green solution was mixed overnight, for 24 hours, and the resultant precipitate was collected on a permanent magnet. This extracted the black iron oxide cores out of solution, leaving the unattached green solution of the dye C e6.

Further experiments involved in-situ coating of the nanoparticles, therefore, during nanoparticle fabrication, C e6 was added, to act as a stabilising ligand, in part of the commonly used citric acid that had been used previously.

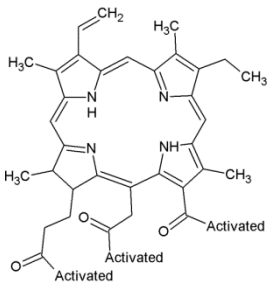

Chlorin e6

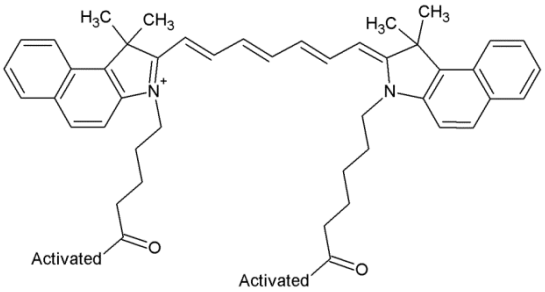

Indocyanine green

Figure 4.1. Chemical structure of activated photoacoustic dyes chlorin e6 and indocyanine green. Where the activated notation represents the Sulfo-NHS leaving group.

4.2.4 Activation of photoacoustic dyes

Ultimately, the reaction of C e6 and the iron oxide core was achieved by using a sulfo-NHS leaving group to activate the dye making esterification possible therefore, using a modified synthesis that has been previously reported on, activation of the dye was carried out. To achieve the catalysed reaction C e6 (1 mM, 663 μg), as a green powder, was dissolved in MES buffer (aq) (pH 4.0, 30 mL, 50mM). To this green solution, EDC (0.1 M) and sulfo-NHS (5.3 mM) were added and stirred at room temperature for 10 mins. This activated the C e6 molecules and addition of FeOx NP's (1 mL, 30mg/ml) whilst mixing overnight lead to conjugation of the dye to the nanoparticles and magnetic separation resulted in a dark green ferrofluid.

Furthermore, the addition of ICG and Flamma®774 was achieved *via* the same synthetic route as C e6, however, the PA dye needed no activation and was used as purchased [BioActs, Korea].

In this reaction, a NHS-activated photoacoustic derivative (ICG sulfo-NHS (10 mM) or Flamma®774 sulfo-NHS (10 mM)), was added to a solution of MES buffer (pH 6.5, 50 mM, 15 mL) giving a pale green solution. Addition of the as-synthesised iron oxide nanoparticles (1 mL, before citrate stabilisation), and mixing overnight at room temperature formed the conjugated nanoparticles and a

dark green solution. The nanoparticle product was collected on a permanent magnet and washed with H_2O (10 mL x3). The resultant magnetic precipitate was collected on a permanent magnet and of a dark green colour.

4.2.5 Particle size and morphology

Particle size and morphology was performed using a combination of transmission electron microscopy (TEM), dynamic light scattering (DLS), and UV-vis spectroscopy. TEM was performed using a JEOL JEM-2100F TEM microscope using an accelerating voltage of 120 kV. TEM samples were prepared by aqueous liquid drop of as-synthesised ferrofluid probe onto perforated carbon grids. DLS was performed on the aqueous ferrofluid with a Malvern Zetasizer Nano, using 1 mL samples in a 4.5 mL plastic cuvette. Ultraviolet visible absorption spectra were obtained on a Hitachi U-2900 UV-Vis spectrophotometer from 300 – 1100 nm wavelengths with a step size of 0.5 nm. The analyte was as-synthesised in an aqueous medium and recorded in a 1.0 mL plastic cuvette.

4.2.6 Animal model

All procedures performed in this study involving animals were in accordance with the ethical standards of the Institutional Animal Care and Use Committee (A*STAR Biological Resource Centre, Singapore, IACUC #151085/140898). The animals used (8-10 weeks-old females, 20-25 g) were NRC nude mice (U87 mg xenograft) from InVivos (Singapore). 8 – 10 weeks old NcR nude female mice

weighing between 20-25 g were used for this study. 200 ul of 5 x 10^6 U87MG cells (ATCC) mixed with matrigel in 1:1 volume was inoculated on the right flank of the mouse and imaging procedures were performed 3 weeks later.

4.2.7 Multispectral optoacoustic tomography

Multispectral optoacoustic tomography (MSOT) was performed on an iThera Medical MSOT inVision 512-echo small animal imaging system[178]. Assisted by Dr Amalina Attia and Dr Ghayatri Balasundaram, phantom samples were 180 μL and were prepared in a 10 cm cylindrical polyurethane phantom fabricated to simulate the characteristics and optical properties of mice and submerged in a water bath to aid with acoustic detection. Detection wavelength was in the range of 680 nm – 980 nm at 5 nm intervals across a length of 5 mm of the phantom at 0.5 mm slices.

Briefly, a tuneable optical parametric oscillator (OPO) pumped by an Nd:YAG laser provides excitation pulses with a duration of 9 ns at a repetition rate of 10 Hz with a wavelength tuning speed of 10 ms and a peak pulse energy of 100 mJ at 730 nm. Ten arms of a fibre bundle provide even illumination of a ring-shaped light strip of approx. 8 mm width. PA signals were acquired using a 512-element concave transducer array spanning a circular arc of 270°. During MSOT measurements, the phantom is translated through the transducer array along its axis to acquire the transverse image slices set.

For *in vivo* imaging, FeOx-774 (100 mM w/Fe in 5 μL saline) was administered through an intratumoral injection. Ultrasound gel was applied on the mouse skin

surface and measurements were recorded in 34°C water for good acoustic coupling. An animal holder with a thin polyethylene membrane was used to prevent direct contact between the mouse and the water. A volumetric region of interest (ROI) consisting of multiple transverse slices with an inter-slice distance of 0.5 mm. Ten frames were acquired and averaged for each wavelength (680, 700, 760, 770, 780 (FeOx-774 absorption peak), 790, 800 (isobestic point of Hb and HbO2), 850, 900 nm). MSOT imaging was performed pre-injection, and 15 minutes post-injection.

4.2.8 Image reconstruction and processing

MSOT images were reconstructed using a model-linear algorithm *via* ViewMSOT proprietary software. Thereafter, spectral unmixing was performed to resolve individual components from different chromophores in the system. For each pixel in the image, the method fits the total measured optoacoustic spectrum to the known absorption spectra of the individual chromophores, based on least-squares linear regression.

4.2.9 Magnetic resonance imaging

MRI relaxivity of the nanoparticles were evaluated by using a 7-Tesla Bruker Clinscan MRI system with the assistance of Michael Ng, Francesca Mandino and Dr Joanes Grandjean from the Singapore bio-imaging consortium, A*STAR. T2-weighted relaxation times were determined from a multiecho spin-echo sequence

(repetition time (TR): 4000 ms; TE: 17.9–250.6 ms). *r2* relaxivities were obtained from the slope of 1/T2 versus molar [Fe] concentration plots. Phantoms were prepared in 500 μL samples in a 1 mL plastic syringe, placed inside the coil.

Animals were anesthetised using Isoflurane. Briefly, anesthesia was induced with 4% isoflurane; animals were then positioned on a MRI-compatible cradle. Isoflurane was lowered to 1.5% for the whole MRI-scanning session. Animal temperature was maintained at 37°C. Data were acquired on an 11.75 T Biospec (Bruker BioSpin MRI, Ettlingen, Germany) equipped with a BGA-S gradient system, a linear volume resonator coil for transmission and a 10 mm multi-purpose surface receiver coil positioned over the tumour. Images were acquired using Paravision 6.0.1 software. Gradient-Echo MRI images were acquired using a fast low angle shot (FLASH) sequence: field of view (FOV) = 20 × 20 mm², number of slices = 20, slice thickness = 0.4, slice gap = 0.3 mm, MD = 192 x 192, TR = 15 ms, TE = 3 ms, flip angle = 50°, volumes = 1, bandwidth = 250 kHz. Two FLASH images were acquired: one before the contrast agent injection, as baseline, and one 5' after the injection.

4.3 RESULTS & DISCUSSION

4.3.1 Synthesis

All iron oxide nanoparticles were synthesised *via* the co-precipitation method, in which iron(II) and iron(III) salts were dissolved aqueously, heated and reduced with a strong ammonium hydroxide base. The citrate stabilised nanoparticles are

hereon referred to a FeOx-citrate. Further functionalisation of the particles was achieved through the novel covalent attachment of the photoacoustic dyes. The surface attachment between the iron oxide particles and sulfo-NHS activated dyes was a modification of a synthesis reported by Gil-Tomas *et. al.*[179] The activation of the dye allows facile attachment of the molecule to the Fe-OH surface of the FeOx nanoparticles (Figure 4.2) *via* a common NHS esterification mechanism.[180]

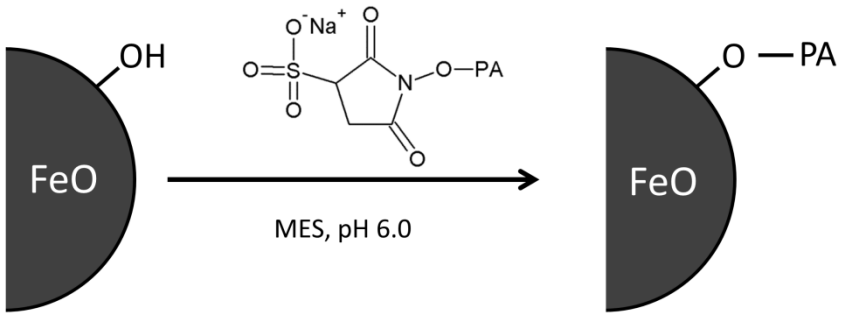

Figure 4.2. Reaction scheme of the photoacoustic molecule attachment to iron oxide nanoparticle surface, where PA represents the photoacoustic dyes Chlorin e6, indocyanine green or Flamma®774

The first dye attached was Chlorin e6 (C e6). The sodium salt of the molecule provided a facile base for activation. The carboxyl end groups made esterification a possibility with the hydroxyl surface of the iron oxide *via* a condensation reaction. This process was then catalyzed, as shown by Figure 4.3 by EDC in the presence of sulfo-NHS.

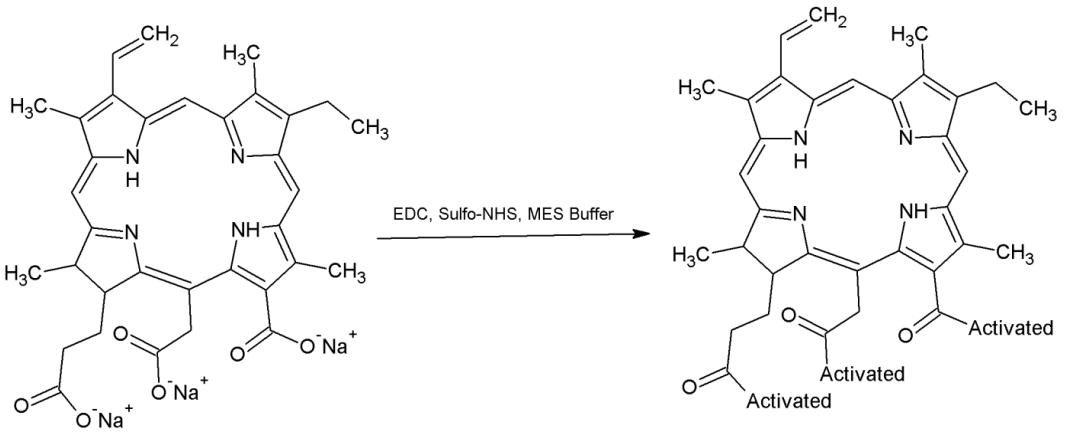

Figure 4.3. Reaction scheme for the activation of chlorin e6 trisodium salt using 1-[3-(dimethylamino)propyl]-3-ethylcarbodiimide hydrochloride (EDC) and N-hydroxysulfosuccinimide (Sulfo-NHS) in a 2-(N-morpholino)ethanesulfonic acid (MES) buffer solution.[179]

The other dyes include indocyanine green and Flamma®774, which were purchased with the Sulfo-NHS functional group pre-attached. These iron oxide core particles are therefore referred to as FeOx-ICG and FeOx-774 respectively. The final products were all dispersible in water and formed strong magnetic ferrofluids.

4.3.2 Chlorin e6 functionalisation

4.3.2.1 Characterisation of nanostructures

To show the attachment of the PA dye was successful, UV was a critical tool for analysis. This allowed detailed optical absorption profiles for the newly formed particles and for us to assess if the dye had bound to the surface of the iron oxide

core. Such is shown in Figure 4.4, where we see the absorption profiles of FeOx-Ce6 and free unbound C e6. The absorption is strong for that of unbound C e6 with a strong peak in the NIR range at 650 nm. Upon addition of the iron oxide core the peak remains, showing conjugation has been successful, although the signal is less intense and has red shifted to 680 nm.

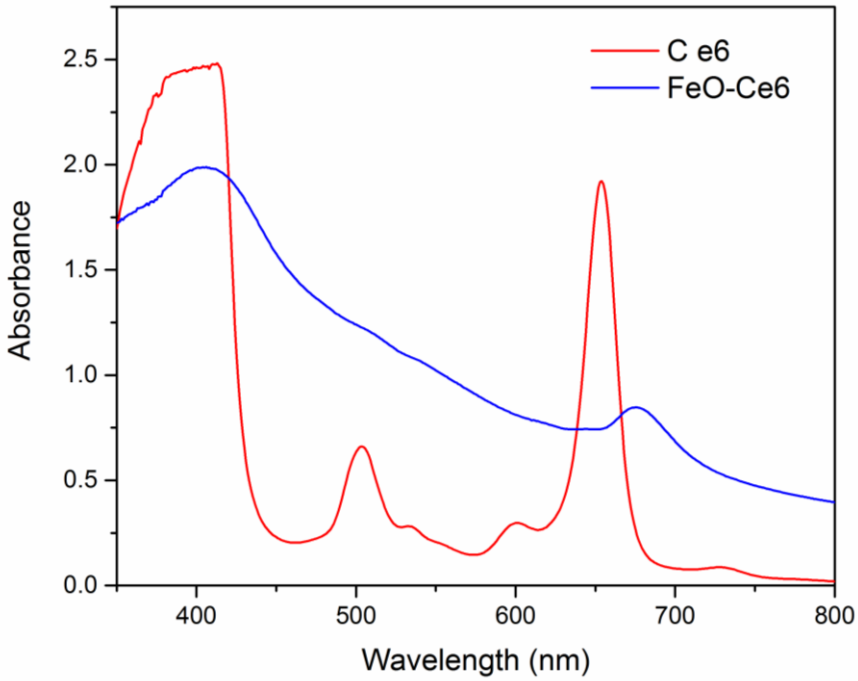

Figure 4.4. UV/Vis absorption spectra of chlorin e6 conjugated iron oxide and free unbound chlorin e6 showing the characteristic near IR peak in both samples.

4.3.2.2 Multispectral optoacoustic spectroscopy

As seen from the UV absorption, the nanoparticles do have a NIR absorption profile, therefore allowing for MSOT spectroscopy to be obtained. To confirm the enhanced conjugation when catalysed with Sulfo-NHS and EDC, a study was performed with both activated and non-activated C e6. Using a small amount of

aqueous sample in a phantom, Figure 4.5 shows the activated material has greater signal intensity. From this, we established that the activation has caused covalent binding through the condensation reaction mentioned beforehand. Whereas, when non-activated C e6 was reacted in the same conditions, we believe this signifies only physical absorption of the dye onto the surface has been achieved.

This is also shown in the PA spectra that are obtained from the MSOT spectroscopy (Figure 4.6). Both the activated and non-activated C e6 compounds produce a PA signal, however the activated has approximately a two-fold intensity increase. This helps to confirm that catalysing the reaction with Sulfo-NHS to activate the carboxyl group on the chlorin e6 dye establishes a higher degree of coordination.

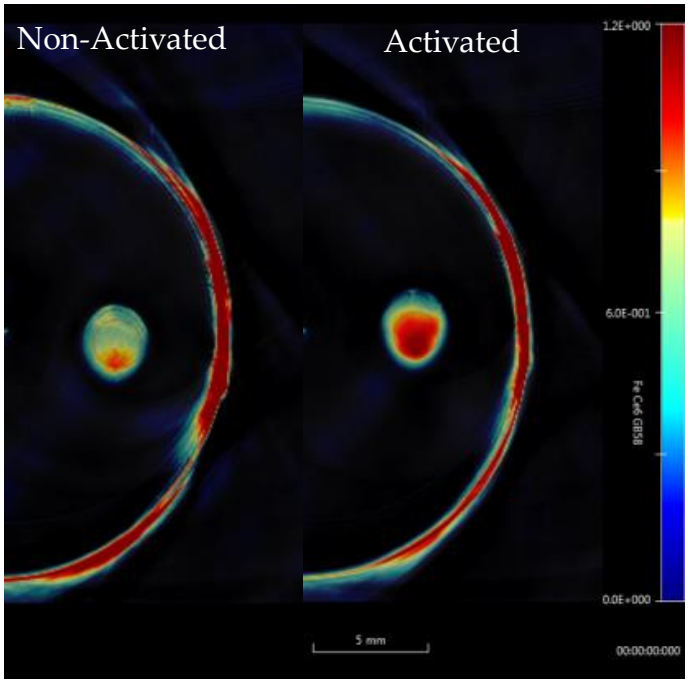

Figure 4.5. Multispectral optoacoustic image of chlorin e6 coated iron oxide (FeOx-Ce6) particles and the difference in photoacoustic signal intensity when synthesised with a) non-activated chlorin e6 trisodium and b) activated dye chlorin e6 sulfo-NHS

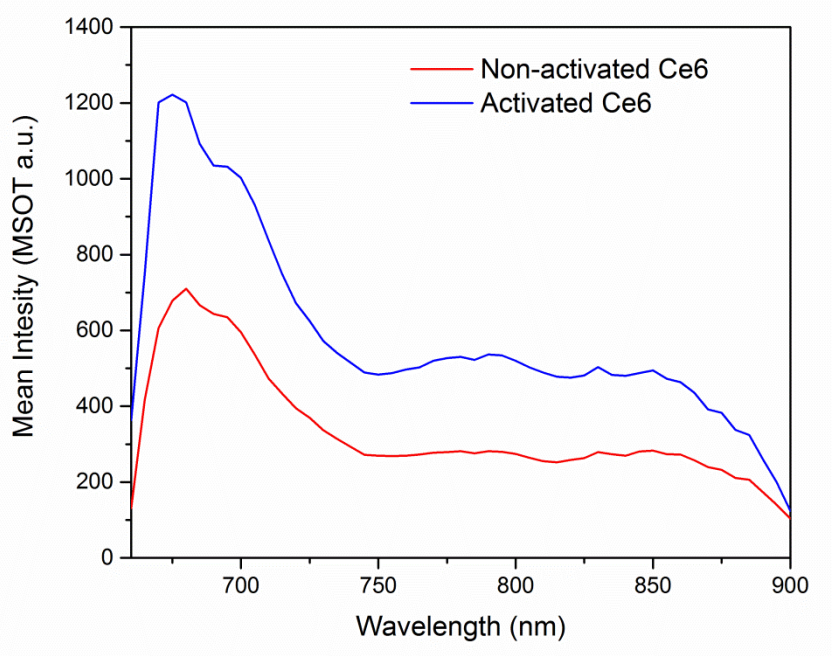

Figure 4.6. Photoacoustic spectra of the different synthetic routes to FeOx-Ce6 production and the increase in MSOT intensity when using the activated chlorin e6 dye

Due to the good PA intensity achieved from the iron oxide nanoparticles, it becomes important to check how spectral un-mixing could be possible with these probes. As previously detailed, spectral un-mixing is critical in MSOT spectroscopy. It is vital to be able to identify the exogenous probes from the endogenous contrast agents. For this we looked at multispectral analysis of Deoxy-Heamoglobin (Hb), Oxy-Heamoglobin (HbO_2) and Iron Oxide Chlorin e6 nanoparticles. The spectra in Figure 4.7 show that we can see the major PA peak of FeOx-Ce6 which occurs at 680 nm. This occurs at the lower limit of the near IR wavelength range for MSOT spectroscopy therefore when *in-vivo* analysis is performed there is a large similarity between the FeOx-Ce6 and Hb at these low

wavelengths. Furthermore, at higher wavelengths the FeOx-Ce6 signal will be masked by the HbO_2 present. This makes the detection of the nanoparticles difficult in the current system.

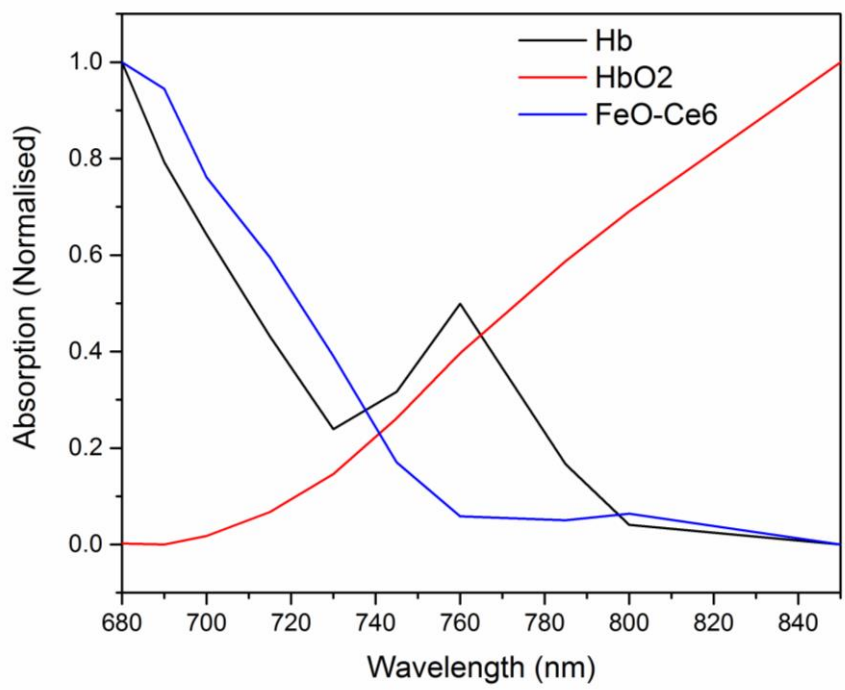

Figure 4.7. *In-vivo* MSOT spectrum for FeOx-Ce6 particles and endogenous contrast molecules oxy- and deoxy-haemoglobin (HbO_2 and Hb) showing the absorption profile of FeOx-Ce6 is too similar to Hb for accurate spatial un-mixing.

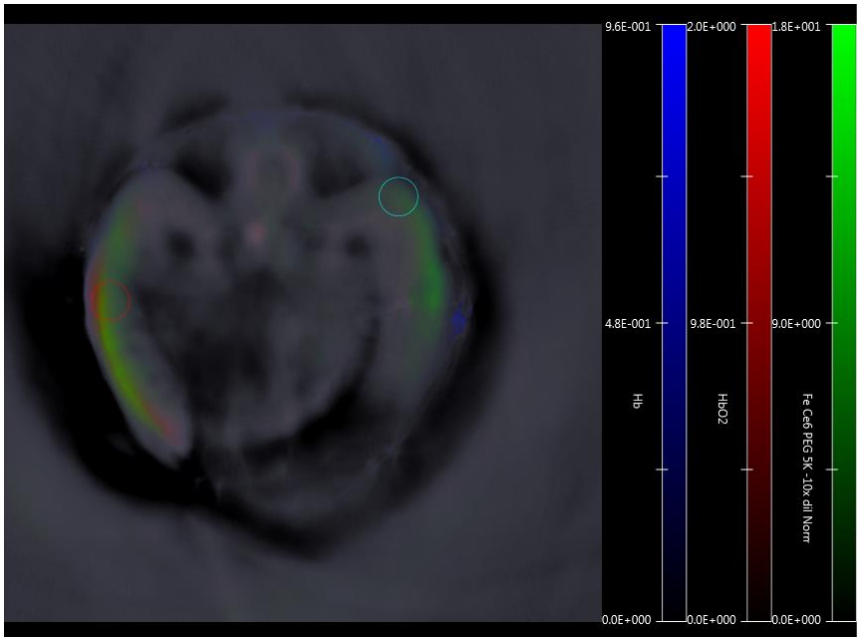

Figure 4.8. *In-vivo* MSOT image of a mouse flank showing there has been no accumulation of the iron oxide chlorin e6 imaging probe (FeOx-Ce6) resulting in poor signal intensity.

Due to this difficulty un-mixing the spectra of FeOx-Ce6 from Hb, the *in-vivo* analysis of the mouse flank (Figure 4.8) showed very mixed signal intensity. It was unable to detect the nanoparticles sufficiently to be clinically useful. Another issue that needed to be overcome was absence of particle accumulation in the tumour site. The nanoparticles were injected intravenously through the tail vain and should be retained for a greater length in the tumour. As this accumulation cannot be seen it is most probable that the nanoparticles have aggregated in solution before administration. This resulting hydrodynamic radius of a cluster of nanoparticles is too great and becomes readily filtered and collected by the liver.

4.3.3 ICG and Flamma®774 functionalisation

Due to the issues surrounding the spectral un-mixing of FeOx-Ce6, this section goes into the research involving the PA dyes indocyanine green (ICG) and Flamma®774. Both of these dyes are known for their PA properties with absorption and emission at a higher wavelength than chlorin e6 at approximately 800 nm.

4.3.3.1 Characterisation of nanostructures

Electron microscopy shows the single core size and structure of the nanoparticle formations before and after dye conjugation. As seen in the TEM images and corresponding histograms (Figure 4.9), the citrate-capped nanoparticles, FeOx-citrate, are of a spherical shape with a mean core diameter of 9 ± 3 nm with some polydispersity. The microscopy also shows that the synthesis of a FeOx-PA dye nanoparticle has little effect on the morphological behavior of the particles. ICG capped nanoparticles have a mean diameter of 8 ± 2 nm, whilst Flamma®774 capped FeOx has a mean diameter of 9 ± 3 nm as shown by the histograms and in Table 4.1. This is common and comparable with previously synthesized nanoparticles formed *via* co-precipitation methods.[168]

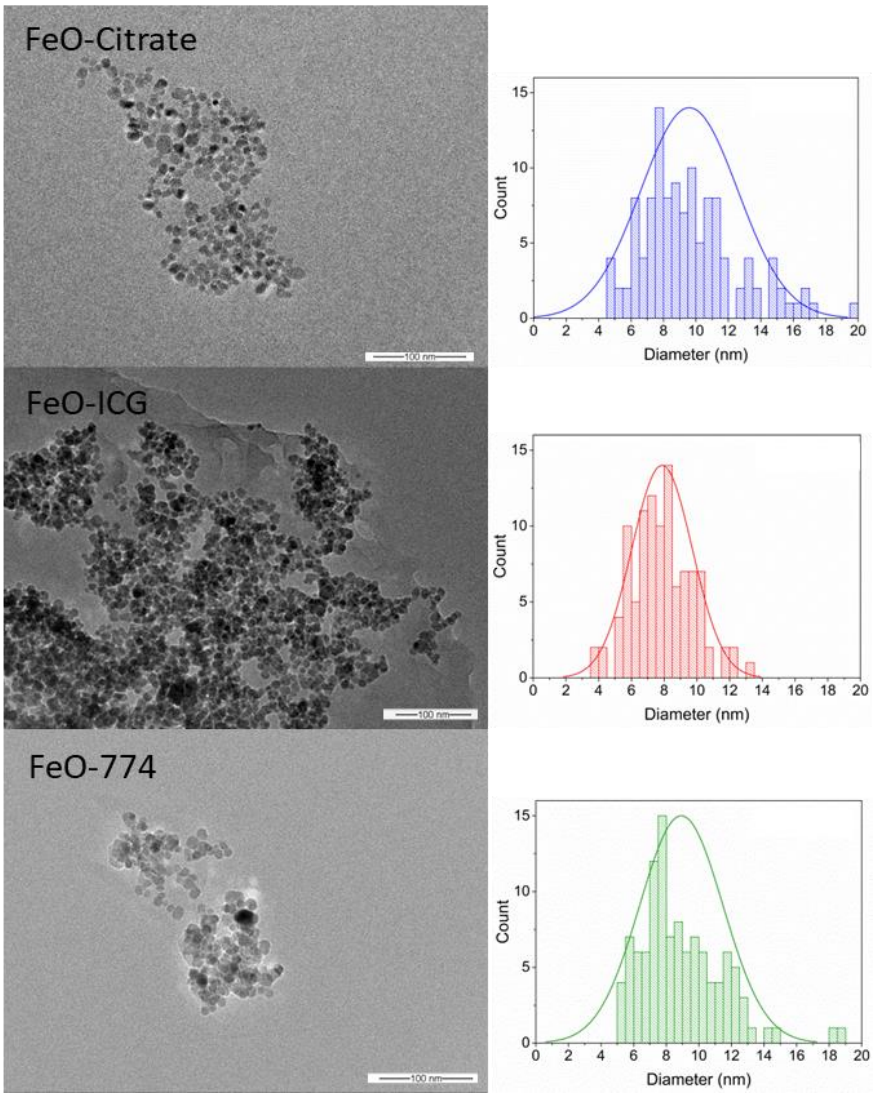

Figure 4.9. TEM images of citrate-capped iron oxide nanoparticles, FeOx-citrate, and photoacoustic-capped iron oxide nanoparticles, FeOx-ICG and FeOx-774. Included are the respective histograms for the diameter of the particles, showing the similar sizes for the functionalised nanoparticles, spherical morphology and aggregation.

Table 4.1. Crystallite size and particles surface charge for the iron oxide and iron oxide – photoacoustic nanoparticles determined *via* TEM and DLS characterisation.

Sample	TEM / nm	DLS / nm	PDI	Zeta potential / mV
FeOx-citrate	9 ± 3	110	0.235	-21.4
FeOx-774	8 ± 2	150	0.239	-24.0
FeOx-ICG	9 ± 3	310	0.363	-16.9

However, the TEM images show that there is aggregation of the nanoparticles when stabilised with both citrate and the PA dyes. This was confirmed with dynamic light scattering (DLS) showing *in situ* agglomeration with Z-average hydrodynamic diameter, φ_H, of 110 nm and polydispersity index (PDI) of 0.24 for FeOx-citrate (Table 4.1). DLS also showed that the PA dyes were less effective stabilizing ligands as the commonly used citrate capping agent. φ_H is in the order of 310 nm and 150 nm for FeOx-ICG and FeOx-774 respectively, with ICG being the least effective stabilising ligand and showing the most polydisperse of the particles, with PDI of 0.36.

The clustering of the nanomaterials is random in nature and has no defined orientation.[181] The main driving force in aggregation is the charged nature of the surface of the individual particles. All synthesized samples hold a negative zeta potential. FeOx-ICG has the weakest negative charge at -16.9 mV, which contributes to the greater aggregation seen.

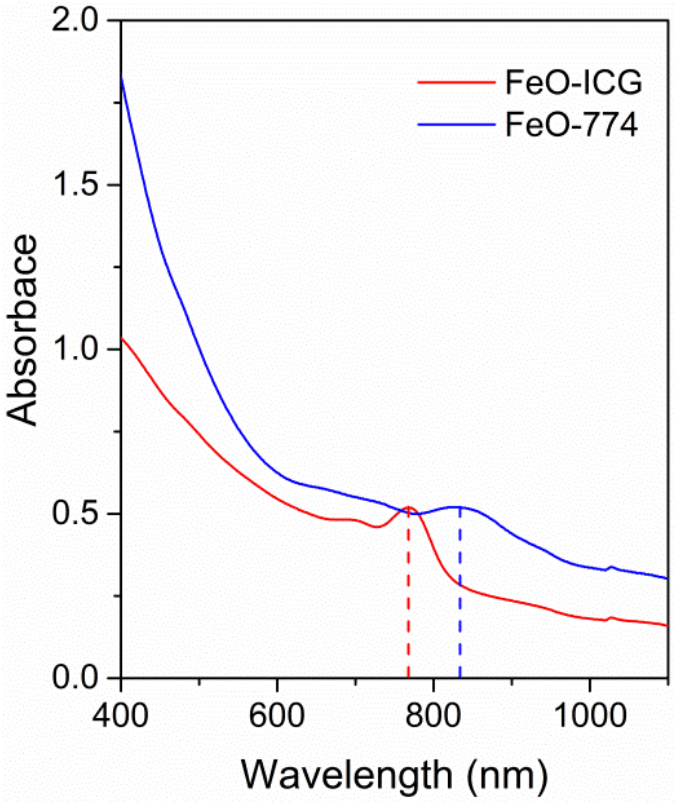

Figure 4.10. UV-visible absorption spectra for probe particles FeOx-ICG and FeOx-774. Near IR absorption of the particles is shown at 830 nm for FeOx-ICG and 780 nm for FeOx-774.

Verification for the attachment of the PA dye onto the surface of the iron oxides can be seen in the UV-vis absorption spectra in Figure 4.10. After thorough extraction of the iron oxide cores through magnetic extraction and washing with H_2O, the absorption peak for ICG and Flamma®774 are both visible at 830 nm and 780 nm respectively. This is in accordance with the standard absorbance of unbound free ICG, at 800 nm, and Flamma®774, at 774 nm. This shows a redshift in the absorption of the dyes which is synonymous with the molecule being bound to the metallic particle core.

4.3.3.2 Multispectral optoacoustic tomography

The attachment of a photoacoustic molecule to the surface of the iron oxide nanoparticles has allowed us to perform optoacoustic tomography to achieve a multimodal probe. The photoacoustic spectra and the subsequent images were all achieved using a polyurethane phantom model. The photoacoustic spectra (Figure 4.11) were plotted in contrast with the endogenous contrast agents oxy (HbO_2) and deoxy-hemoglobin (Hb). For an exogenous contrast agent to be visible, the photoacoustic spectra must not have interference from any of the internal biological contrasts. Figure 4.11 shows MSOT absorption spectra for Fe-ICG and FeOx-774 which are represented with peaks of 790 and 780 nm respectively. These wavelengths fall between the 755 nm peak of Hb and the rising absorbance of HbO_2, thus making spectral unmixing of the probe possible against these endogenous contrasts.

In contrast, the photoacoustic spectra of FeOx-citrate has low intensity and is not sufficient to un-mix the signals for the HbO_2 spectra. Therefore, with the conjugation of the PA dyes, ICG or Flamma®774, however, the photoacoustic signal has been amplified making spectral un-mixing possible.

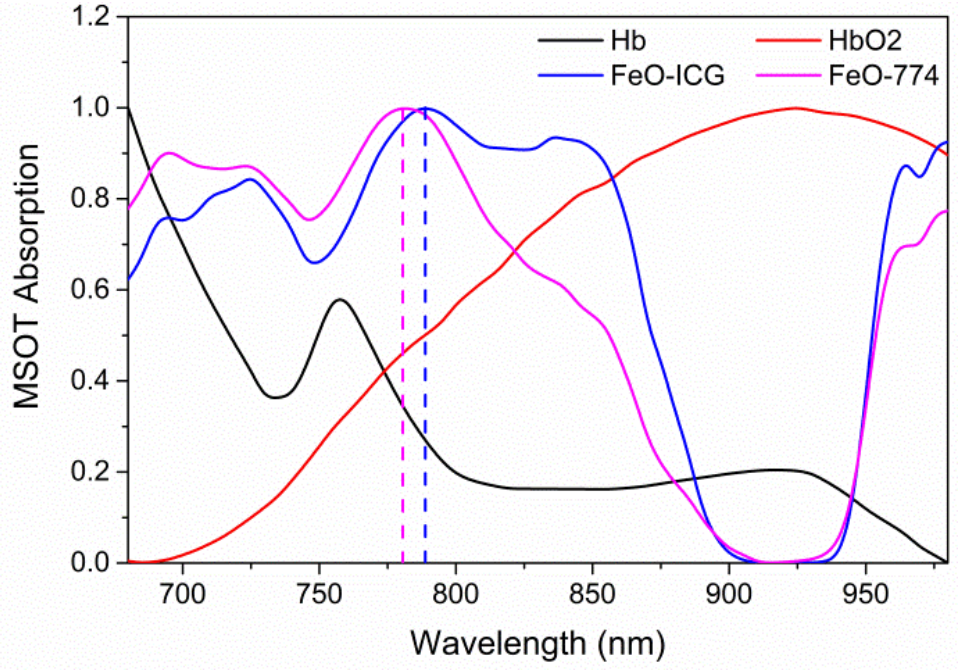

Figure 4.11. Photoacoustic absorption spectra for FeOx-ICG and FeOx-774 along with the contrast with the endogenous contrast agents oxy (HbO_2) and deoxy-hemoglobin (Hb). The normalised MSOT absorption peaks at 780 nm for FeOx-774 and 790 nm for FeOx-ICG. Variation in the peak wavelengths absorbance makes spectral un-mixing possible.

Multi-spectral processing of the photoacoustic absorption spectra over concentration shows the average MSOT signal acquired from FeOx-PA particles. The trend, shown in Figure 4.12, shows the signal obtained at increasing concentrations. As concentration increases, so too does the MSOT signal, reaching saturation at ~100 mM [FeOx]. The signal for both FeOx-ICG and FeOx-774 shows comparable intensity and the linear fit of the concentration curve shows similar absorption profiles. This demonstrates that FeOx-ICG and FeOx-774 are both effective and suitable MSOT probes, even at low concentrations

<100 mM [FeOx]. However, the gradient of the linear fit is greater for the absorption of FeOx-774. Figure 4.12 shows a steeper gradient of $32x10^{-3}$ for FeOx-774 compared to $25x10^{-3}$ for FeOx-ICG. Thus allowing us to show that FeOx-774 is the better MSOT probe with higher PA efficiency.

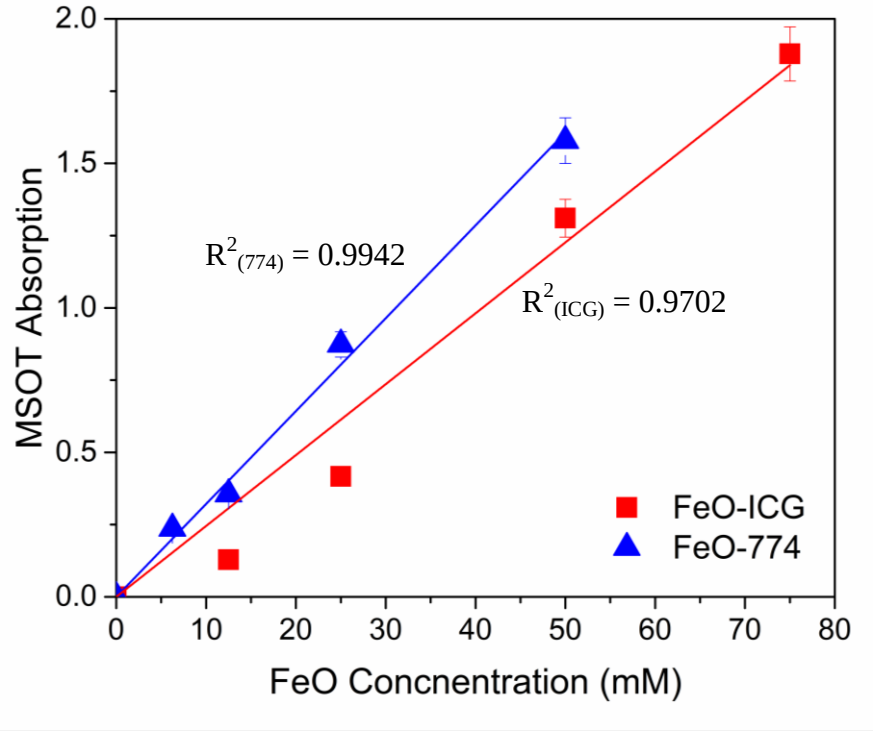

Figure 4.12. Concentration gradient with respect to multispectral optoacoustic (MSOT) intensity and linear fit for the MRI-MSOT probe nanoparticles FeOx-ICG and FeOx-774

4.3.3.3 Magnetic resonance imaging

For a complete multimodal probe, the nanoparticles must also exhibit a contrast for MRI. For this a concentration gradient in a phantom study was achieved in a 7-Tesla Bruker Clinscan MRI system. This shows the level of T2 relaxation caused from the iron oxide core from the equation:

$$M_{xy}(t) = M_{xy}(0)e^{-t/T2} \tag{4.1}$$

Where, $M_{xy}(t)$, is the nuclear spin magnetization vector and, *t*, is the time. This is easily extracted form an exponential fit of the relaxation curves. The scan was performed over increasing scan lengths from t_1, 17.9 ms, to t_{14}, 250.6 ms. Furthermore, the spin relaxivity;

$$R2 = {}^{1}/_{T_2} \tag{4.2}$$

which shows the degree to the T_2-weighted contrast of the MRI image and a linear plot of *R2* vs [Fe] (the concentration of the magnetic atoms) gives the relaxivity coefficient, *r2*, *via* the gradient.[118]

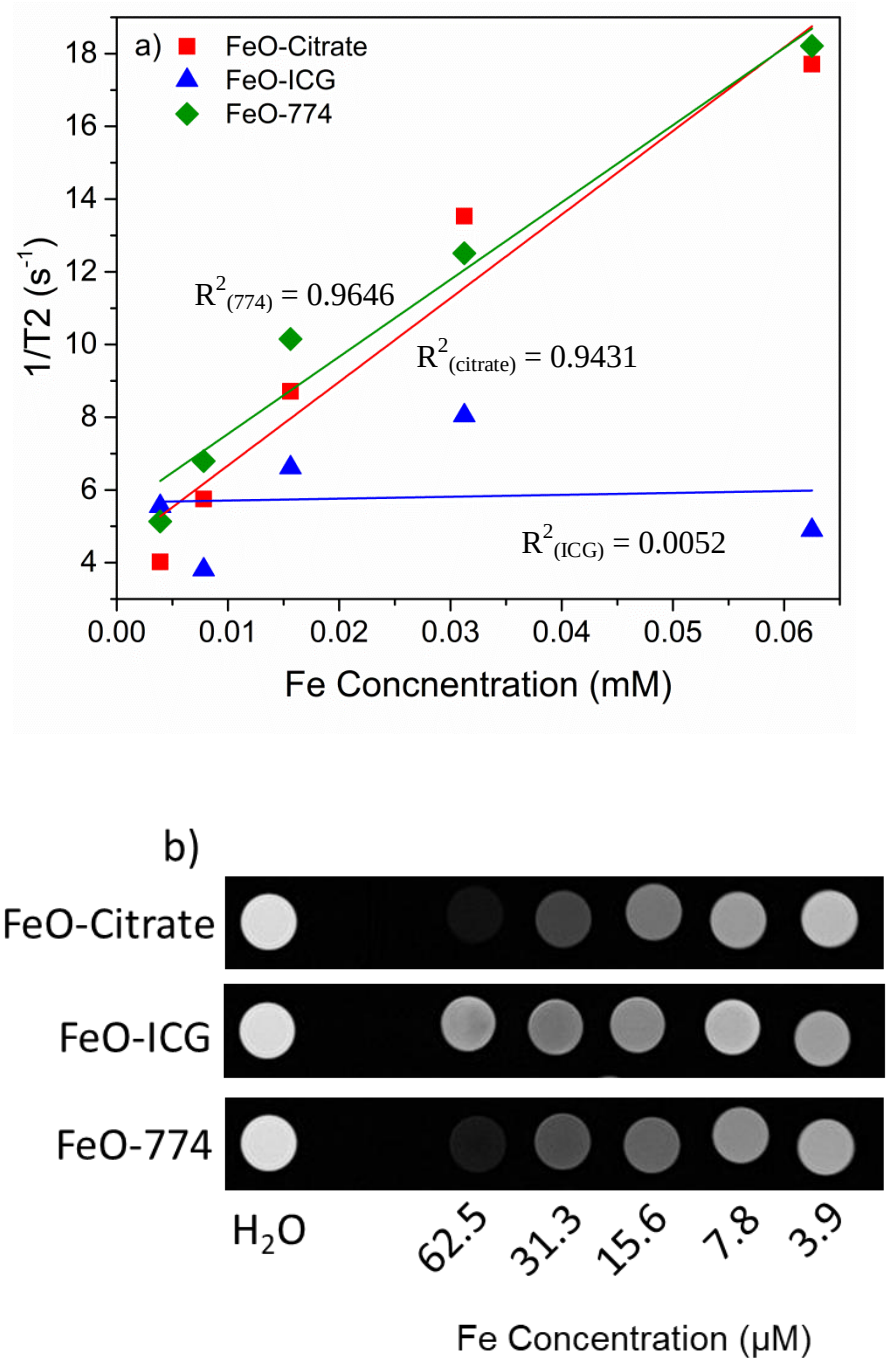

Figure 4.13. Plot of $^{1}/_{T2}$ against [Fe] concentration and b) visual representation of the concentration dependent T_2-weighted MRI contrast for FeOx-citrate, FeOx-774, and FeOx-ICG. The positive linear trend gives the *R2* relaxivity values for the nanoparticle materials. Included is the background of H_2O to show the intensity of the contrast.

From the gradient of the plots in Figure 4.13, the spin echo relaxivity, *r2*, is shown to be 230 $mM^{-1}s^{-1}$ for FeOx-citrate, 212 $mM^{-1}s^{-1}$ for FeOx-774 and only 5.2 $mM^{-1}s^{-1}$ for FeOx-ICG. There has been little effect on the addition of Flamma®774 on the relaxivity of the nanoparticles. Whereas, ICG has shown a large decrease in *R2*, showing nearly negligible contrast in MRI, and a poor linear fit (R^2 = 0.006). Even at higher concentrations of FeOx-ICG there is still no definitive MRI *r2* relaxivity coefficient seen.

Compare the *r2* values to one industry standard and commercially viable iron oxide T_2 contrast agent, Resovist, which has an *r2* relaxivity coefficient of 151 $mM^{-1}sec^{-1}$.

One probable cause for this discrepancy with FeOx-ICG is thought to be due to the stabilisation and dispersion of the magnetic nanoparticle cores.[182] As stated previously (Table 4.1), FeOx-ICG has a hydrodynamic radius of 311 nm, which is up to a three-fold increase in hydrodynamic diameter. FeOx-citrate and FeOx-774 are shown to have φ_H of 108 nm and 146 nm respectively. For comparison, the hydrodynamic radius of Resovist is reported as 45 – 60 nm. This is a factor of two smaller than that of FeOx-citrate and FeOx-774 nanoparticles and a factor of 4 smaller than Fe-ICG. Furthermore, indocyanine green is not a large stabilising molecule or high molecular weight organic polymer. Therefore the resultant φ_H is due to the aggregation of the negatively charged FeOx cores and not the ligand dispersion around the core. The TEM images (Figure 4.9) also shows that the

aggregation of the FeOx-ICG nanoparticles is greater. The images show much larger clusters of particles compared to those of FeOx-citrate and FeOx-774.

This shows that aggregation of the particles can play a large role in the contrast of MRI agents. For a contrast agent to work, H_2O molecules must be present as MRI measures the effect the exogenous contrast has on the proton spins of water. Well-dispersed particles like those coated in citrate or the polymer-based iron oxide particles in the literature have a high contrast and relaxivity coefficient as there is a greater surface area of nanoparticle in contact with surrounding H_2O. Therefore, development into the stabilisation and encapsulation of the photoacoustically active iron oxide through organic and bio-polymer chemistry is currently being investigated to further increase the dispersion coefficients and hopefully improve *r2* values.

4.3.3.4 In-vivo imaging

To determine if the multimodality of the FeOx-PA nanoparticles is translatable to animal models and real world biological systems, *in-vivo* analysis was performed. This was achieved using the mouse model. Nanoparticle delivery was achieved with an intratumoral injection of the nanoparticle sample at 100mM FeOx concentration in a saline solution and scanned 15 minutes post injection. FeOx-774 nanoparticles were analysed *in-vivo* as FeOx-774 provided both the highest photoacoustic signal output and the greatest MRI t2 contrast when compared to the FeOx-ICG nanoparticles. Due to the disparity between the relatively low concentration of Flamma®774 on the surface of the nanoparticles compared to the

FeOx in the core, the MRI was a much more sensitive imaging technique. This means that the concentration of nanoparticles needed for the MSOT was far higher than that for MRI. For this a 100 mM aqueous solution of FeOx-774 was injected once for both scans of MSOT and MRI producing high signal and high contrast images.

MSOT images are shown in Figure 4.14 and show the pre-scan where there is some negligible background signal form the FeOx-774 wavelength. This is expected as the FeOx-774 spectra (see Figure 4.11) has multiple minor peaks which do partially overlap with the endogenous contrast agents Hb and HbO_2. Upon intratumoral injection, spectral unmixing of the MSOT signal isolated the exogenous FeOx-774 optical contrast agent from the endogenous spectra. It can be seen that the signal intensity of the spectrally unmixed MSOT spectra is greatly increased at the tumour site on the right flank of the mouse due to the increased presence of FeOx-774 nanoparticles. The retention time for the nanoparticles in the tumour is high due to the method of introduction of the contrast agent.

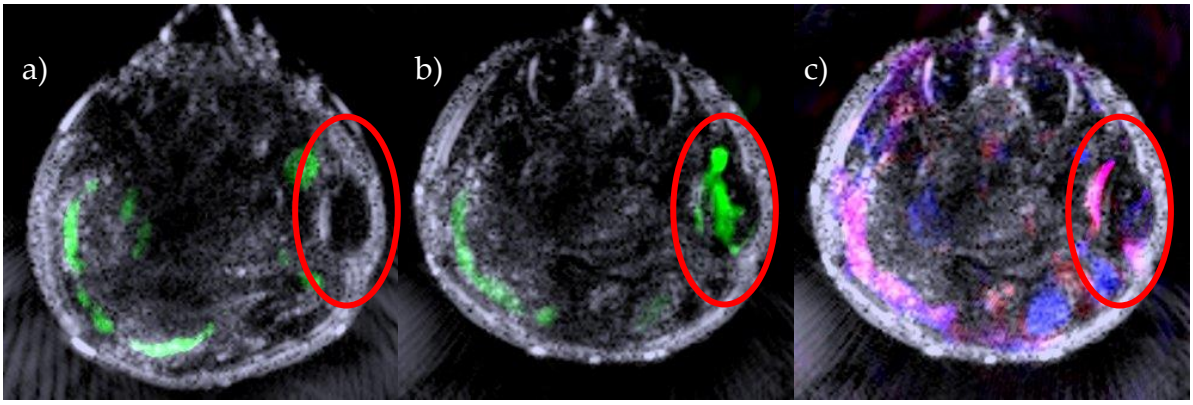

Figure 4.14. Multispectral optoacoustic images of a mouse tumour model (tumour highlighted within the oval) showing the exogenous signal of FeOx-774 (green) at a) the pre-scan of the tumour prior to injection and b) the 15 minute post-injection scan after FeOx-774 intra-tumour injection showing the high photoacoustic signal localisation of the FeOx-774 nanoparticles in the tumour. For comparison, c) shows the endogenous contrast agents (Hb – blue, and HbO_2 – red) 15 minutes post-injection of FeOx-774.

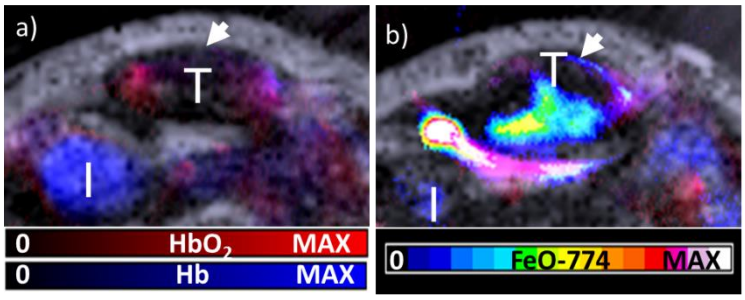

Figure 4.15. Detailed images of a) Oxy- and deoxy-haemoglobin maps overlaid on ultrasound images of U87MG tumor (T indicated by white arrow) implanted subcutaneously in NcR nude mouse obtained before contrast agent administration and b) after injection of FeOx-774 nanoparticles. Where MAX represents total saturation of signal.

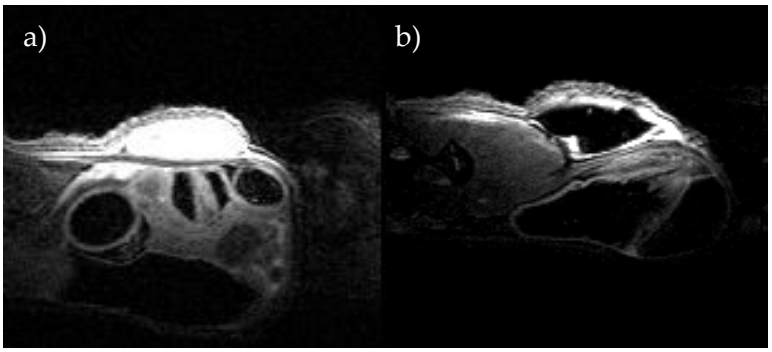

Figure 4.16. MRI images for a) pre-scan and b) 15 mins post injection showing the increase in t2 contrast within the tumour from the presence of FeOx-774 nanoparticles.

Following the MSOT scan the mouse model was transferred, without further injection, to acquire MRI images (Figure 4.16) and it shows that the addition of FeOx-774 nanoparticles leads to a strong t2 contrast with the pre-scan tumour (white region) becoming negatively contrasted upon addition of FeOx-774 nanoparticles. This is expected due to the well-known nature of FeOx nanoparticles being a strong T_2 contrast agent, and this demonstrates that the nanoparticles are still stable in the mouse model and do not aggregate and lose MRI contrast

Many multi-modal FeOx imaging probes currently in literature use multi-step hydrothermal synthesis procedures of complex multi-phase structures held within polymer surfactants.[183–187] Many of which are designed for MRI and, CT or PET imaging. Hyaluronic acid coated of multi-core FeO-Au nanoparticles is one example by Li *et. al.*[188] This nanoconstruct gives tri-modal imaging of MR-CT-

PDT using a functionalised Fe *via* a 7 step synthetic method. This also gives good T_2 contrast at 144 $mM^{-1}s^{-1}$.

The particles presented in this thesis more closely resemble Janus/dumbbell style nanomaterials currently in literature. Reguera *et. al.* have shown how such shaped particles are suitable for all manner of imaging techniques including CT, MRI, PA and SERS.[189] This synthesis can be seen a great advantage to nanoprobe development due its simplicity and high reproducibility.

4.4 CONCLUSION

This chapter therefore shows how we have created a facile way to make a multimodal MRI–MSOT nanoparticle probe using a novel surface attachment chemistry of a PA dye onto the surface of iron oxide nanoparticles. Initial synthesis of chlorin e6-coated iron oxide nanoparticles showed that the chemistry can successfully coordinate a PA dye onto the metallic surface through a condensation reaction.

The subsequent nanoparticles we report on show an enhanced photoacoustic signal form the presence of the PA dye, ICG or Flamma®774, With FeOx-774 showing the highest MSOT efficiency. The obtained photoacoustic spectra exhibit a clear peak in the Near-IR wavelength region of 790 and 780 nm for FeOx-ICG and FeOx-774 respectively. This makes spectral unmixing of FeOx-PA nanoparticles and the endogenous contrast Hb and HbO_2 possible.

Furthermore, we have demonstrated that FeOx-774 displays good MRI *r2* contrast of 212 $mM^{-1}s^{-1}$, which is similar to the citrate coated FeOx-citrate *r2* relaxivity coefficient of 230 $mM^{-1}s^{-1}$. This shows that PA dye functionalisation has little to no effect on the MRI properties of FeOx nanoparticles. However, FeOx-ICG does show vastly reduced contrast, at 5 $mM^{-1}s^{-1}$. This can be attributed to the surface stabilisation produced *via* ICG molecules. TEM and DLS analysis showed much greater aggregation and clustering compared to FeOx nanoparticles coated with citrate or Flamma®774 conjugation. Aggregation is important for imaging nanoparticles due to the mechanism of MRI because MRI uses a measure of the magnetic spin of protons in H_2O. When the FeOx nanoparticles are large clusters there is less water present, resulting in few adjacent protons to enhance the contrast of the image and therefore a weak signal.

In-vivo analysis also demonstrated how the nanoparticles can be used for spectral un-mixing of the nanoparticle absorption wavelengths and the endogenous contrast agents using MSOT. Furthermore, the nanoparticles showed high MRI contrast due to the good hydrodynamic dispersity and stability of the iron oxide cores. This also showed that FeOx-774 nanoparticles are stable in biological systems and the MRI or MSOT signals were not quenched.

This can be seen as a critical development in the understanding of multimodal imaging probes, showing that there are facile methods for the synthesis of a feasible nano-probe combining both MRI and MSOT. Importunately, it is good to note that these particles are also of the same design of those in Chapter 2, where magnetic hyperthermia was investigated. In theory, these multimodal particles will also possess a hyperthermic response when under an external magnetic field.

This both open up the possibility for a multi-functional particle that can both image (with two modalities) and also treat the region of interest.

Interestingly, with regards to the heating of the nanoparticles though magnetic hyperthermia, this will have an effect on the photoacoustic properties. As stated with the Grüneisen parameter, changes in local environmental factors, such as temperature, will affect the photoacoustic effect of the material. How the heating of the particles will modify the potential multimodal nature of these particles is yet to be investigated.

5 CONCLUSION

5.1 CLOSING REMARKS

In conclusion, this thesis has explored the synthetic methods and use of iron oxide nanoparticles in a wide range of applications; from magnetic hyperthermia therapy to multimodal sensing/imaging probes.

Initial synthesis involved a co-precipitation technique for iron oxide nanoparticles, using the different stabilising ligands of citric acid or tiopronin. Highly spherical and monodisperse nanoparticles were produced but coalescence of the individual cores was troubling. The stabilising ligands were for the purpose of improving the colloidal stability of the particles and analysing their effect on the heating achieved through magnetic hyperthermia. Temperature profiles were gathered showing that citrate stabilised iron oxide nanoparticles were more effective at heating, furthermore, citrate-stabilising ligands can be advantageous towards further functionalisation. This further functionalisation came from the post-production addition of gold onto the iron oxide surface through a modification of the Turkevich citrate boiling gold colloid synthesis. The main reason for this addition was two-fold; firstly gold may improve bio-stability and protect the iron oxide, while secondly, giving a superior anchor point for any polymer or peptide binding through thiol's affinity towards gold. Unfortunately, but not unexpectedly, the gold addition did not evenly coat the iron oxide nanoparticles. Microscopy showed that gold nanoparticles were forming within the iron oxide

superstructure, and at different sizes dependant on the concentration of gold added. Interestingly, it developed that this was highly beneficial towards heat generation *via* magnetic hyperthermia resulting in almost a 3-fold increase in intrinsic loss power. As of yet the mechanism for this is still unsure, however there could be interference between the interfaces of the different phases.

These iron oxide – gold nanocomposite materials were shown to have a combination of multiple beneficial physiological properties. The high levels of paramagnetism from the iron oxide and specific optical SPR bands from the small amounts of gold. Importantly after repeated synthesis and analysis of these materials it was determined that this synthetic method was widely reproducible. This is aided by the factor of a simple co-precipitation mechanism with few complex steps and mild reaction conditions. This is co-precipitation mechanism is advantageous over the other commonly used hydrothermal synthesis in most regards in my opinion. The only disadvantage being a relative lack of monodisperse nanoparticles for a co-precipitation reaction compared to the hydrothermal.

Multi-modal imaging was therefore always a possible avenue to explore. Firstly, SERS spectroscopy was analysed to see if the nanocomposite gave strong Raman enhancement. FeOx-Au was therefore compared to gold nanospheres and gold nanostars. The gold nanoparticles were synthesised, in a similar method to the post-production of FeOx with Au, by the common Turkevich synthesis. Au stars were synthesised using a reduction method utilising silver nitrate as a seeding agent. Gold nanostructures have been well described to be ideal SERS substrates and these synthesised particles proved no difference. Gold nanostars proved to be

the most effective when dried to a silica substrate. Likewise the iron oxide – gold nanocomposite achieved SERS enhancement when dried under vacuum on a silica substrate, however not when in solution. This is attributed to the displacement and dispersity of any gold nanoparticles throughout the iron oxide, i.e. few gold nanoparticles are in close proximity to each other. This results in poor localised SPR bands throughout the whole solution. I think that this has the potential to be impactful within bio-imaging, due to the ability to actively recover the sensing medium. Using an external magnet, it would be possible to recycle and reuse any such Raman probe after suitable cleansing. This would make a magnetic SERS particle highly desirable in a scientific, economic and environmental aspect.

Further multi-modality of iron oxide nanoparticles was achieved by pairing the magnetic cores with a photoacoustically active dye. Synthesis of this was carried out in a novel condensation esterification reaction between the FeOx cores and either C e6, ICG or Flamma®774 dyes. This synthetic route used bare nanoparticle cores and dyes possessing an activated carboxyl group. Activation was achieved with Sulfo-NHS in an MES buffer to lower the energy required to successfully covalently bind the dye to the surface Fe-OH of the nanoparticle.

MSOT analysis of the new photoacoustic iron oxide nanoparticles showed that photoacoustic activity was present in all probes. Depending on the absorption profiles however, it showed that FeOx-Ce6 would not be visible *in-vivo* due to the similar PA profile of Hb. ICG and Flamma®774 both have more suitable absorption wavelengths between the peaks of Hb and HbO_2 making them ideal conjugators.

To test the full abilities of this iron oxide – PA dye multi-modal probe, MRI was obtained and showed the high T_2 contrast common with FeO nanoparticles. Interestingly, it was seen that FeO-ICG failed to have contrast even after being synthesised from the same iron oxide cores. This was attributed to the greater aggregation seen when the iron oxide nanoparticles were stabilised/coated with ICG. Therefore, it is clear to see that the ideal MRI-MSOT multi-modal probe synthesised here is that of FeO-774. The development of this multi-modal imaging probe is highly impactful due to the ability to gather data for two differing techniques with one nanoparticle solution.

5.2 OUTLOOK

The potential for magnetic hyperthermia as being one of the next processes in the fight against cancer, tumours and bacteria is still high. Tailoring magnetic nanoparticles to be efficient and powerful hyperthermia agents is important for the therapeutics and clinicians. This means that further research into more responsive and stable nanoparticles is necessary. For this, different ligands can be trialled in a comparative way to those of citric acid and tiopronin. These could include many biostable compounds and polymers such as dextran, oleic acid and etidronic acid. Furthermore, the iron oxide – gold nanocomposites are of great interest due to their improved hyperthermia characteristics and potential biocompatibility. This can lead to functionalization of the gold, resulting in selectively binding hyperthermia agents. In addition, biological studies will be carried out to

determine the overall effectiveness of these particles on cancerous cells and bacteria.

However, it would be important to gather more analysis of the iron oxide – gold nanoparticles. SQUID (superconducting quantum interference device) is of great interest and will give detailed ***H*** plot analysis on the magnetisation of the particles, which could provide insight into the mechanisms surrounding the increase in ILP from gold addition.

In this potentially very interesting SERS research, the outlook is towards further refinement of the nanoparticle analytes. As is shown, gold nanostars are an effective SERS agent however the synthesis still leaves much to be desired. The synthesis of highly controlled and repeatable gold nanostars is still seen as a challenge and that of key importance for the creation of a reliable and accurate SERS sensor. There are also other varied gold nanoparticle morphologies that could make useful SERS sensors.

Furthermore, the synthesis of iron oxide – gold nanoparticles can be enhanced. The formation of a uniformly coated iron oxide core is of difficulty and requires more investigation. This has the potential to lead to the development of several easy to make multimodal sensing and imaging techniques, such as a magnetic resonance – photoacoustic – Raman (MR-PA-SERS) probe. It is also important to further investigate the spectra obtained from the iron oxide – gold nanocomposite material. The Raman spectrum contains many peaks not associated with the dye MGICT or the nanoparticles.

From the MRI-MSOT analysis we have determined that FeOx-774 is the best iron oxide core based MSOT-MRI probe that we have developed using a facile and simple chemical synthesis. However, this chemical synthesis can be easily altered with a variety of other suitable chromofluors making development of new magnetic PA probes possible. Together with further refinement of the nanoparticle structures which is still necessary, with stabilization and aggregation being key areas of development in the progression to make an ideal MSOT-MRI photoacoustic probe. Development into a specific targeting probe is of high interest and impact for clinical studies for where an intravenous administration of the contrast is more desired.

It would also be of great interest to investigate the potential of combining the three techniques I have analysed these magnetic nanoparticles for. As the nanoparticles used for the bio-imaging were of the same characteristics and synthetic method of those used for thermotherapy, it would be possible to have a imaging probe combined with therapeutics. However the surface ligands of the iron oxide will have significant effects on the magnetic heating so this would need to be studied. Furthermore, the heat generated from the magnetic hyperthermia can have knock-on effects for the generation of photoacoustics as it is fundamentally a thermally induced phenomenon.

REFERENCES

[1] A. D. McNaught, A. Wilkinson, *IUPAC. Compendium of Chemical Terminology*, Blackwell Scientific Publications, Oxford, **1997**.

[2] W. Haiss, N. T. K. Thanh, J. Aveyard, D. G. Fernig, *Anal. Chem.* **2007**, *79*, 4215–21.

[3] A. Albanese, P. S. Tang, W. C. W. W. Chan, *Annu. Rev. Biomed. Eng.* **2012**, *14*, 1–16.

[4] A. C. Balazs, T. Emrick, T. P. Russell, *Science* **2006**, *314*, 1107–1110.

[5] Q. A. Pankhurst, J. Connolly, S. K. Jones, J. Dobson, *J. Phys. D. Appl. Phys.* **2003**, *167*, R167–R181.

[6] Q. A. Pankhurst, N. Thanh, S. Jones, J. Dobson, *J. Phys. D. Appl. Phys.* **2009**, *224001*.

[7] Z. Liu, L. M. Gan, L. Hong, W. Chen, J. Y. Lee, *J. Power Sources* **2005**, *139*, 73–78.

[8] Y.-C. Chang, D.-H. Chen, *J. Hazard. Mater.* **2009**, *165*, 664–9.

[9] L. Thomas, L. Dekker, M. Kallumadil, P. Southern, M. Wilson, S. Nair, Q. Pankhurst, I. Parkin, *J. Mater. Chem.* **2009**, *19*, 6529–6535.

[10] R. Y. Hong, B. Feng, L. L. Chen, G. H. Liu, H. Z. Li, Y. Zheng, D. G. Wei, *Biochem. Eng. J.* **2008**, *42*, 290–300.

[11] B. Feng, R. Y. Y. Hong, L. S. S. Wang, L. Guo, H. Z. Z. Li, J. Ding, Y. Zheng, D. G. G. Wei, *Colloids Surfaces A Physicochem. Eng. Asp.* **2008**, *328*, 52–59.

[12] T. K. Jain, M. a. Morales, S. K. Sahoo, D. L. Leslie-Pelecky, V. Labhasetwar, *Mol. Pharm.* **2005**, *2*, 194–205.

[13] L. Li, K. Y. Mak, C. W. Leung, C. H. Leung, a. Ruotolo, K. Y. Chan, W. K. Chan, P. W. T. Pong, *IEEE Trans. Magn.* **2014**, *50*, DOI 10.1109/TMAG.2013.2274457.

[14] H. L. Ding, Y. X. Zhang, S. Wang, J. M. Xu, S. C. Xu, G. H. Li, *Chem. Mater.* **2012**, *24*, 4572–4580.

[15] I. W. Hamley, *Angew. Chem. Int. Ed. Engl.* **2003**, *42*, 1692–712.

[16] A. K. Gupta, M. Gupta, *Biomaterials* **2005**, *26*, 3995–4021.

[17] R. Grau-Crespo, A. Y. Al-Baitai, I. Saadoune, N. H. De Leeuw, *J. Phys. Condens. Matter* **2010**, *22*, 255401.

[18] W. Wu, Q. He, C. Jiang, *Nanoscale Res. Lett.* **2008**, *3*, 397–415.

[19] K. T. Wu, P. C. Kuo, Y. D. Yao, E. H. Tsai, *IEEE Trans. Magn.* **2001**, *37*, 2651–2653.

[20] Y. Lee, J. Lee, C. J. Bae, J.-G. Park, H.-J. Noh, J.-H. Park, T. Hyeon, *Adv. Funct. Mater.* **2005**, *15*, 503–509.

[21] J. Zhi, Y. Wang, Y. Lu, J. Ma, G. Luo, *React. Funct. Polym.* **2006**, *66*, 1552–1558.

[22] T. J. Daou, G. Pourroy, S. Bégin-Colin, J. M. Grenèche, C. Ulhaq-Bouillet, P. Legaré, P. Bernhardt, C. Leuvrey, G. Rogez, *Chem. Mater.* **2006**, *18*, 4399–4404.

[23] C. Blanco-Andujar, D. Ortega, P. Southern, Q. A. Pankhurst, N. T. K. Thanh, *Nanoscale* **2015**, *7*, 1768–75.

[24] N. T. K. Thanh, N. Maclean, S. Mahiddine, *Chem. Rev.* **2014**, *114*, 7610–30.

[25] P. W. Voorhees, *J. Stat. Phys.* **1985**, *38*, 231–252.

[26] I. M. Lifshitz, V. V. Slyozov, *J. Phys. Chem. Solids* **1961**, *19*, 35–50.

[27] M. Jaiswal, R. Dudhe, P. K. Sharma, *3 Biotech* **2015**, *5*, 123–127.

[28] J. R. Sosa-Acosta, J. A. Silva, L. Fernández-Izquierdo, S. Díaz-Castañón, M. Ortiz, J. C. Zuaznabar-Gardona, A. M. Díaz-García, *Colloids Surfaces A Physicochem. Eng. Asp.* **2018**, *545*, 167–178.

[29] P. Nehra, R. P. Chauhan, N. Garg, K. Verma, *Br. J. Biomed. Sci.* **2018**, *75*, 13–18.

[30] J. S. Basuki, A. Jacquemin, L. Esser, Y. Li, C. Boyer, T. P. Davis, *Polym. Chem.* **2014**, *5*, 2611–2620.

[31] J. Lodhia, G. Mandarano, N. J. Ferris, P. Eu, S. F. Cowell, *Biomed. Imaging Interv. J.* **2010**, *6*, DOI 10.2349/biij.6.2.e12.

[32] J.-P. Jolivet, C. Chanéac, E. Tronc, *Chem. Commun. (Camb).* **2004**, 481–7.

[33] S. Laurent, D. Forge, M. Port, A. Roch, C. Robic, L. V Elst, R. N. Muller, *Chem. Rev.* **2008**, *108*, 2064–2110.

[34] J. Park, K. An, Y. Hwang, J.-G. Park, H.-J. Noh, J.-Y. Kim, J.-H. Park, N.-M. Hwang, T. Hyeon, *Nat. Mater.* **2004**, *3*, 891–895.

[35] Y. Tian, B. Yu, X. Li, K. Li, *J. Mater. Chem.* **2011**, *21*, 2476.

[36] S. Ge, X. Shi, K. Sun, C. Li, J. R. Baker, M. M. Banaszak Holl, B. G. Orr, *J. Phys. Chem. C. Nanomater. Interfaces* **2009**, *113*, 13593–13599.

[37] J. Li, Y. He, W. Sun, Y. Luo, H. Cai, Y. Pan, M. Shen, J. Xia, X. Shi, *Biomaterials* **2014**, *35*, 3666–3677.

[38] H. Cai, X. An, J. Cui, J. Li, S. Wen, K. Li, M. Shen, L. Zheng, G. Zhang, X. Shi, *ACS Appl. Mater. Interfaces* **2013**, *5*, 1722–1731.

[39] D. Naor, S. Nedvetzki, I. Golan, L. Melnik, Y. Faitelson, *Crit. Rev. Clin.*

Lab. Sci. **2002**, *39*, 527–579.

[40] C. Blanco-Andujar, D. Ortega, P. Southern, Q. A. Pankhurst, N. T. K. Thanh, *Nanoscale* **2015**, *7*, 1768–1775.

[41] X. Hu, J. C. Yu, J. Gong, Q. Li, G. Li, *Adv. Mater.* **2007**, *19*, 2324–2329.

[42] Z. L. Liu, Y. J. Liu, K. L. Yao, Z. H. Ding, J. Tao, X. Wang, **2002**, *10*, 83–87.

[43] W. Wu, Z. Wu, T. Yu, C. Jiang, W. S. Kim, *Sci. Technol. Adv. Mater.* **2015**, *16*, DOI 10.1088/1468-6996/16/2/023501.

[44] S. Laurent, D. Forge, M. Port, a Roch, C. Robic, L. V Elst, R. N. Muller, *Chem. Rev.* **2008**, *108*, 2064–2110.

[45] J. Turkevich, P. C. Stevenson, J. Hillier, *Discuss. Faraday Soc.* **1951**, *11*, 55–75.

[46] Y. Sahoo, H. Pizem, T. Fried, D. Golodnitsky, L. Burstein, C. N. Sukenik, G. Markovich, *Langmuir* **2001**, *17*, 7907–7911.

[47] Y. Sahoo, A. Goodarzi, M. T. Swihart, T. Y. Ohulchanskyy, N. Kaur, E. P. Furlani, P. N. Prasad, *J. Phys. Chem. B* **2005**, *109*, 3879–3885.

[48] H. Lee, E. Lee, D. K. Kim, N. K. Jang, Y. Y. Jeong, S. Jon, *J. Am. Chem. Soc.* **2006**, *128*, 7383–7389.

[49] E. S. Jang, S. Y. Lee, E. J. Cha, I. C. Sun, I. C. Kwon, D. Kim, Y. Il Kim, K. Kim, C. H. Ahn, *Pharm. Res.* **2014**, *31*, 3371–3378.

[50] J. L. Lyon, D. a. Fleming, M. B. Stone, P. Schiffer, M. E. Williams, *Nano Lett.* **2004**, *4*, 719–723.

[51] H. Yu, M. Chen, P. M. Rice, S. X. Wang, R. L. White, S. Sun, *Nano Lett.* **2005**, *5*, 379–382.

[52] C. Xu, B. Wang, S. Sun, *J. Am. Chem. Soc.* **2009**, *27*, 339–351.

[53] A. M. Helmenstine, “Tyndall Effect Definition and Examples,” can be found under thoughtco.com/definition-of-tyndall-effect-605756., **2017**.

[54] P. Pattnaik, *Appl. Biochem. Biotechnol.* **2005**, *126*, 79–92.

[55] J. Homola, S. S. Yee, G. Gauglitz, *Sensors Actuators B Chem.* **1999**, *54*, 3–15.

[56] R. Karlsson, *J. Mol. Recognit.* **2004**, *17*, 151–161.

[57] W. Li, X. Chen, *Nanomedicine (Lond).* **2015**, *10*, 299–320.

[58] U. S. Dinish, Z. Song, C. J. H. Ho, G. Balasundaram, A. B. E. Attia, X. Lu, B. Z. Tang, B. Liu, M. Olivo, *Adv. Funct. Mater.* **2015**, *25*, 2316–2325.

[59] T. A. El-Brolossy, T. Abdallah, M. B. Mohamed, S. Abdallah, K. Easawi, S. Negm, H. Talaat, *Eur. Phys. J. Spec. Top.* **2008**, *153*, 361–364.

[60] C. S. Ah, Y. J. Yun, H. J. Park, W. J. Kim, D. H. Ha, W. S. Yun, *Chem. Mater.* **2005**, *17*, 5558–5561.

[61] K. S. Lee, M. A. El-Sayed, *J. Phys. Chem. B* **2005**, *109*, 20331–20338.

[62] J. He, X. Huang, Y. C. Li, Y. Liu, T. Babu, M. A. Aronova, S. Wang, Z. Lu, X. Chen, Z. Nie, *J. Am. Chem. Soc.* **2013**, *135*, 7974–7984.

[63] A. M. Smith, M. C. Mancini, S. Nie, *Nat. Nanotechnol.* **2010**, *4*, 710–711.

[64] D. C. Hone, P. I. Walker, R. Evans-Gowing, S. FitzGerald, A. Beeby, I. Chambrier, M. J. Cook, D. A. Russell, *Langmuir* **2002**, *18*, 2985–2987.

[65] A. Srivatsan, S. V. Jenkins, M. Jeon, Z. Wu, C. Kim, J. Chen, R. K. Pandey, *Theranostics* **2014**, *4*, 163–174.

[66] H. Häkkinen, *Nat. Chem.* **2012**, *4*, 443–455.

[67] T. Niidome, M. Yamagata, Y. Okamoto, Y. Akiyama, H. Takahashi, T. Kawano, Y. Katayama, Y. Niidome, *J. Control. Release* **2006**, *114*, 343–347.

[68] X. Qian, X. H. Peng, D. O. Ansari, Q. Yin-Goen, G. Z. Chen, D. M. Shin, L. Yang, A. N. Young, M. D. Wang, S. Nie, *Nat. Biotechnol.* **2008**, *26*, 83–90.

[69] P. Ghosh, G. Han, M. De, C. K. Kim, V. M. Rotello, *Adv. Drug Deliv. Rev.* **2008**, *60*, 1307–1315.

[70] J. Turkevich, P. C. Stevenson, J. Hiller, *Discuss. Faraday Soc.* **1951**, *11*, 55–75.

[71] S. Zeng, K.-T. Yong, I. Roy, X.-Q. Dinh, X. Yu, F. Luan, *Plasmonics* **2011**, *6*, 491–506.

[72] N. G. Bastús, J. Comenge, V. Puntes, *Langmuir* **2011**, *27*, 11098–11105.

[73] M. Brust, M. Walker, D. Bethell, D. J. Schiffrin, R. Whyman, *J. Chem. Soc. Chem. Commun.* **1994**, 801–802.

[74] P. J. G. Goulet, R. B. Lennox, *J. Am. Chem. Soc.* **2010**, *132*, 9582–9584.

[75] A. H. Morrish, *The Physical Principles of Magnetism*, IEEE, New York, **2001**.

[76] Y. Liu, D. J. Sellmyer, D. Shindo, *Handbook of Advanced Magnetic Materials*, Springer Publishing, New York, **2006**.

[77] P. Atkins, J. De Paula, *Atkins' Physical Chemistry*, Oxford University Press, Oxford, **2010**.

[78] H. Maeda, Y. Yanagisawa, *IEEE Trans. Appl. Supercond.* **2014**, *24*, DOI 10.1109/TASC.2013.2287707.

[79] E. H. Brandt, *Appl. Phys. Lett.* **1988**, *53*, 1554–1556.

[80] S. Sun, *Science (80-.).* **2000**, *287*, 1989–1992.

[81] W. T. Coffey, Y. P. Kalmykov, *J. Appl. Phys.* **2012**, *121301*, 1–99.

[82] K. Mahmoudi, C. G. Hadjipanayis, **2014**, *2*, 1–5.

[83] S. Laurent, S. Dutz, U. O. Häfeli, M. Mahmoudi, *Adv. Colloid Interface Sci.* **2011**, *166*, 8–23.

[84] W. F. Brown, *Phys. Rev.* **1963**, *130*, 1677–1686.

[85] W. Wernsdorfer, E. Orozco, K. Hasselbach, a. Benoit, B. Barbara, N. Demoncy, a. Loiseau, H. Pascard, D. Mailly, *Phys. Rev. Lett.* **1997**, *78*, 1791–1794.

[86] A. Jordan, R. Scholz, P. Wust, H. Fähling, Roland Felix, *J. Magn. Magn. Mater.* **1999**, *201*, 413–419.

[87] N. T. K. Thanh, A. Hervault, *Nanoscale* **2014**, DOI 10.1039/C4NR03482A.

[88] R. D. Issels, *Eur. J. Cancer* **2008**, *44*, 2546–2554.

[89] R. R. Wildeboer, P. Southern, Q. A. Pankhurst, **2014**, *47*, DOI 10.1088/0022-3727/47/49/495003.

[90] M. Kallumadil, M. Tada, T. Nakagawa, M. Abe, P. Southern, Q. A. Pankhurst, *J. Magn. Magn. Mater.* **2009**, *321*, 1509–1513.

[91] D. Ortega, Q. A. Pankhurst, *Nanoscience* **2012**, *1*, 60–88.

[92] S. Kossatz, R. Ludwig, H. Dähring, V. Ettelt, G. Rimkus, M. Marciello, G. Salas, V. Patel, F. J. Teran, I. Hilger, *Pharm. Res.* **2014**, 3274–3288.

[93] K. Maier-Hauff, F. Ulrich, D. Nestler, H. Niehoff, P. Wust, B. Thiesen, H. Orawa, V. Budach, A. Jordan, *J. Neurooncol.* **2011**, *103*, 317–324.

[94] Z. R. Stephen, F. M. Kievit, O. Veiseh, P. A. Chiarelli, C. Fang, K. Wang, S. J. Hatzinger, R. G. Ellenbogen, J. R. Silber, M. Zhang, et al., **2014**.

[95] V. Ntziachristos, D. Razansky, *Chem. Rev.* **2010**, *110*, 2783–2794.

[96] E. Grüneisen, *Ann. Phys.* **1912**, *344*, 257–306.

[97] S. Tzoumas, A. Nunes, N. C. Deliolanis, V. Ntziachristos, *J. Biophotonics* **2015**, *8*, 629–637.

[98] L. V Wang, *Nat. Photonics* **2009**, *3*, 503–509.

[99] L. Wang, S. Hu, *Science (80-.).* **2012**, *335*, 1458–1462.

[100] Meng-Lin Li, Jung-Taek Oh, Xueyi Xie, Geng Ku, Wei Wang, Chun Li, G. Lungu, G. Stoica, L. V. Wang, *Proc. IEEE* **2008**, *96*, 481–489.

[101] N. Beziere, N. Lozano, A. Nunes, J. Salichs, D. Queiros, K. Kostarelos, V. Ntziachristos, *Biomaterials* **2015**, *37*, 415–424.

[102] C. Zheng, M. Zheng, P. Gong, D. Jia, P. Zhang, B. Shi, Z. Sheng, Y. Ma, L. Cai, *Biomaterials* **2012**, *33*, 5603–5609.

[103] A. B. E. Attia, G. Balasundaram, W. Driessen, V. Ntziachristos, M. Olivo, *Biomed. Opt. Express* **2015**, *6*, 591.

[104] C. J. H. Ho, G. Balasundaram, W. Driessen, R. McLaren, C. L. Wong, U. S. Dinish, A. B. E. Attia, V. Ntziachristos, M. Olivo, *Sci. Rep.* **2014**, *4*, 5342.

[105] S. Link, M. A. El-Sayed, *J. Phys. Chem. B* **1999**, *103*, 8410–8426.

[106] L. Nie, X. Chen, *Chem. Soc. Rev.* **2014**, *43*, 7132–7170.

[107] M. F. Kircher, A. De La Zerda, J. V. Jokerst, C. L. Zavaleta, P. J. Kempen, E. Mittra, K. Pitter, R. Huang, C. Campos, F. Habte, et al., *Nat. Med.* **2012**, *18*, 829–834.

[108] S. C. Bushong, G. Clarke, *Magnetic Resonance Imaging: Physical Aand Biological Principles*, Elsevier, St. Louis, **2015**.

[109] M. Kriege, C. T. M. Brekelmans, C. Boetes, P. E. Besnard, H. M. Zonderland, I. M. Obdeijn, R. A. Manoliu, T. Kok, H. Peterse, M. M. A. Tilanus-Linthorst, et al., *N. Engl. J. Med.* **2004**, *351*, 427–437.

[110] A. Carrillo, J. L. Duerk, J. S. Lewin, D. L. Wilson, *IEEE Trans. Med. Imaging* **2000**, *19*, 175–185.

[111] E. . M. Warner H.; Causer, P.; Eisen, A.; Shumak, R.; Plewes, D., *Ann Intern Med* **2008**, *148*, 671–679.

[112] C. R. Jack Jr., M. M. Shiung, J. L. Gunter, P. C. O'Brien, S. D. Weigand, D. S. Knopman, B. F. Boeve, R. J. Ivnik, G. E. Smith, R. H. Cha, et al., *Neurology*. **2004**, *62*, 591–600.

[113] H. . Adams, H. . Adams, B. . Bendixen, B. . Bendixen, L. . Kappelle, L. . Kappelle, J. Biller, J. Biller, B. . Love, B. . Love, et al., *Stroke* **1993**, *23*, 35–41.

[114] N. Lee, T. Hyeon, *Chem. Soc. Rev.* **2012**, *41*, 2575–2589.

[115] Y.-X. J. Wang, *Quant. Imaging Med. Surg.* **2011**, *1*, 35–40.

[116] H.-J. Weinmann, R. C. Brasch, W.-R. Press, G. E. Wesbey, *Am. J. Roentgenol.* **1983**, *142*, DOI 10.2214/ajr.142.3.619.

[117] P. Caravan, J. J. Ellison, T. J. McMurry, R. B. Lauffer, *Chem. Rev.* **1999**, *99*, 2293–2352.

[118] S. H. Koenig, K. E. Kellar, *Magn. Reson. Med.* **1995**, *34*, 227–233.

[119] N. Lee, D. Yoo, D. Ling, M. H. Cho, T. Hyeon, J. Cheon, *Chem. Rev.* **2015**, *115*, 10637–10689.

[120] J. Jang, H. Nah, J. Lee, S. H. Moon, M. G. Kim, J. Cheon, *Angew. Chem. Int. Ed* **2009**, *4*, 1234–1238.

[121] H. Wei, O. T. Bruns, M. G. Kaul, E. C. Hansen, M. Barch, A. Wiśniowska, O. Chen, Y. Chen, N. Li, S. Okada, et al., *Proc. Natl. Acad. Sci.* **2017**, *114*, 2325–2330.

[122] Y. Jin, C. Jia, S.-W. Huang, M. O'Donnell, X. Gao, *Nat. Commun.* **2011**, *1*, 1–17.

[123] C. V Raman, *Indian J. Phys.* **1928**, *398[1] S.*

[124] K. Kneipp, Y. Wang, H. Kneipp, L. T. Perelman, I. Itzkan, R. R. Dasari, M. S. Feld, *Phys. Rev. Lett.* **1997**, 1667–1670.

[125] E. C. Le Ru, E. Blackie, M. Meyer, P. G. Etchegoin, *J Phys. Chem. C* **2007**, 13794–13803.

[126] Y. Sun, Y. Xia, *Science (80-.).* **2002**, *298*, 2176–2180.

[127] K. W. Kho, Z. X. Shen, H. C. Zeng, K. C. Soo, M. Olivo, *Anal. Chem.* **2005**, *77*, 7462–7471.

[128] H. Chen, L. Zhao, D. Chen, W. Hu, *J. Colloid Interface Sci.* **2015**, *460*, 258–263.

[129] O. Seitz, M. M. Chehimi, E. Cabet-deliry, S. Truong, N. Felidj, C. Perruchot, S. J. Greaves, J. F. Watts, *Colloids Surfaces A Physicochem. Eng. Asp.* **2003**, *218*, 225–239.

[130] S. S. R. Dasary, A. K. Singh, D. Senapati, H. Yu, P. C. Ray, *J. Am. Chem. Soc.* **2009**, 13806–13812.

[131] T. Vo-Dinh, *Sensors Actuators B Chem.* **1995**, *29*, 183–189.

[132] E. P. Hoppmann, W. W. Yu, I. M. White, *Methods* **2013**, *63*, 219–224.

[133] M. W. Knight, N. S. King, L. Liu, H. O. Everitt, P. Nordlander, N. J. Halas, *ACS Nano* **2014**, 834–840.

[134] X.-L. Qiu, Y. Zhou, X.-Y. Jin, A.-D. Qi, Y.-W. Yang, *J. Mater. Chem. C* **2015**, *3*, 3517–3521.

[135] M. Tian, D.-X. Chen, Y.-L. Sun, Y.-W. Yang, Q. Jia, *RSC Adv.* **2013**, *3*, 22111.

[136] H. Zhang, Q. S. Liu, C. L. Yang, J. Z. Lv, L. Q. Xie, M. J. Tang, Z. F. Yue, Z. G. Wan, *Food Anal. Methods* **2013**, *6*, 933–940.

[137] X.-L. Qiu, Q.-L. Li, Y. Zhou, X.-Y. Jin, A.-D. Qi, Y.-W. Yang, *Chem.*

Commun. (Camb). **2015**, *51*, 4237–40.

[138] M. Z. Iqbal, X. Ma, T. Chen, L. Zhang, W. Ren, L. Xiang, A. Wu, *J. Mater. Chem. B* **2015**, *3*, 5172–5181.

[139] S. Moraes Silva, R. Tavallaie, L. Sandiford, R. D. Tilley, J. J. Gooding, *Chem. Commun.* **2016**, *52*, 7528–7540.

[140] J. L. Lyon, D. A. Fleming, M. B. Stone, P. Schiffer, M. E. Williams, *Nano Lett.* **2004**, *4*, 719–723.

[141] T. T. Hien Pham, C. Cao, S. J. Sim, *J. Magn. Magn. Mater.* **2008**, *320*, 2049–2055.

[142] I. Robinson, L. D. Tung, S. Maenosono, C. Wälti, N. T. K. Thanh, *Nanoscale* **2010**, *2*, 2624–2630.

[143] E. S. Krystofiak, E. C. Mattson, P. M. Voyles, C. J. Hirschmugl, R. M. Albrecht, M. Gajdardziska-josifovska, J. a Oliver, *Microsc. Microanal.* **2013**, *19*, 821–834.

[144] C. A. Gorski, M. M. Scherer, *Am. Mineral.* **2010**, *95*, 1017–1026.

[145] A. Monshi, M. R. Foroughi, M. R. Monshi, *World J. Nano Sci. Eng.* **2012**, *2*, 154–160.

[146] J. Fock, L. K. Bogart, D. González, J. I. Espeso, M. F. Hansen, M. Váron, C. Frandsen, *J. Phys. D. Appl. Phys.* **2017**, *50*.

[147] G. M. da Costa, C. Blanco-Andujar, E. De Grave, Q. A. Pankhurst, *J. Phys. Chem. B* **2014**, *118*, 11738–11746.

[148] X. Liu, M. Atwater, J. Wang, Q. Huo, *Colloids Surfaces B Biointerfaces* **2007**, *58*, 3–7.

[149] S. Link, M. A. El-Sayed, *J. Phys. Chem. B* **1999**, *103*, 4212–4217.

[150] S. R. Hattersley, M. Kallumadil, Q. A. Pankhurst, P. Southern, *Resonant*

Circuit Driving Apparatus for Magnetic Field Hyperthermia Device, Has Controller Which Close Switch so Drive Current Flows through Resonant Circuit When Signal Derived from Sensor Satisfies a Predetermined Condition, **2010**, WO2010084311-A1.

[151] G. Kandasamy, A. Sudame, D. Maity, *Adv. Mater. Lett.* **2017**, *8*, 873–877.

[152] P. Guardia, S. Nitti, M. E. Materia, G. Pugliese, N. Yaacoub, J.-M. Greneche, C. Lefevre, L. Manna, T. Pellegrino, *J. Mater. Chem. B* **2017**, *5*, 4587–4594.

[153] S. Tong, C. A. Quinto, L. Zhang, P. Mohindra, G. Bao, *ACS Nano* **2017**, *11*, 6808–6816.

[154] D. Cabrera, J. Camarero, D. Ortega, F. J. Teran, *J. Nanoparticle Res.* **2015**, *17*, DOI 10.1007/s11051-015-2921-9.

[155] B. Sharma, R. R. Frontiera, A. I. Henry, E. Ringe, R. P. Van Duyne, *Mater. Today* **2012**, *15*, 16–25.

[156] D. L. Jeanmaire, R. P. Van Duyne, *J. Electroanal. Chem.* **1977**, *84*, 1–20.

[157] P. L. Stiles, J. A. Dieringer, N. C. Shah, R. P. Van Duyne, *Annu. Rev. Anal. Chem.* **2008**, *1*, 601–626.

[158] P. Gao, D. Gosztola, L. W. H. Leung, M. J. Weaver, *J. Electroanal. Chem.* **1987**, *233*, 211–222.

[159] J. T. Hupp, M. J. Weaver, D. Larkin, *Surf. Sci.* **1983**, *125*, 429–451.

[160] S. B. Chaney, S. Shanmukh, R. A. Dluhy, Y. P. Zhao, *Appl. Phys. Lett.* **2005**, *87*, 2003–2006.

[161] C. Khoury, T. Vo-Dinh, *J. Phys. Chem. C* **2008**, *112*, 18849–18859.

[162] L.-C. Cheng, J.-H. Huang, H. M. Chen, T.-C. Lai, K.-Y. Yang, R.-S. Liu, M. Hsiao, C.-H. Chen, L.-J. Her, D. P. Tsai, *J. Mater. Chem.* **2012**, *22*,

2244–2253.

[163] V. Raghavan, H. M. Fan, E. K. McCarthy, P. Dockery, A. Wheatley, I. Keogh, M. Olivo, *Micro Nano Lett.* **2016**, *11*, 769–774.

[164] Y. Ooi, I. Hanasaki, D. Mizumura, Y. Matsuda, *Sci. Technol. Adv. Mater.* **2017**, *18*, 316–324.

[165] B. Pettinger, B. Ren, G. Picardi, R. Schuster, G. Ertl, *J. Raman Spectrosc.* **2005**, *36*, 541–550.

[166] P. P. Bergmann CP, *J. Mater. Sci. Eng.* **2015**, *5*, 4–6.

[167] A. Bertoluzza, C. Fagnano, M. Antonietta Morelli, V. Gottardi, M. Guglielmi, *J. Non. Cryst. Solids* **1982**, *48*, 117–128.

[168] G. Bell, L. K. Bogart, P. Southern, M. Olivo, Q. A. Pankhurst, I. P. Parkin, *Eur. J. Inorg. Chem.* **2017**, 2386–2395.

[169] S. Ge, X. Shi, K. Sun, C. Li, C. Uher, J. R. Baker, M. M. B. Holl, B. G. Orr, *J. Phys. Chem. C* **2009**, *113*, 13593–13599.

[170] M. Lattuada, T. A. Hatton, *Langmuir* **2007**, *23*, 2158–2168.

[171] R. Alwi, S. Telenkov, A. Mandelis, T. Leshuk, F. Gu, S. Oladepo, K. Michaelian, *Biomed. Opt. Express* **2012**, *3*, 2500–9.

[172] B. Stella, S. Arpicco, M. T. Peracchia, D. Desmaele, J. Hoebeke, M. Renoir, J. D'Angelo, L. Cattel, P. Couvreur, *J. Pharm. Sci.* **2000**, *89*, 1432–1442.

[173] M. Rogosnitzky, S. Branch, *BioMetals* **2016**, *29*, 365–376.

[174] A. Roggan, M. Friebel, K. Dorschel, A. Hahn, G. Muller, *J. Biomed. Opt.* **1999**, *4*, 36–46.

[175] A. B. E. Attia, S. Y. Chuah, D. Razansky, C. J. H. Ho, P. Malempati, U. S. Dinish, R. Bi, C. Y. Fu, S. J. Ford, J. S. S. Lee, et al., *Photoacoustics* **2017**,

7, 20–26.

[176] J. Garcia, T. Tang, A. Y. Louie, *Nanomedicine* **2015**, *10*, 1343–1359.

[177] Y.-K. Peng, C. N. P. Lui, T.-H. Lin, C. Chang, P.-T. Chou, K. K. L. Yung, S. C. E. Tsang, *Faraday Discuss.* **2014**, *175*, 13–26.

[178] S. Morscher, W. H. P. Driessen, J. Claussen, N. C. Burton, *Biochem. Pharmacol.* **2014**, *2*, 103–110.

[179] J. Gil-Tomás, S. Tubby, I. P. Parkin, N. Narband, L. Dekker, S. P. Nair, M. Wilson, C. Street, *J. Mater. Chem.* **2007**, *17*, 3739.

[180] D. Bartczak, A. G. Kanaras, *Langmuir* **2011**, *27*, 10119–10123.

[181] E. M. Hotze, T. Phenrat, G. V. Lowry, *J. Environ. Qual.* **2010**, *39*, 1909.

[182] U. I. Tromsdorf, N. C. Bigall, M. G. Kaul, O. T. Bruns, M. S. Nikolic, B. Mollwitz, R. A. Sperling, R. Reimer, H. Hohenberg, W. J. Parak, et al., *Nano Lett.* **2007**, *7*, 2422–2427.

[183] L. Sandiford, A. Phinikaridou, A. Protti, L. K. Meszaros, X. Cui, Y. Yan, G. Frodsham, P. A. Williamson, N. Gaddum, R. M. Botnar, et al., *ACS Nano* **2013**, *7*, 500–512.

[184] H.-Y. Lee, Z. Li, K. Chen, A. R. Hsu, C. Xu, J. Xie, S. Sun, X. Chen, *J. Nucl. Med.* **2008**, *49*, 1371–1379.

[185] H. Xu, L. Cheng, C. Wang, X. Ma, Y. Li, Z. Liu, *Biomaterials* **2011**, *32*, 9364–9373.

[186] R. Thomas, I. K. Park, Y. Y. Jeong, *Int. J. Mol. Sci.* **2013**, *14*, 15910–15930.

[187] H. Cai, K. Li, M. Shen, S. Wen, Y. Luo, C. Peng, G. Zhang, X. Shi, *J. Mater. Chem.* **2012**, *22*, 15110.

[188] J. Li, Y. Hu, J. Yang, P. Wei, W. Sun, M. Shen, G. Zhang, X. Shi,

Biomaterials **2015**, *38*, 10–21.

[189] J. Reguera, D. Jiménez de Aberasturi, M. Henriksen-Lacey, J. Langer, A. Espinosa, B. Szczupak, C. Wilhelm, L. M. Liz-Marzán, *Nanoscale* **2017**, *9*, 9467–9480.

APPENDIX

Current Publications

[1] **G. Bell**, L. K. Bogart, P. Southern, M. Olivo, Q. A. Pankhurst, I. P. Parkin, Eur. J. Inorg. Chem. 2017, 2386–2395.

Future Publications

[2] **G. Bell**, G. Balasundaram, A. B. E. Attia, F. Mandino, Q. A. Pankhurst, M. Olivo, I. P. Parkin, Photoacoustic functionalised iron oxide nanoparticles for multimodal optoacoustic and magnetic resonance imaging, To be submitted.

[3] **G. Bell**, Q. A. Pankhurst, M. Olivo, I. P. Parkin, Surface enhanced raman scattering spectroscopy using iron oxide – gold nanocomposite, To be submitted.